

Analytical, FEA, And Experimental Research of 2D-Vibration Assisted Cutting (2D-VAC) In Titanium Alloy Ti6Al4V

Rendi Kurniawan

Yeungnam University

Farooq Ahmed

Yeungnam University

Gun Chul Park

Yeungnam University

Tae Jo Ko (✉ tjko@yu.ac.kr)

Yeungnam University

Research Article

Keywords: 2D-VAC, Finite Element Analysis, Stress, Cutting Force, Temperature, Chip Formation

Posted Date: May 26th, 2021

DOI: <https://doi.org/10.21203/rs.3.rs-474065/v1>

License:  This work is licensed under a Creative Commons Attribution 4.0 International License.

[Read Full License](#)

Version of Record: A version of this preprint was published at The International Journal of Advanced Manufacturing Technology on August 12th, 2021. See the published version at <https://doi.org/10.1007/s00170-021-07831-8>.

Analytical, FEA, and Experimental Research of 2D-Vibration Assisted Cutting (2D-VAC) in Titanium Alloy Ti6Al4V

RENDI KURNIAWAN

Affiliation: Precision Machining Laboratory room 214, Department of Mechanical Engineering, Yeungnam University, 280 Daehak-Ro, Gyeongsan, Gyeongbuk, South Korea.

e-mail: rendi@ynu.ac.kr

FAROOQ AHMED

Affiliation: Precision Machining Laboratory room 214, Department of Mechanical Engineering, Yeungnam University, 280 Daehak-Ro, Gyeongsan, Gyeongbuk, South Korea.

e-mail: farooqahmed333@gmail.com

GUN CHUL PARK

Affiliation: Precision Machining Laboratory room 214, Department of Mechanical Engineering, Yeungnam University, 280 Daehak-Ro, Gyeongsan, Gyeongbuk, South Korea.

e-mail: gu2572@ynu.ac.kr

TAE JO KO* (Corresponding Author)

Affiliation: Precision Machining Laboratory room 214, Department of Mechanical Engineering, Yeungnam University, 280 Daehak-Ro, Gyeongsan, Gyeongbuk, South Korea.

e-mail: tjko@yu.ac.kr

ABSTRACT

In the 2D-Vibration Assisted Cutting (2D-VAC) method, the cutting tool shakes in a 2-dimensional approach because of superimposed high-frequency modulation. This high-frequency modulation effect creates a displacement at a tiny scale of micrometers and causes an escalation in the resultant cutting speed. Consequently, 2D-VAC has superior advantages compared to traditional cutting (TC). This manuscript describes research on 2D-VAC that focuses on modeling cutting forces (mathematical model) and finite element analysis (FEA) results. The FEA results are focused on the von Mises stress, plastic strain, cutting force, cutting temperature, and residual stress. In addition, an experiment for the chip formation, micro-structure layer, and micro-hardness was also analyzed in this study. According to the modeling results, the cutting force has a comparable pattern to the FEA results. The stress contour result confirms that the 2D-VAC method has lower stress than that in the TC method during tool retraction mode. Additionally, the plastic strain in the 2D-VAC method can be higher than that in the TC method. According to the temperature results, the peak temperature in the 2D-VAC could be higher than that in the TC method. The residual stress shows that there is a compressive effect. Thus, the compressive stress is higher than that in the TC method. Micro-hardness results confirmed that there is not too much change from the original surface in the 2D-VAC method. The result of micro-structure morphology also confirmed that there is a significant shear deformation flow in case of the TC method, although less occurs in the 2D-VAC method.

Keywords: 2D-VAC; Finite Element Analysis; Stress; Cutting Force; Temperature; Chip Formation

1. INTRODUCTION

The mechanical vibration cutting phenomenon is defined as three types based on the vibration sources [1]. The first type is free vibration, the second type is forced vibration, and the third type is self-excited vibration. In the case of free vibration, an impact force during a cutting procedure causes the tooling system to vibrate. The forced vibration is also named active vibration [2]. One example of forced vibration in metal cutting is vibration-assisted cutting (VAC) [3]. The cutting tool is pulsed in an intermittent manner by an external source of excitation (for example, by a piezo actuator or ultrasonic horn mechanism structure) in the VAC process. Thus, the cutting tool intermittently cuts the workpiece surface in either one-, two-, or three-dimensional space [3].

Evidently, the VAC method has brought many positive effects in metal cutting, such as facilitating chip separation, decreasing frictional force, decreasing the deformation zone, suppressing the tool wear, and enhancing surface integrity of a machined product [4]. The VAC method has been implemented successfully to fabricate ultrafine topography on the cut faces of hard-to-cut materials [4]. The VAC method has also been well known in practices to manufacture advanced micro/nano-textured surfaces [5].

The self-excited vibration has been also known as a passive vibration [2]. One example of the passive vibration in material removal method has been known as chatter vibration [6]. The cutting tool shakes in the chatter vibration due to an internal excitation that is near to the physical frequency of a mechanical formation such as a cutting tool, tool holder, spindle, and workpiece. The negative impact in chatter vibration yields

absolute destruction of the surface quality after machining, and it is undesirable [6]. The magnitude of the cutting force during chatter vibration is also very high due to periodically escalating the depth of cut. A variable-speed mechanism has been one of the solutions to avoid chatter vibration [7] and avoids *self-excited vibration* due to internal excitation growing rapidly.

Ti6Al4V titanium alloy has been extensively employed in the airplane and space craft industry due to excellent properties (excellent corrosion resistance, superior strength, relatively low density, and excellent thermal resistance due to low thermal conductivity) [8,9]. However, Ti6Al4V is categorized as a difficult-to-machine material because of minimal thermal conductivity properties. Because of this, high pressure and temperature are accumulated in the secondary zone (the tool-chip interface). An accumulated heat is transferred into the cutting tool instead of into the deformed chip. Thus, severe tool wear occurs [9].

The severe tool wear is due to either abrasive wear or diffusion wear in very high temperature and creates a rough surface finish and inaccurate dimensions of the machined part. This wear problem causes machining inefficiency in production and is still a major issue during titanium cutting. The severe tool wear causes surface defects such as cracking, tearing, cavities, and smearing surfaces, etc. [8,9], and it decreases the surface quality of the final product. The machining inefficiency during titanium cutting has been enhanced by previous researchers who optimized the cutting conditions [10], developed a novel tool [11], and developed a novel methodology [12].

A serrated or segmented chip (also named as a “saw-tooth” chip) generally occurs during the cutting of Ti6Al4V alloy. The segmented chips could be generated at lower cutting speeds and are more clearly seen at high cutting speeds [13]. Theoretically, the segmented chip generation is due to the thermoplastic uncertainty concentrated in adiabatic shear bands and the crack initiation in the primary shear zone. Calamaz *et al.* [14] numerically studied a segmented chip when cutting Ti6Al4V alloy. The modified Johnson-Cook formula with material strain softening phenomenon was able to predict a segmented chip. Sima and Ozel [15] proposed a modified Johnson-Cook model based on temperature-dependent flow softening, wherein strain hardening, thermal softening, and flow softening are coupled. Published work emphasized that the flow strain softening occurrence is particularly important throughout chip deformation in Ti6Al4V cutting.

VAC is categorized according to the degree of freedom of the tool movement [3]. 1D-VAC (one-dimensional-vibration-assisted-cutting) is defined as where the tool vibrates along the cutting velocity direction. 2D-VAC (two-dimensional-vibration-assisted-cutting) is defined as where the tool shakes sequentially in together the cutting velocity and depth-of-cut paths. 3D-VAC (three-dimensional-vibration-assisted-cutting) is defined as where the tool vibrates sequentially in three-dimensional space with additional movement of 2D-VAC. Recently, VAC has been acknowledged for cutting effectively compared to a traditional cutting (TC) method. Advantages in VAC such as decreased cutting energy and surface roughness have been reported [16]. The 2D-VAC method is fundamentally similar to the elliptical vibration cutting (EVC) [17] as an alternative approach to 1D-VAC.

Recently, 2D-VAC has been acknowledged to effectively cut hard or difficult-to-cut material (e.g., Ti6Al4V [18] and Inconel 718 [19]) or even brittle material [20]. Also, 2D-VAC has been acknowledged to manufacture a textured surface pattern such as a micro-dimple [21], micro-groove [16], surface diffraction effect [22], and wettability pattern [23]. Therefore, 2D-VAC will become a promising metal removal process in the future and it is our motivation to explore this technique more. Our study focuses on the 2D-VAC cutting force model for a segmented chip and a finite element study for this promising technique. This specific study of a force model including a segmented chip in 2D-VAC has not been inspected yet and can be investigated more deeply.

Recent advanced modeling 2D-VAC has been investigated widely, including a cutting force model [24] and surface roughness [25]. Researchers also explored 2D-VAC employing numerical methods for instance the FEA [26,27] or the molecular dynamics (MD) [28]. However, recent past investigations [29,30] did not include segmented chip morphology, which must be considered during cutting of Ti6Al4V material using VAC. As explained before, the segmented chip occurs due to the thermoplastic instability during cutting [14]. In our study, the segmented chip morphology is included during 2D-VAC, which affects the amplitude of the cutting force cycle.

The general purpose in this research is to propose a numerical investigation for 2D-VAC to find the von Mises stress, the cutting force, the plastic strain, the cutting temperature, the chip morphology, and the residual stress during cutting of Ti6Al4V material. Additionally, in this paper, the analytical cutting force for Ti6Al4V material is also proposed. The transient modified Johnson-Cook shear flow, the transient shear strain rate, the transient thickness of cut, and the transient shear angle are considered in this study, and subsequently the analytical cutting force result is matched to the numerical solution. Additionally, the surface structure of Ti6Al4V after cutting using 2D-VAC is also investigated.

2. FORCE MODEL of 2D-VAC

Fig. 1 shows an illustration of 2D-VAC during cutting of a material such as titanium alloy, where the cutting edge radius is considered, and a segmented chip is formed. The tool movement in the 2D-VAC through the consideration of the cutter edge radius has been introduced [16,25,31]. The cutting edge radius influences the micro-cutting. Thus, it has to be considered and it cannot be neglected. Therefore, Eq. 1 clarifies the tool trajectory in the x-path ($x_e(t)$) and y-path ($y_e(t)$) at the CC point. The CC point is the cutter contact or cutter engagement point between the workpiece and the cutter edge in the 2D-VAC, as illustrated in Fig. 1.

$$\begin{aligned} x_e(t) &= a_m \cdot \cos(2\pi f_v \cdot t) + a_m - V_c \cdot t - r_e \cdot \sin \theta_t(t) \\ y_e(t) &= b_m \cdot \cos(2\pi f_v \cdot t + \varphi) + b_m + r_e(1 - \cos \theta_t(t)) \end{aligned} \quad (1)$$

a_m and b_m are the elliptical locus magnitude in μm in the x- and y-paths, correspondingly, as demonstrated in Fig. 1. f_v is the frequency of vibration of the cutter

$$TOC_t(t) = \begin{cases} 0 & t < t_A, t \geq t_D \\ y_e(t_p) - y_e(t) & t_A \leq t < t_T \\ DOC - y_e(t) & t_T \leq t < t_D \end{cases} \quad (3)$$

The times t_A , t_D , t_P , and t_T must be found by a numerical method such as the Newton-Raphson method. Eqs. 4, 5, 6, and 7 define them [16]. The time t_T (Eq. 7) can be found by determination of the value of the nominal rake angle of the cutting tool (α_o). In this study, a polycrystalline (PCD) insert cutting tool has been used, which has a nominal rake angle α_o of 7° .

$$x_e(t_A) - x_e(t_A') = 0 ; y_e(t_A) - y_e(t_A') = 0 \quad (4)$$

$$-a \cdot 2\pi f_v \cdot \sin(2\pi f_v \cdot t_D) - V_c - r_e \cdot \frac{d}{dt} \sin \theta_t(t_D) = 0 \quad (5)$$

$$t_P = t_D - 1/f_v \quad (6)$$

$$\frac{x_e(t_T) - x_e(t_P)}{y_e(t_T) - y_e(t_P)} = \tan(\alpha_o) \quad (7)$$

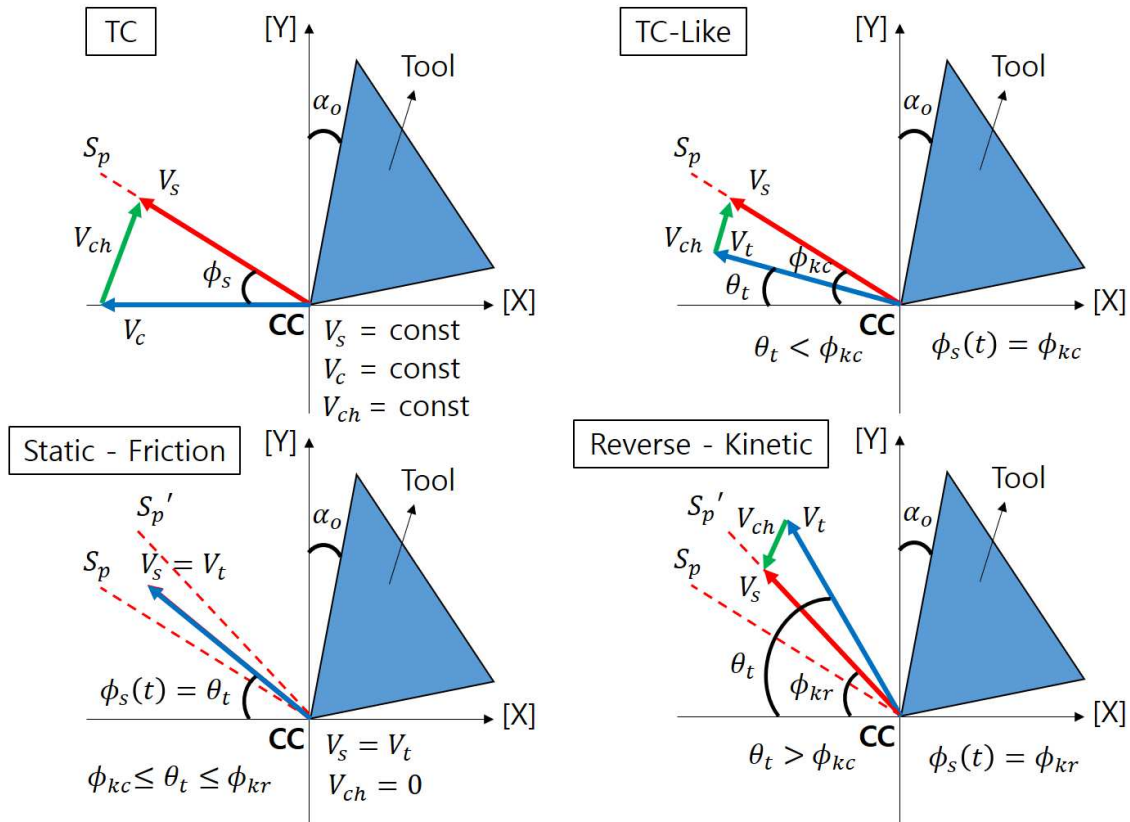


Fig. 2 Model of transient shear angle (TC-like, static-friction, and reverse-kinetic) in the 2D-VAC mechanisms

In the 2D-VAC process, it has been thought that there are three main mechanisms [24,32,33] during cutting in one single cycle of cut. The first is the traditional cutting mechanism (TC-like), the second is the static-friction mechanism, and the third is the reverse-kinetic mechanism, as shown in Fig. 2. The transient shear angle $\phi_s(t)$ remains a constant during the TC-like mechanism, as modelled in Fig. 2. Thus, the value is equal to ϕ_{kc} , which can be determined based on the minimum cutting energy principle [32], as shown in Eq 9.

In the case of the static-friction mechanism, $\phi_s(t)$ is equal to the slope angle of the velocity vector, as introduced in Eq. 2. The value of $\phi_s(t)$ becomes transient between shear plane S_p and shear plane S_p' . Meanwhile, during the reverse-kinetic mechanism, $\phi_s(t)$ is equal to the constant shear angle of reverse-kinetic ϕ_{kr} , which can be determined in Eq. 9 [32], which is based on the minimum energy principle. In Eq. 9, the friction angle (β) was assumed to be equal to 20° .

Fig. 3 illustrates the cutting force vectors in orthogonal cutting during the TC-like and reverse-kinetic mechanism. Generally, the friction force direction F_f is downward like in the TC-like mechanism. However, during the reverse-kinetic mechanism, the friction force direction F_f goes in the reverse way on the sliding rake face. Thus, the transient shear angle should be equal to ϕ_{kr} when θ_t is more than ϕ_{kr} .

$$\phi_s(t) = \begin{cases} \phi_{kc} , & \theta_t < \phi_{kc} \\ \theta_t , & \phi_{kc} \leq \theta_t \leq \phi_{kr} \\ \phi_{kr} , & \theta_t > \phi_{kr} \end{cases} \quad (8)$$

$$\begin{aligned} \phi_{kc} &= 45^\circ - \frac{1}{2}(\beta - \alpha_o) ; \\ \phi_{kr} &= 45^\circ + \frac{1}{2}(\beta + \alpha_o) ; \end{aligned} \quad (9)$$

Fig. 4 illustrates the shear strain diagram during the cutting of titanium in the 2D-VAC for all the cases: TC-like, static-friction, and reverse-kinetic. The deformed chip has a segmented shape. It can be analyzed like a piece of a stacked card of the deformed chip (as shown in Fig. 4) [34] when a segmented triangle in the main cutting zone is being analyzed. In the traditional cutting, as shown in Fig. 4, the cutting velocity vector V_c is towards the horizontal direction, where Δs is the elongation of the workpiece material during the shear deformation and is parallel to the shear velocity vector V_s . Δd is illustrated as a thickness between two sequences of segmented chip or the thickness of the shear plane, and it is always perpendicular to the shear velocity vector V_s .

When during the TC-like mechanism, θ_t is less than ϕ_{kc} , so $\phi_s(t) = \phi_{kc}$. When using the static-friction mechanism, the velocity vector V_c is between shear planes S_p and S_p' , so $\phi_s(t) = \theta_t$. When during the reverse-kinetic mechanism, θ_t is more than ϕ_{kr} , so $\phi_s(t) = \phi_{kr}$, and the chip velocity vector V_{ch} direction is reversed. Therefore, the transient shear strain $\varepsilon(t)$ can be defined in Eq. 10 for all cases.

$$\varepsilon(t) = \frac{\Delta s}{\Delta d} = \frac{\cos \alpha_o}{\sin \phi_s(t) \cos(\phi_s(t) - \alpha_o)} \quad (10)$$

Meanwhile, the transient shear strain rate $\dot{\varepsilon}(t)$ can be defined as follows:

$$\dot{\varepsilon}(t) = \frac{V_t(t) \cos \theta_t(t) \cos \alpha_o}{\Delta d \cos(\phi_s(t) - \alpha_o)} \quad (11)$$

where Δd can be defined in Eq. 12 [32]. TOC_{max} is the maximum value of the transient thickness of cut $TOC_t(t)$.

$$\Delta d = \frac{TOC_{max}}{10 \sin \phi_s(t)} \quad (12)$$

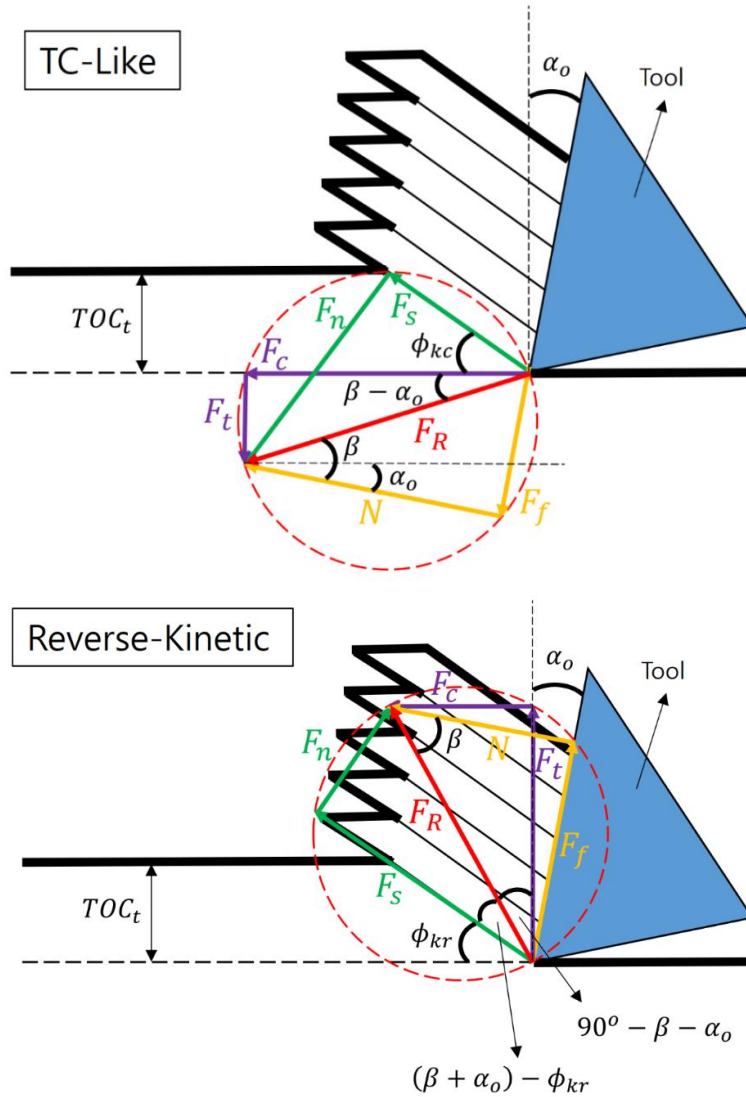


Fig. 3 Merchant's circle when TC-like and Reverse-Kinetic cutting

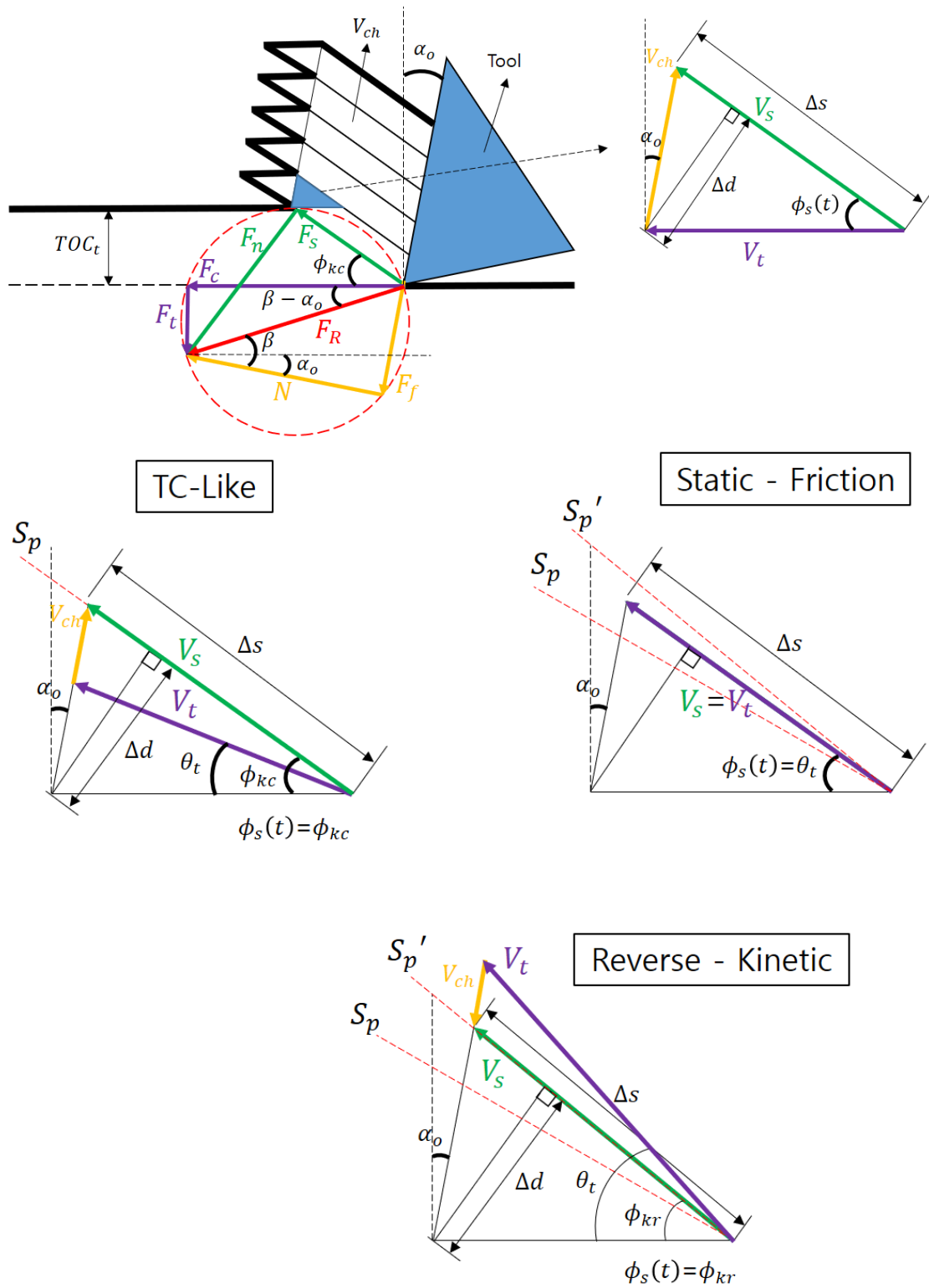


Fig. 4 Illustration of transient shear strain in 2D-EVC

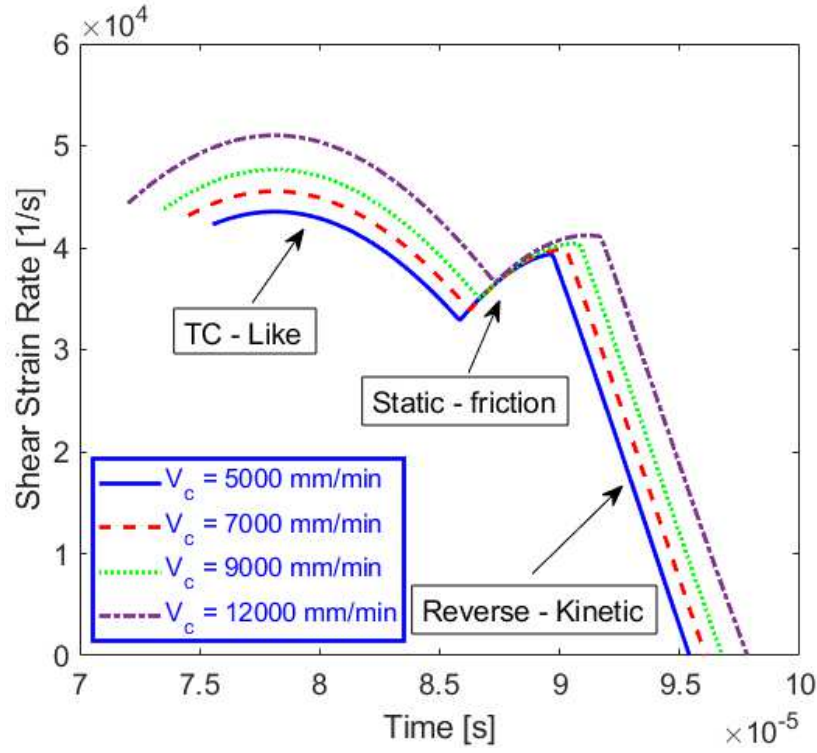


Fig. 5 Shear strain rate simulation for 2D-VAC with various cutting speeds V_c

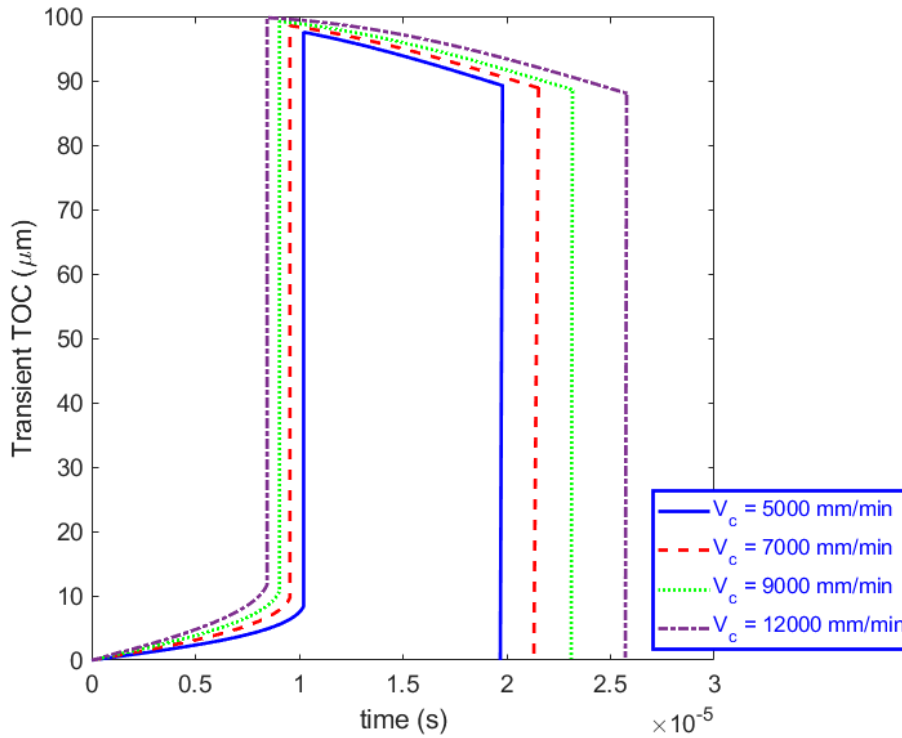


Fig. 6 Transient TOC with variation of cutting speeds V_c

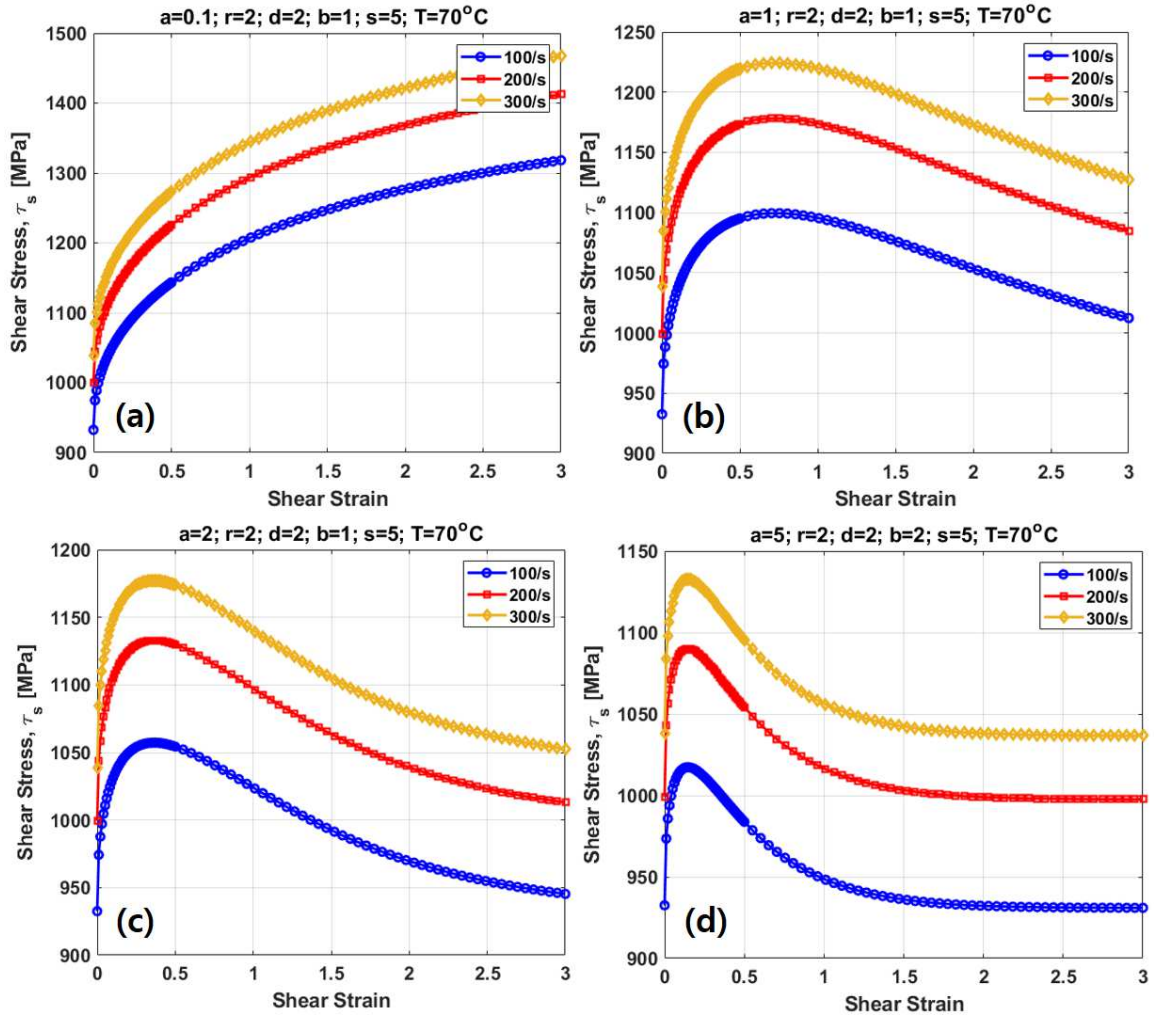


Fig. 7 Transient shear stress of modified Johnson-Cook model with variation of variable a . (a) $a=0.1$, (b) $a=1$, (c) $a=2$, (d) $a=5$.

Fig. 5 shows the shear strain rate during single cutting with 2D-VAC with variation of cutting speeds V_c . In the TC-like case, the shear strain rate increases and then decreases. During the static-friction case, the shear strain rate slightly increases due to an escalation of the transient shear angle. The shear strain rate decreases due to the increase of the slope angle to 90 degrees ($\cos \theta_t(t) = 0$), in the reverse-kinetic case.

Fig. 6 shows the TOC_t (Eq. 3), which is plotted with variation of the cutting speeds V_c . The time axis has been normalized, where t_A (beginning time to cut) was set to zero. It is clear that by increasing the cutting speeds, the periodical time to engage with the workpiece increases. This means it increases the horizontal speed ratio ($HSR = V_c / 2\pi f_v a_m$). Therefore, the engaging time of the cutting tool with the workpiece is longer when increasing cutting speed.

Shear deformation occurs during the material processing with both TC and 2D-VAC. Therefore, S_p (the shear stress on the shear plane) should be defined to identify cutting forces. The shear stress model from Sima's model [15] according to the modified Johnson-Cook flow stress model is adopted in this paper, as described in Eq. 13. The transient shear strain and shear strain rate is defined in Eq. 10 and Eq. 11, respectively. The temperature-dependent flow softening parameters D and P vary on the cutting temperature (T) and melting temperature of the workpiece (T_m). The parameters D and P [15] are described in Eq. 14. Meanwhile, the Johnson-Cook parameters (A , B , C , n , and m) for titanium alloy are introduced in Table 1.

$$\tau_s(t) = \frac{1}{\sqrt{3}} \left(A + B \left(\frac{\varepsilon(t)}{\sqrt{3}} \right)^n \left(\frac{1}{\exp \left(\left(\frac{\varepsilon(t)}{\sqrt{3}} \right)^a \right)} \right) \right) \cdot \left(1 + C \cdot \ln \frac{\dot{\varepsilon}(t)}{\dot{\varepsilon}_o} \right) \cdot \left(1 - \left(\frac{T - T_r}{T_m - T_r} \right)^m \right) \cdot \left(D + (1 - D) \left[\tanh \left(\frac{1}{\left(\frac{\varepsilon(t)}{\sqrt{3}} + P \right)^r} \right) \right]^s \right) \quad (Eq. 13)$$

$$D = 1 - \left(\frac{T}{T_m} \right)^d \quad \text{and} \quad P = \left(\frac{T}{T_m} \right)^b \quad (Eq. 14)$$

Table 1 Johnson-Cook parameters of Ti6Al4V alloy from Calamaz et al. [14]

A [MPa]	B [MPa]	C	n	m	$\dot{\varepsilon}_o$ [1/s]	T_s [°C]
968	380	0.197	0.421	0.577	1	25
T_m [°C]		a	r	d	b	s
1676		2	2	2	1	5

Fig. 7 shows the transient shear stress of the modified Johnson-Cook model versus shear strain with different parameters of a . Fig. 7 also shows variation of the shear strain rate. The shear stress fundamentally increases when the shear strain rate increases from 100/s to 300/s, as shown in Fig. 7. The shear stress typically has a trend to increase when $a = 0.1$. A small value of a does not have any significant effect on the strain hardening term. In case of a higher constant of a , the shear stress tends to increase, and at critical

shear strain, the shear stress tends to decrease. A higher value of α decreases the critical shear strain, as shown in Fig. 7, and it also decreases the shear stress.

It should be known that the shear stress also depends on the cutting temperature, which is known as thermal softening. However, the cutting temperature ($T = 70^\circ\text{C}$) is used to predict the shear stress. This value is used based on an experimental result in the TC method (range: $60 - 70^\circ\text{C}$).

The shear force upon the shear plane has to be determined first to predict the principal and thrust force. Eq. 15 presents the shear force, which is according to the projection of the Johnson-Cook shear flow onto the cutting area $\{w \cdot TOC_t(t)\}$. $TOC_t(t)$ is the transient TOC (Eq. 3), and w is the width of cut.

$$F_s(t) = \frac{\tau_s(t)}{\sin \phi_s(t)} \cdot w \cdot TOC_t(t) \quad (Eq. 15)$$

The resultant force is given in Eq. 16 for different slope angle θ_t . The first term is given based on Merchant's circle like in the TC-like and static-friction mechanism when $\theta_t \leq \phi_{kr}$. Meanwhile, the second term of Eq. 16 is used when $\theta_t > \phi_{kr}$ during the reverse kinetics (Fig. 3).

$$F_R(t) = \frac{F_s(t)}{\cos(\phi_{kc} + \beta - \alpha_o)} \quad \theta_t \leq \phi_{kr}$$

$$F_R(t) = \frac{F_s(t)}{\cos(\beta + \alpha_o - \phi_{kc})} \quad \theta_t > \phi_{kr} \quad (Eq. 16)$$

Finally, the principal cutting force $F_c(t)$ and the thrust cutting force $F_t(t)$ are given in Eq. 17. The minimum principal cutting energy is implemented in terms of the transient shear angle $\phi_s(t)$.

$$F_c(t) = F_R(t) \cos(\beta - \alpha_o) = F_R(t) \cos(90^\circ - 2\phi_s(t))$$

$$F_t(t) = F_R(t) \sin(\beta - \alpha_o) = F_R(t) \sin(90^\circ - 2\phi_s(t)) \quad (Eq. 17)$$

3. NUMERICAL METHODOLOGY

In this research, the FEA cutting process of both 2D-VAC and TC has been carried out using AdvantEdge software version 7.4 made by Third Wave Systems. The adaptive re-meshing technique and Lagrangian formula were adopted to suppress element distortion. Fig. 1 displays the FEA simulation setup of the 2D-VAC. In the case of the TC,

the vibration of the cutting tool is simply not given for vibration amplitudes and ultrasonic frequency. There are no vibrational effects as input constraints in the case of TC.

A rectangular workpiece with a width dimension of $H = 500 \mu\text{m}$ and length dimension of $L = 1000 \mu\text{m}$ was considered. The workpiece was moved along the x -direction or cutting speed direction of the V_c vector and it had a sliding constraint at the bottom with no motion along the y -direction. The cutting tool was a PCD (poly-crystalline-diamond) tool that has an angle of 7° for both the rake (α) and flank (γ). In the FEA, the cutter has been assumed as inflexible (rigid body) and un-deformable.

Tool Vibration:

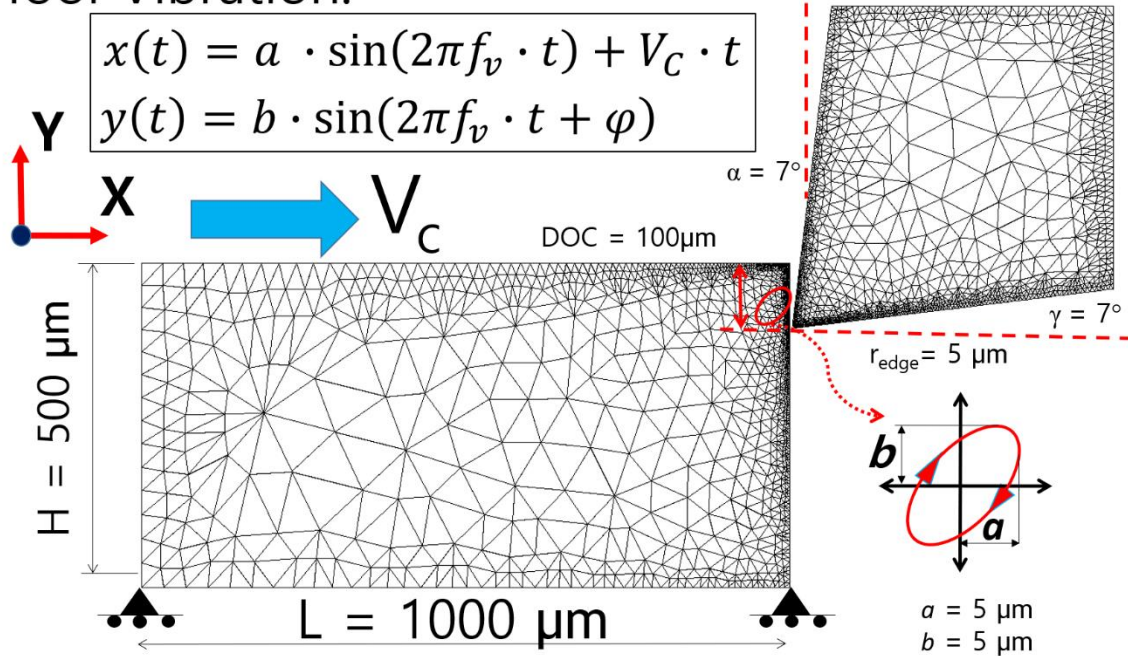


Fig. 8 FEA simulation setup for 2D-VAC

Table 1 demonstrates cutting and meshing parameters in FEA using AdvantEdge simulation software. In the FEA simulation, the cutting speed was considered to be varied from 5 to 12 m/min, which has been considered to be lower than the critical vibrational speed ($V_{cr} \cong 2\pi f_v a_m$). The cutting depth was considered as about $100 \mu\text{m}$, the cutting width was considered as about $80 \mu\text{m}$, the cutting length was considered as about $500 \mu\text{m}$, which is half of the workpiece's total length, and the friction coefficient was considered as about 0.5, which is considered in dry cutting (no lubrication) and in harsh conditions.

It should be noted that the cutting depth is the feed, and the width of cut is the axial DOC in actual turning. In the case of the 2D-VAC, the vibration amplitudes a and b were set as $5 \mu\text{m}$ for both x - and y -directions. The ultrasonic frequency vibration (f) was fixed at about 16 kHz like the working frequency of the transducer. The phase difference (θ) was fixed at about 90° .

For both methods, the simulation conditions were without cooling and tool wear considerations. In the case of the mesh setting, the number of nodes was approximately 24000. The minimum and maximum element sizes were 0.004 mm and 0.4 mm, correspondingly. A mesh refinement factor scale of 2 and a mesh coarsening factor scale of 6 have been used for the adaptive remeshing during the simulation. \

A maximum number of output frames of 1000 has been considered to investigate perfect post-processed FEA analysis for the tool trajectory of the 2D-VAC technique. The Ti6Al4V database in AdvantEdge was used for the workpiece material properties. In addition, the workpiece hardness was set to be similar to that in Table 3. PCD with high conductivity was selected for the cutting tool material, which is available from the AdvantEdge database.

Table 2 FEA cutting simulation parameter of the 2D-VAC and TC in FEA

Parameters	TC	2D-VAC
Cutting speed [V_c]	5, 7, 9, 12 m/min	5, 7, 9, 12 m/min
Cutting depth [feed]	100 $\mu\text{m}/\text{rev}$	100 $\mu\text{m}/\text{rev}$
Cutting width [w]	80 μm	80 μm
Cutting length [L]	500 μm	500 μm
Friction coefficient	0.5	0.5
Frequency [f_v]	-	16 kHz
Amplitude [a & b]	-	$a = 5 \mu\text{m}$ & $b = 5 \mu\text{m}$
Phase different [φ]	-	90°
Condition	Dry and no wear	Dry and no wear
Number of nodes	24000	24000
Min element size	0.004 mm	0.004 mm
Max element size	0.4 mm	0.4 mm
Mesh refinement	2	2
Mesh coarsening	6	6
Output frame	1000	1000
Tool	PCD	PCD
Workpiece	Ti6Al4V	Ti6Al4V

4. Ti6Al4V MATERIAL and EXPERIMENTAL SETUP

4.1 Ti6Al4V Material

Ti6Al4V material is broadly utilized in the aerospace industry such as in jet engine parts (fan blades and compressor blades) [8] due to its high mechanical strength and low weight. In this study, the Ti6Al4V material was supplied by SamJin Jongmil Co. Industry without any heat-treatment involved. To reveal its microstructure before mechanical machining, the primary phases of alpha (α) and beta (β) must be revealed in this study before deformation. An image of the Ti6Al4V microstructure was taken by a SEM (Scanning Electron Microscopy) machine after mirror polishing and then etching with

Kroll's solution (consists of 100 mL distilled H₂O, 2-6 mL HNO₃, and 1-3 mL HF) at room temperature (25 °C).

Fig. 9 demonstrates the Ti6Al4V microstructure SEM images, which consists of mainly two phases: (α -alpha) and (β -beta) phase. It is clearly shown that dark color is the α -phase and the light color is the β -phase. In addition, the lamellar β -phase structure is also observed in Fig. 9. The lamellar microstructure consists of secondary α in the β -phase. The mechanical strength parameters of the Ti6Al4V are demonstrated in Table 3. It is shown that the Ti6Al4V has hardness in the range of about 330 – 340 HV according to the author's own observation and high mechanical strength of about 1000 MPa. However, the tensile strength decreases to 500 MPa at high elevated temperature [35].

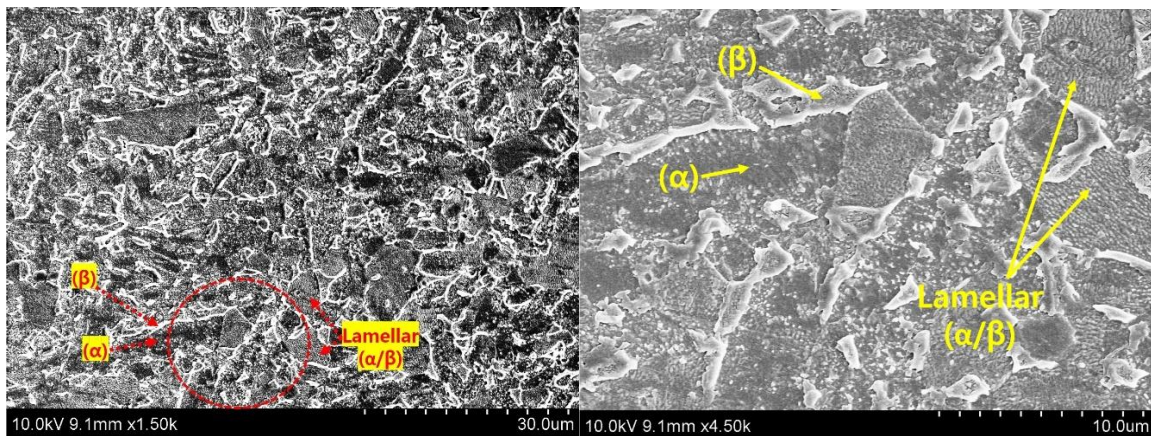


Fig. 9 SEM Ti6Al4V metallography after Kroll's etching

Table 3 Ti6Al4V mechanical properties [35,36]

Properties	Value
Young's modulus	104-113 GPa
Yield tensile strength (YTS)	900 MPa
Ultimate tensile strength (UTS)	1000 MPa
Tensile strength at 400°C	550 MPa
Elongation	18%
Vickers hardness	330 – 340 HV
Density	4510 kg/m ³
Poisson ratio	0.32

4.2 Experimental Setup

The experimental setup in this study is shown in Fig. 10. The 3D-vibrated tool holder (3D-VTH) is installed in a conventional CNC-turning lathe machine. A similar design of 3D-VTH was developed by the author in a previous study. Even though 3D-VTH was used in this study, 2D vibration is only used in this study. The third signal and phase shift were deactivated. Based on Table 4, the variation of the cutting speed was from 5 to 12

m/min. Therefore, the rotational speed was then converted from the linear speed with 28 mm of as the initial workpiece diameter.

The rotational speeds were from 56.8 rpm to 136.4 rpm, which were set in the CNC-turning machine. The feed was maintained at a medium feed rate and was constant at 100 $\mu\text{m}/\text{rev}$. Also, the radial cutting depth was set as about 80 μm . The vibrational cutting condition was maintained constant at a high frequency of about 16 kHz, the vibrational amplitude was about 5 μm , and the phase difference was 90°.

The PCD tool was used in this study, which has a cutting edge radius of about 5 – 10 μm [21]. A dry cutting condition was used for all experiments. A dynamometer (KISTLER) 9256C was utilized to obtain cutting force data. The sensitivity was set in an amplifier (5019B) as 26 pC/N for F_x and F_z directions and 13 pC/N for the F_y direction.

A low pass filter of 10kHz has been used. The data were recorded using an NI (NATIONAL INSTRUMENTS) USB DAQ NI 6363 with sampling frequency of 100 kHz and data amount of 40k. Fig. 10 shows the SEM S-4200 (HITACHI) and μ -hardness tester (MMT-X MATSUZAWA) that were utilized in this study.

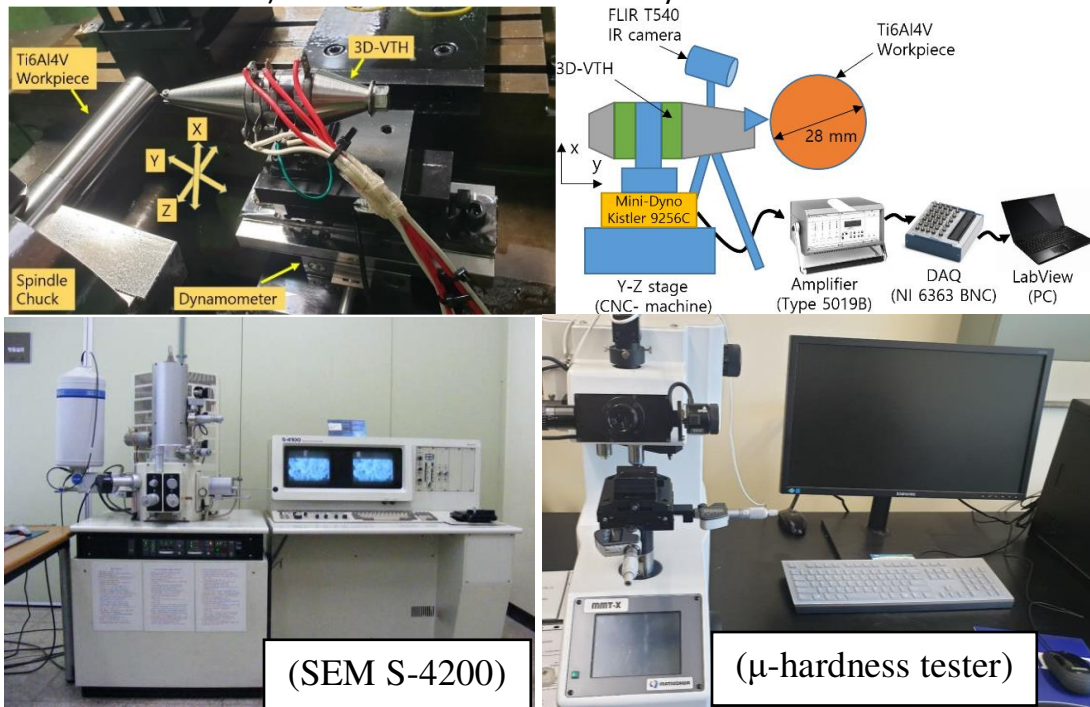


Fig. 10 Experimental setup of the 2D-VAC, SEM HITACHI S-4200 and μ -hardness tester

Table 4 Experimental setup of 2D-VAC of Ti6Al4V

Parameters	TC	2D-VAC
Rotational speed [N_w]	56.8, 79.6, 102.3, 136.4 rpm	56.8, 79.6, 102.3, 136.4 rpm
Cutting speed [V_c]	5, 7, 9, 12 m/min	5, 7, 9, 12 m/min
Workpiece diameter [D]	28 mm (initial)	28 mm (initial)
Feed [f]	100 $\mu\text{m}/\text{rev}$	100 $\mu\text{m}/\text{rev}$
Radial cutting depth [w]	80 μm	80 μm
Frequency [f_v]	-	16 kHz

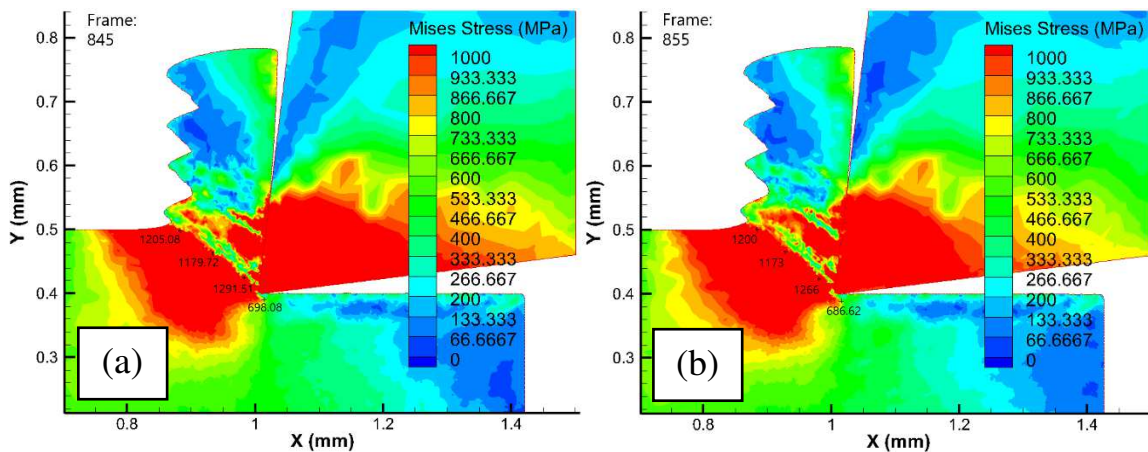
Amplitude [a & b]	-	5 μm
Phase difference [φ]	-	90°
Condition	Dry cutting	Dry cutting
Tool	PCD	PCD
Workpiece	Ti6Al4V	Ti6Al4V

5. RESULTS AND DISCUSSION

5.1 Stress distribution contour

Figs. 11 (a-d) show the 2D numerical result of the von Mises stress distribution contour in the TC process under a cutting velocity of $V_c = 9$ m/min, feed of 100 $\mu\text{m}/\text{rev}$, and cutting width of 80 μm . Steady state has been achieved, and the frames were captured from the 845th to 875th frames with 1000 frames in total. The maximum von Mises stress is concentrated in the primary deformation zone, in which the value of high stress is approximately between 1100 to 1200 MPa, as revealed in Fig. 11. In addition, the tertiary zone is approximately in the range of 500 to 600 MPa.

In the case of the TC process, the stress concentration mainly remains constant and has a similar contour for the 845th, 855th, 865th, and 875th frames. The cutting tool also experiences a high von Mises stress on the tool edge with more than approximately 1000 MPa (red contour). The constant stress concentration in the TC process did not significantly fluctuate due to a constant cutting depth [feed] of 100 $\mu\text{m}/\text{rev}$ (Table. 2).



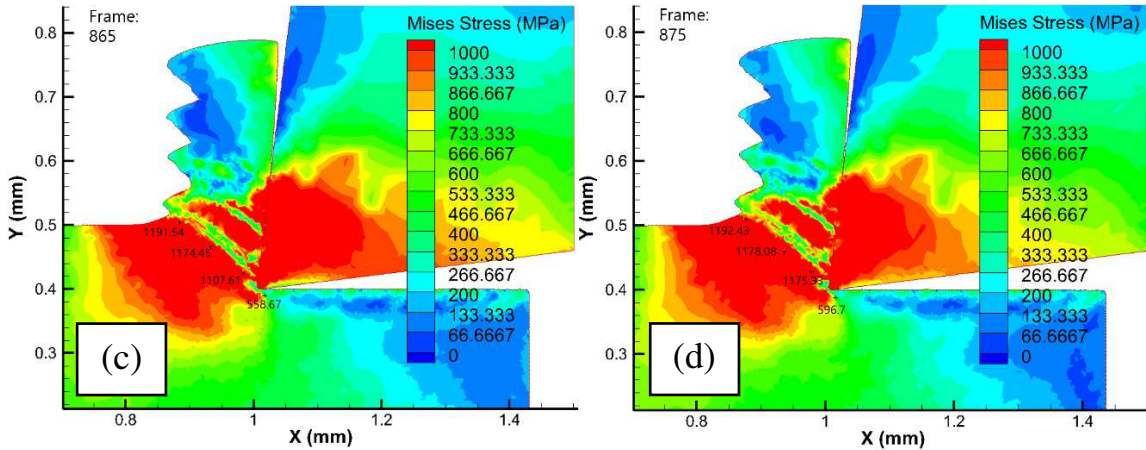
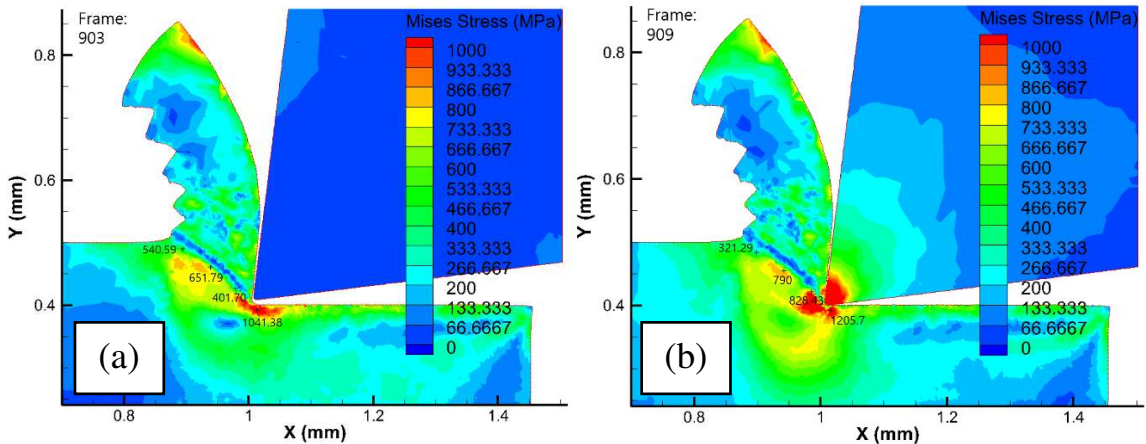


Fig. 11 Von Mises stress contour in the TC process at $V_c = 9$ m/min, $f = 100$ μ m/rev, $w = 80$ μ m

Fig. 12 demonstrates the von Mises stress concentration in the case of the 2D-VAC method under a cutting velocity of 9 m/min, feed of 100 μ m/rev, and cutting width of 80 μ m for one single cycle of cut. Fig. 12 shows a lower von Mises stress concentration in the primary deformation zone compared to the TC process due to retraction of the cutting tool edge from the primary deformation zone. The frames were captured when the cutting tool edge begins retraction from the deformed chip in frame 903 (Fig. 12(a)), in which the stress concentration is low. This is indicated by the blue and green contours in the primary deformation zone with a stress value of 400 – 650 MPa.

In addition, there is a stress localization of about 1041.38 MPa in the separation zone, which is hard to release after shear deformation. Then, the cutting tool edge begins to enter the main cutting zone in frame 909 (Fig. 12(b)), in which the impact energy adds stress localization in the separation zone of up to 1205.7 MPa and increases the stress in the primary deformation zone. The cutting tool edge cuts like in the TC process in frame 915 (Fig. 12(c)), in which the maximum von Mises concentration stress is similar in the TC process between 1100 and 1200 MPa. In the final cycle of the cutting, the cutting tool edge moves upward and begins to leave the main cutting zone in frame 918 (Fig. 12(d)). Then, the cutting tool begins to recut the workpiece in the next cycle of the cut.



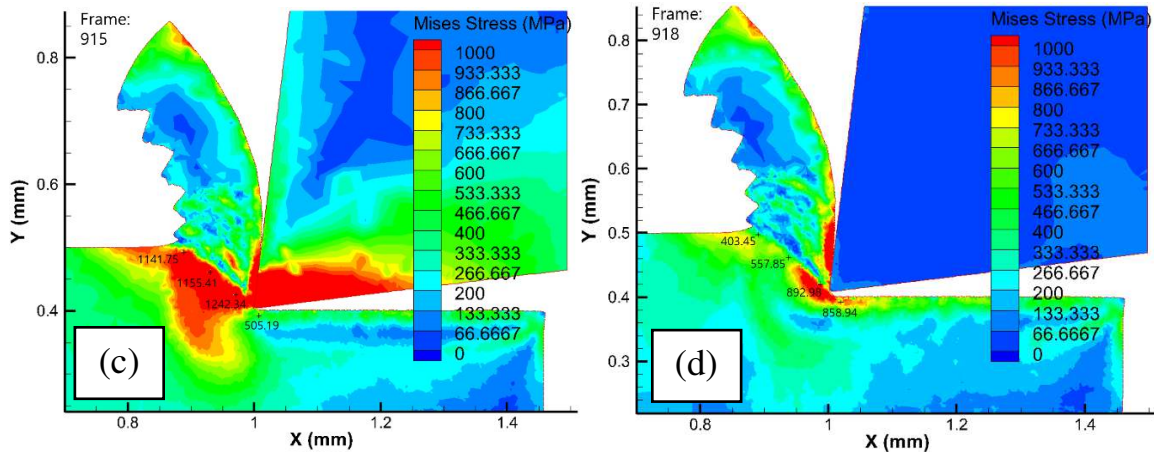


Fig. 12 Von Mises stress contour in the 2D-VAC process at $V_c = 9$ m/min, $f = 100$ μ m/rev, $w = 80$ μ m, $f_v = 16$ kHz, $\varphi = 90^\circ$, $a = 5$ μ m, and $b = 5$ μ m **(a)** after retracted tool, **(b)** beginning to cut, **(c)** cutting process, **(d)** disengaged tool

Fig. 13 shows the von Mises stress comparison between the TC and the 2D-UAVC at cutting velocity of 12 m/min, feed of 100 μ m/rev, and cutting width of 80 μ m. Fig. 13 shows that three polylines for three different locations. Path 1 is near the free cutting zone of the deformed chip. Path 2 is in the middle zone of the deformed chip zone. Path 3 is near the rake-chip contact zone of the deformed zone. The von Mises stress in the 2D-VAC is lower than that in the TC process, especially during the tool retraction in the 2D-VAC, as demonstrated in Fig. 13.

The maximum von Mises stress in the TC process could reach approximately 1200 MPa and it is uniform among paths 1, 2, and 3. Meanwhile, the maximum von Mises stress in the 2D-VAC is lower than that in the TC process but is not uniform among paths 1, 2, and 3. It is clear that there is a stress localization in the separation zone (tertiary zone), which is difficult to release after shearing deformation.

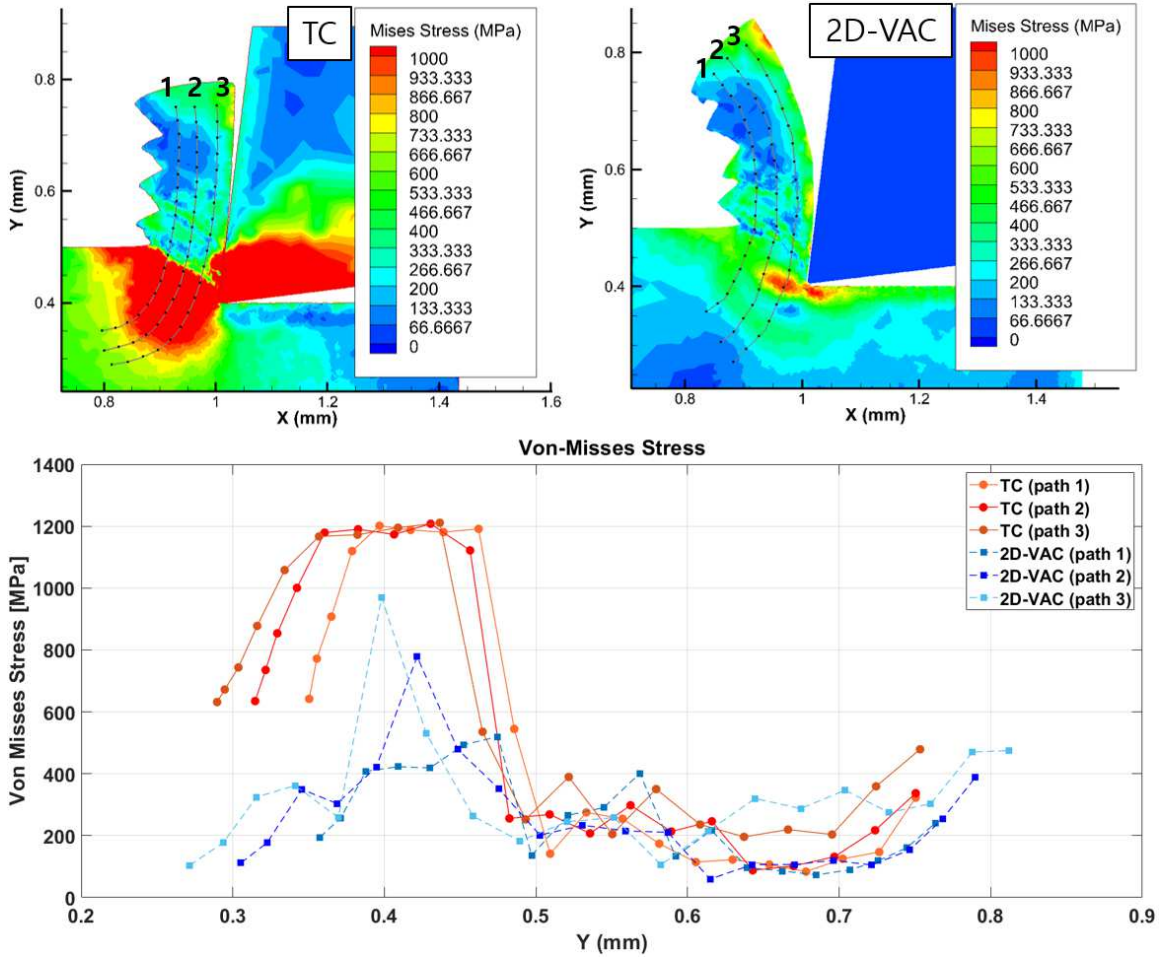


Fig. 13 Von Mises stress comparison between the TC and the 2D-VAC at $V_c = 12$ m/min, $f = 100$ μ m/rev, $w = 80$ μ m, $f_v = 16$ kHz, $\varphi = 90^\circ$, $a = 5$ μ m and $b = 5$ μ m

5.2 Plastic Strain

Figs. 14 and 15 show the numerical results of the plastic strain contour in both the TC and the 2D-VAC process at cutting velocity of 7 m/min and 9 m/min, respectively. The plastic strain has been plotted according to polynomial lines 1, 2, and 3. Path 1 is near the free zone of the deformed chip. Path 2 is the middle of the deformed chip. Path 3 is near the chip-rake contact zone.

As shown in Fig. 14, the maximum plastic strain is a localized occurrence on the adiabatic shear band [13] of the serrated deformed chip. In the case of paths 1 and 2 for both the TC and the 2D-VAC for $V_c = 7$ m/min, the maximum peak of the plastic strain has approximately equal value. However, in the case of path 3, which is near the chip-rake zone, the maximum peak of the plastic strain in the 2D-VAC is higher than that in the TC process.

In the case of $V_c = 9$ m/min, as demonstrated in Fig. 15, the highest peak of the plastic strain in the 2D-VAC is higher than that in the TC process for all paths 1, 2, and 3.

More shear deformation occurs in the case of the 2D-VAC. These numerical results indicate that the 2D-VAC process has a curlier chip deformation and higher chip shear deformation due to a higher plastic strain value near the chip-rake contact zone. Therefore, the chip can be easily removed in the 2D-VAC process compared to the TC process.

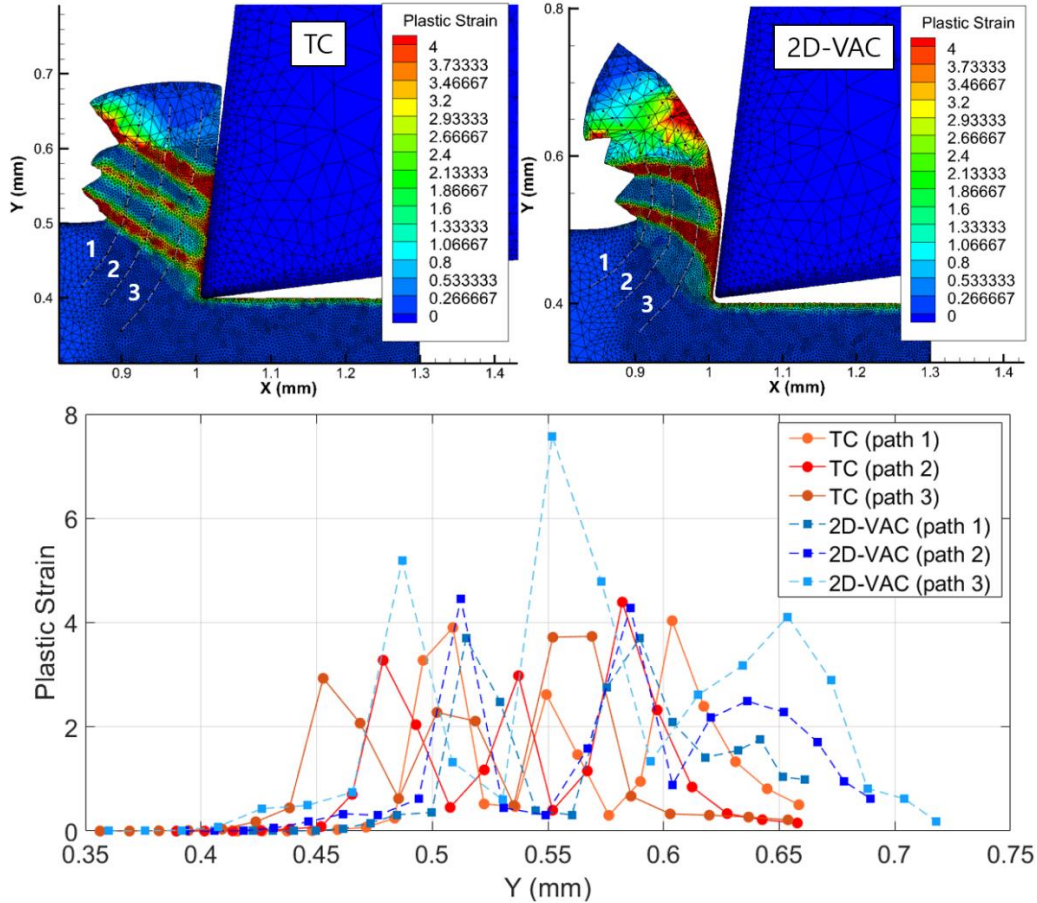


Fig. 14 Plastic strain comparison between the TC and the 2D-VAC at $V_c = 7$ m/min, $f = 100$ μ m/rev, $w = 80$ μ m, $f_v = 16$ kHz, $\varphi = 90^\circ$, $a = 5$ μ m, and $b = 5$ μ m

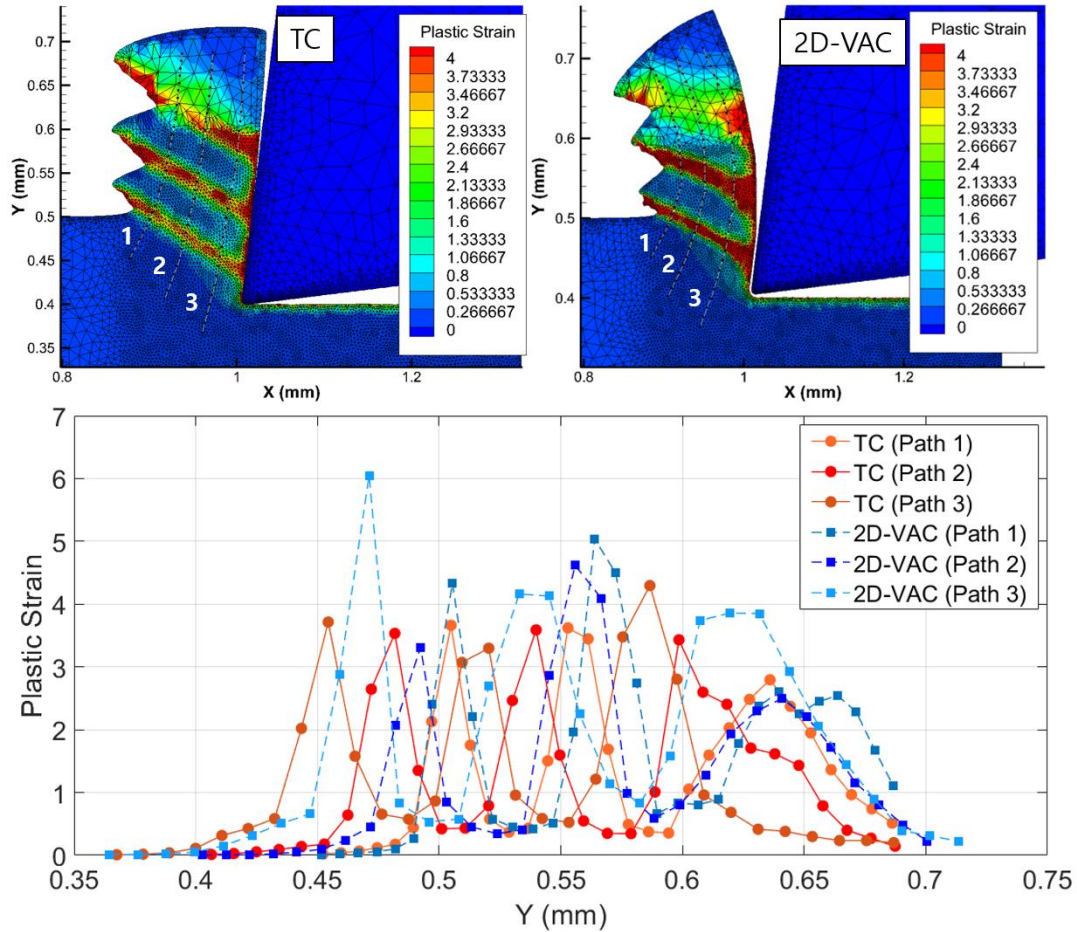


Fig. 15 Plastic strain comparison between the TC and the 2D-VAC at $V_c = 9$ m/min, $f = 100$ μ m/rev, $w = 80$ μ m, $f_v = 16$ kHz, $\varphi = 90^\circ$, $a = 5$ μ m, and $b = 5$ μ m

5.3 Cutting Force

Fig. 16 demonstrates the numerical cutting force results for both the TC and the 2D-VAC process under cutting speed of 7 m/min. The cutting forces pattern shows that the TC process does not show a constant pattern, as shown in Fig. 16(a). This is due to the effect of the strain softening phenomenon, the shear localization, and the chip segmentation occurrence [14].

It has been mentioned in previous publications that the cutting of Ti-6Al-4V generally produces segmented chips even at relatively low cutting speeds [14,15]. It can be understood that when the strain softening phenomenon occurs, the material strength decreases as the strain increases [37]. After achieving the maximum V_c level at 18 N, the cutting force pattern in the TC process then declines after it loses its material strength. At this point, the segmented chip morphology grows. After that, the cutting force gradually increases again after the material strength grows. Therefore, the cutting force pattern in the TC process does not have a relatively constant value.

Fig. 16(b) shows the numerical cutting force under the 2D-VAC process. It is clear that the cutting force has a typical periodical pattern of a vibration owing to the different

cutting depth based on time due to intermittent elliptical tool motion. The principal force (F_c) is indicated by the blue line graph. F_c goes from zero to the maximum level when the transient cutting depth is the maximum. The zero level of the principal force (F_c) means that the cutting tool leaves the main cutting zone. According to the principal force (F_c) pattern, the 2D-VAC process also experiences the strain softening phenomenon, and therefore, the maximum peak level is not at the same level with a nonuniform degree. However, the principal force (F_c) pattern definitely has more uniformity of segmentation.

Fig. 17 shows the simulated cutting force in the 2D-VAC, which is created by the analytical technique under different cutting velocities of 5 and 12 m/min. At the beginning of the cut, the principal force behaves as in TC. Then in the middle of the cutting, the principal force goes down like in the static-friction mechanism, leading to the reverse-kinetic mechanism. Meanwhile, the thrust force is negative during the static-friction mechanism, which is an indication of reversed direction of the friction force [32]. The thrust force climbs when the transient shear angle becomes ϕ_{kr} , while the transient thickness of cut reduces. Then, the thrust force goes to zero as the cutting tool begins to leave the main cutting zone.

Fig. 18 demonstrates the comparison for both the analytical and numerical cutting force under the cutting speed of 12 m/min. Additionally, the FFT (Fast Fourier Transform) is also included for proving that the vibration frequency is about 16 kHz. The analytical cutting force has a similar pattern to the numerical cutting force. Even though the slope pattern of the cutting force is different, the maximum level of the principal and the thrust force is similar. In addition, the thrust force has a similar negative pattern value. These results indicate that the cutting force in the 2D-VAC could be estimated by the both the analytical and numerical methods.

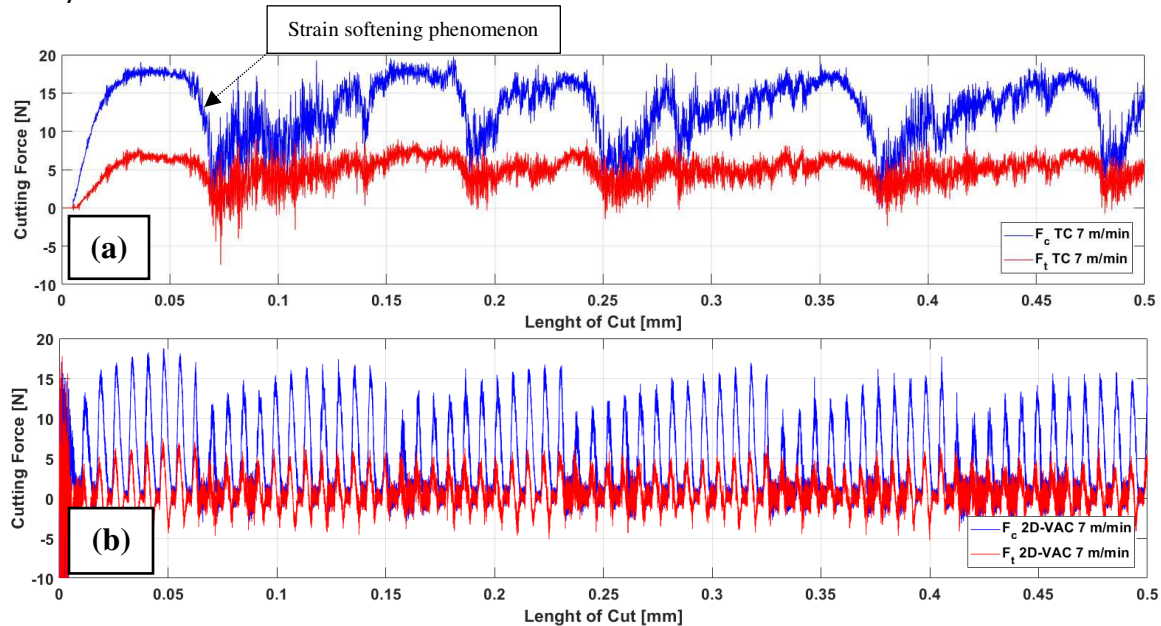


Fig. 16 Simulated cutting force comparison between (a) the TC and (b) the 2D-VAC at $V_c = 7$ m/min

Analytical, FEA, and Experimental Research of 2D-Vibration Assisted Cutting (2D-VAC) in Titanium Alloy Ti6Al4V

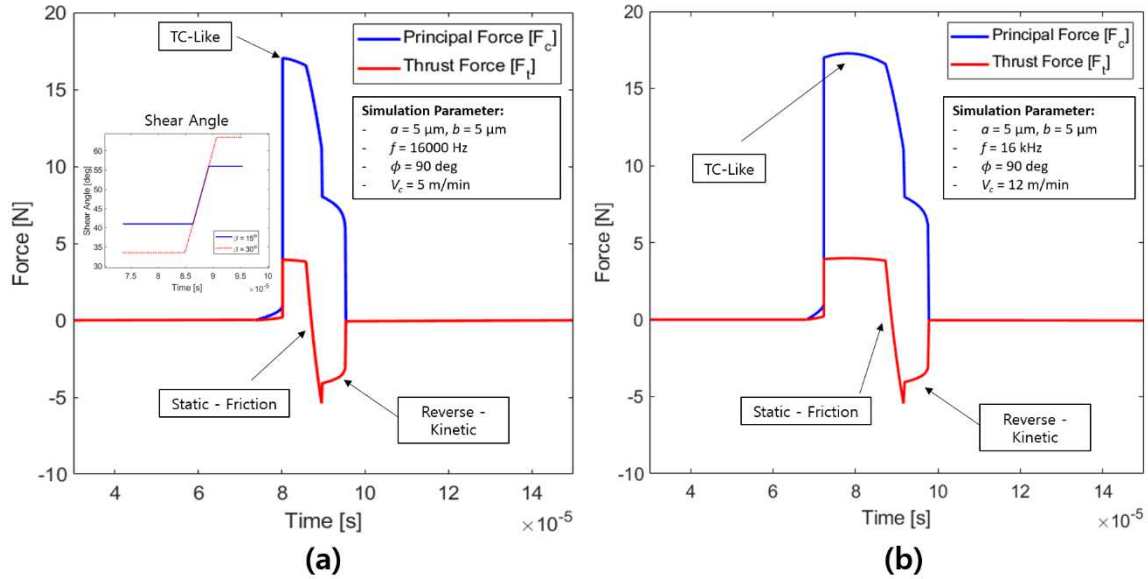


Fig. 17 Simulated cutting force in the 2D-VAC. **(a)** $V_c = 5$ m/min, **(b)** $V_c = 12$ m/min

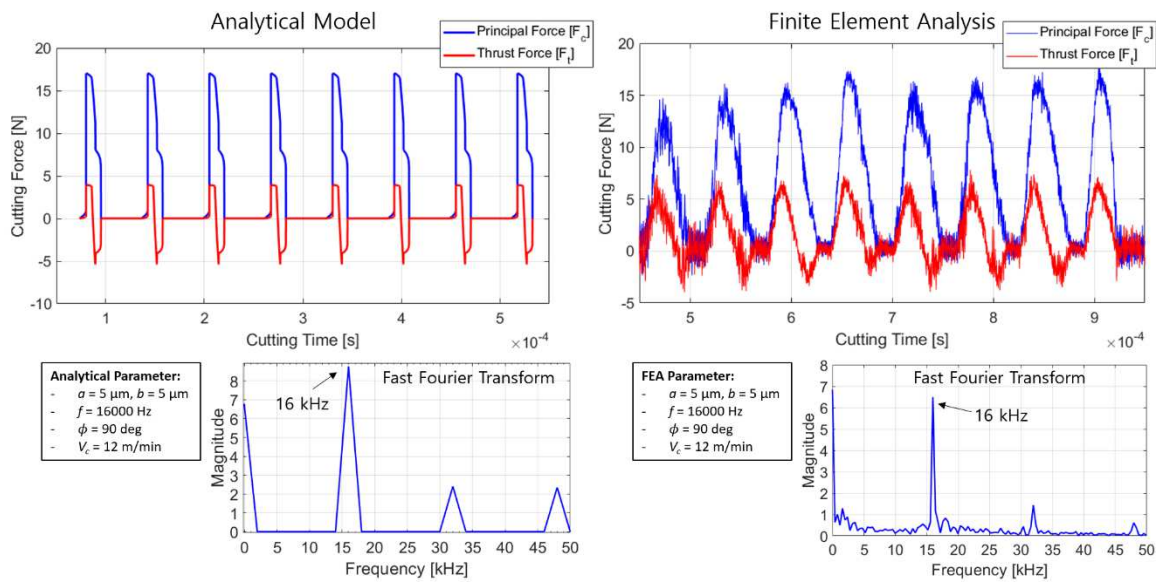


Fig. 18 Comparison between analytical force and FEA simulated force for the 2D-VAC at $V_c = 12$ m/min

Fig. 19 shows the average cutting force component for the thrust (F_t) and the principal cutting (F_c) force between the TC and the 2D-VAC process. Based on numerical results, the cutting forces (F_c and F_t) for the 2D-VAC process are certainly lesser than that in the TC process. Based on experimental results, at lower cutting speeds (5 and 7 m/min), F_c and F_t in the 2D-VAC process are lower than that in the TC process. Interestingly, at a higher cutting velocity of 12 m/min, F_c in the 2D-VAC could be even slightly higher than that in the TC. The vibration could now be ineffective to decrease the load due to the higher velocity than the critical vibration speed. However, the chip temperature in the 2D-VAC process is still lower than that in the TC process (Sec. 5.4).

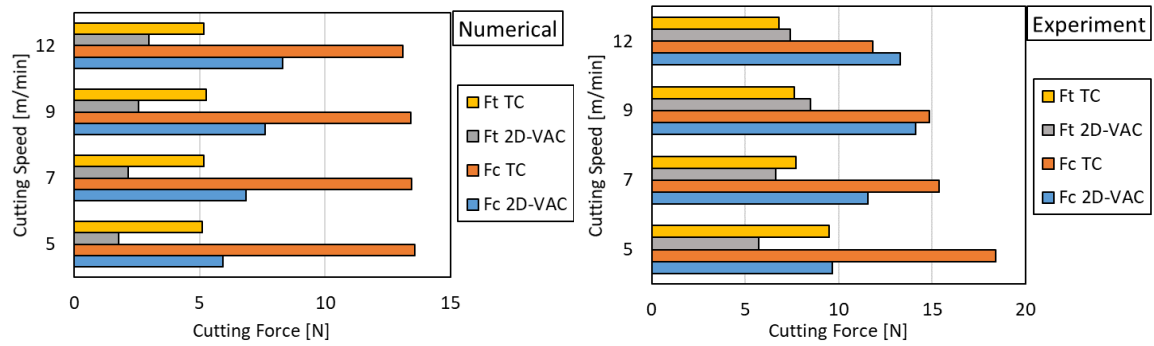


Fig. 19 Average cutting force comparison among numerical and experimental results.

5.4 Cutting Temperature

Fig. 20 shows the cutting temperature contour and the temperature plot at a specific polyline between the TC and the 2D-VAC process. The cutting temperature frame in the 2D-VAC is only captured when the tool is disengaged (the cutting tool separates from the main cutting zone), as shown in Fig. 20. The maximum cutting temperature occurs in the primary deformation zone indicated by the red color. The cutting temperature develops largely in the primary deformation zone due to large shearing velocity upon the shear plane, wherein the large shearing velocity is proportional with the large shear strain rate. The heat produced around the primary deformation zone occurs then dissipated along the deformed chip and the machined surface.

The cutting temperature around the primary deformation region in 2D-VAC process happens lower than that in the TC process during the tool disengagement. In the case of $V_c = 9$ m/min, the cutting temperature around the primary deformation region in the TC is approximately 264.35 °C. This is higher than that in the 2D-VAC, which is about 215 °C, as shown in Figs. 20 (a-b).

In the case of $V_c = 12$ m/min, the result has been found to be similar to $V_c = 9$ m/min, in which the cutting temperature in 2D-VAC is a bit more than that in the TC process. This can be confirmed from the polyline graph shown in the Figs. 20(e-f), where the peak temperature is more in the TC process. However, after the Y-distance is more than 0.5 mm, the rest of the temperature is higher in the 2D-VAC. During tool disengagement, the remaining high temperature is challenging to dissipate quickly into the air. As the result the chip temperature remains higher in the 2D-VAC for the numerical solution.

Fig. 21 shows the average temperature on the cutting tool between the TC and the 2D-VAC under variation of cutting speeds. The tool temperature value in the TC is nearly constant with fluctuation. Meanwhile, the tool temperature value in the 2D-VAC is periodically shifting. The maximum peak of the tool temperature in the 2D-VAC process could be higher than that in the TC process during the tool engagement. It could be understood that the relative shearing velocity becomes higher due to additional relative vibration velocity. The tool temperature in the 2D-VAC process could be lower than that in the TC process during the tool disengagement. The mean value of temperature shows that the tool temperature in the 2D-VAC is slightly lower than that in the TC process.

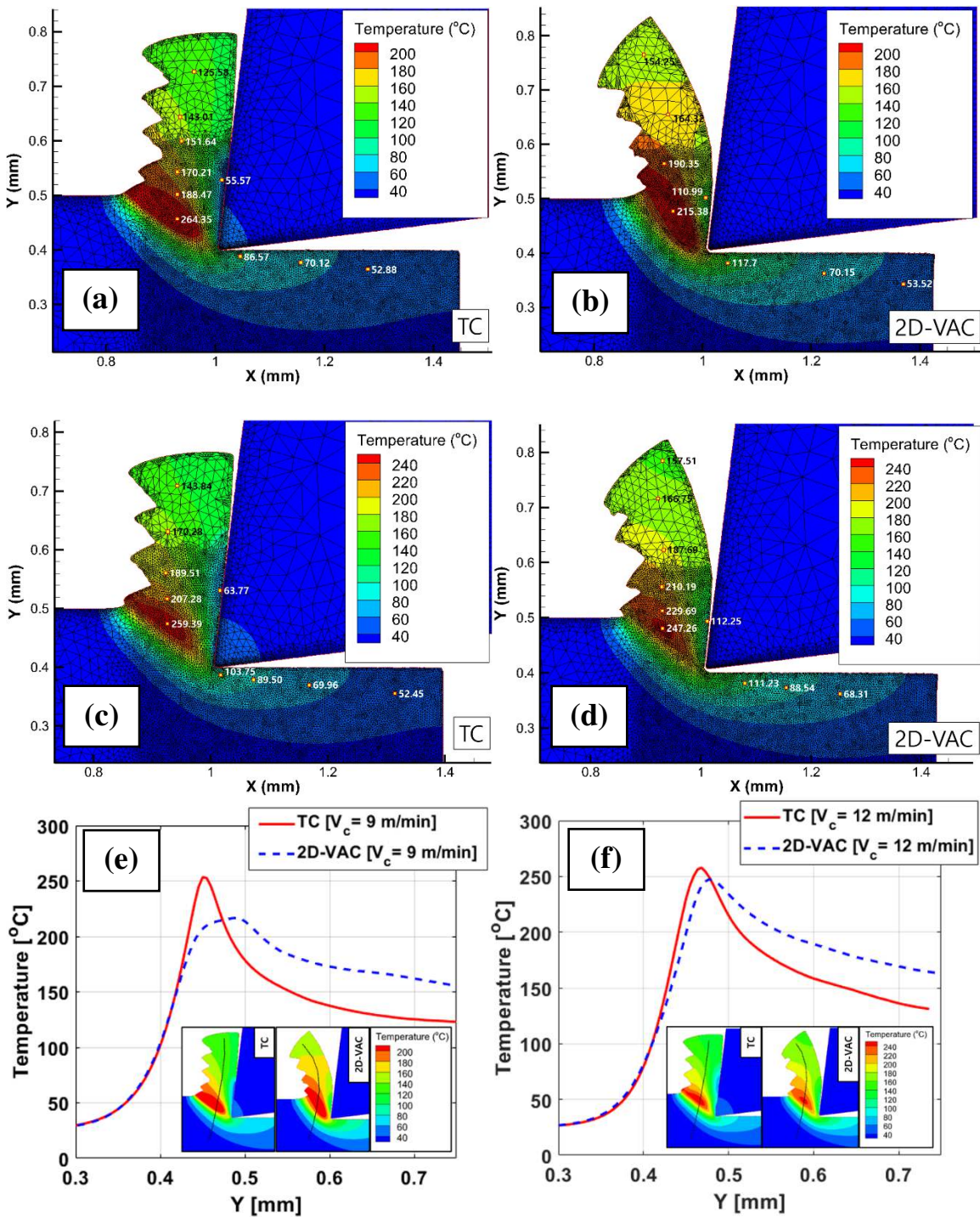


Fig. 20 Temperature contour comparison between (a) TC at $V_c = 9$ m/min, (b) 2D-VAC at $V_c = 9$ m/min, (c) TC at $V_c = 12$ m/min, (d) 2D-VAC at $V_c = 12$ m/min, (e, f) temperature plot at specific polyline.

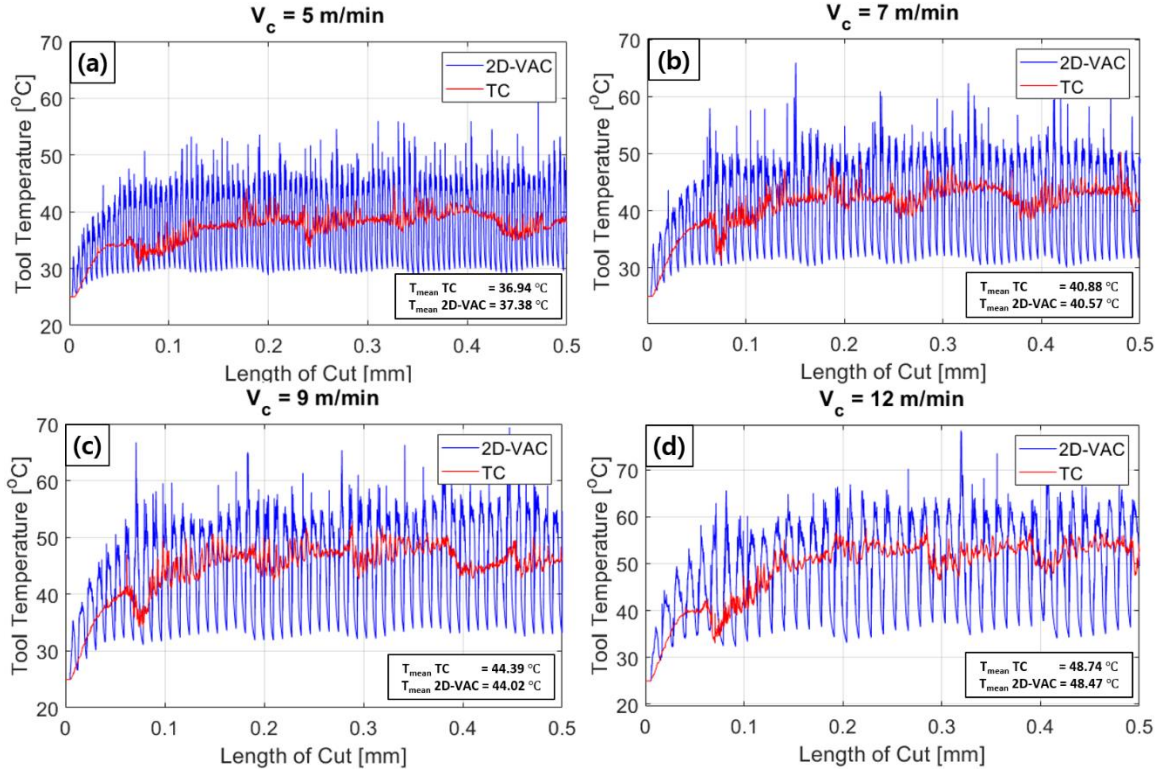


Fig. 21 Comparison of the average simulated temperature in the cutting tool between the 2D-VAC and TC method through change of the cutting speed. **(a)** $V_c = 9$ m/min, **(b)** $V_c = 7$ m/min, **(c)** $V_c = 9$ m/min and **(d)** $V_c = 12$ m/min

Fig. 22 shows the experimental measurement of the cutting temperature during using an FLIR T540 IR camera, in which the material emissivity ($\varepsilon = 0.2$) [38] has been set for the tool's diamond material. Every figure displays maximum tool temperature values. According to the IR camera, the results of the tool temperature in the case of the 2D-VAC are lower than that in the TC process under different cutting velocities ($V_c = 9$ m/min and $V_c = 12$ m/min). As shown Figs. 22(a) and (b), the tool temperature in the TC process is about 63°C and the tool temperature in the 2D-VAC process is about 55°C.

Under a higher cutting velocity under $V_c = 12$ m/min, the maximum tool temperature of the cutting tool could reach 80°C under the TC process for $V_c = 12$ m/min (Fig. 22 (c)). Meanwhile, the maximum tool temperature of the 2D-VAC for $V_c = 12$ m/min is lesser than that under the TC process. If the cutter temperature is compared between the numerical and experimental results (Fig. 21 and Fig. 22), the mean numerical value is evidently lower than in the experimental result. However, the experimental results show only the maximum value, and it shows the 2D-VAC temperature is lower than that in the TC process.

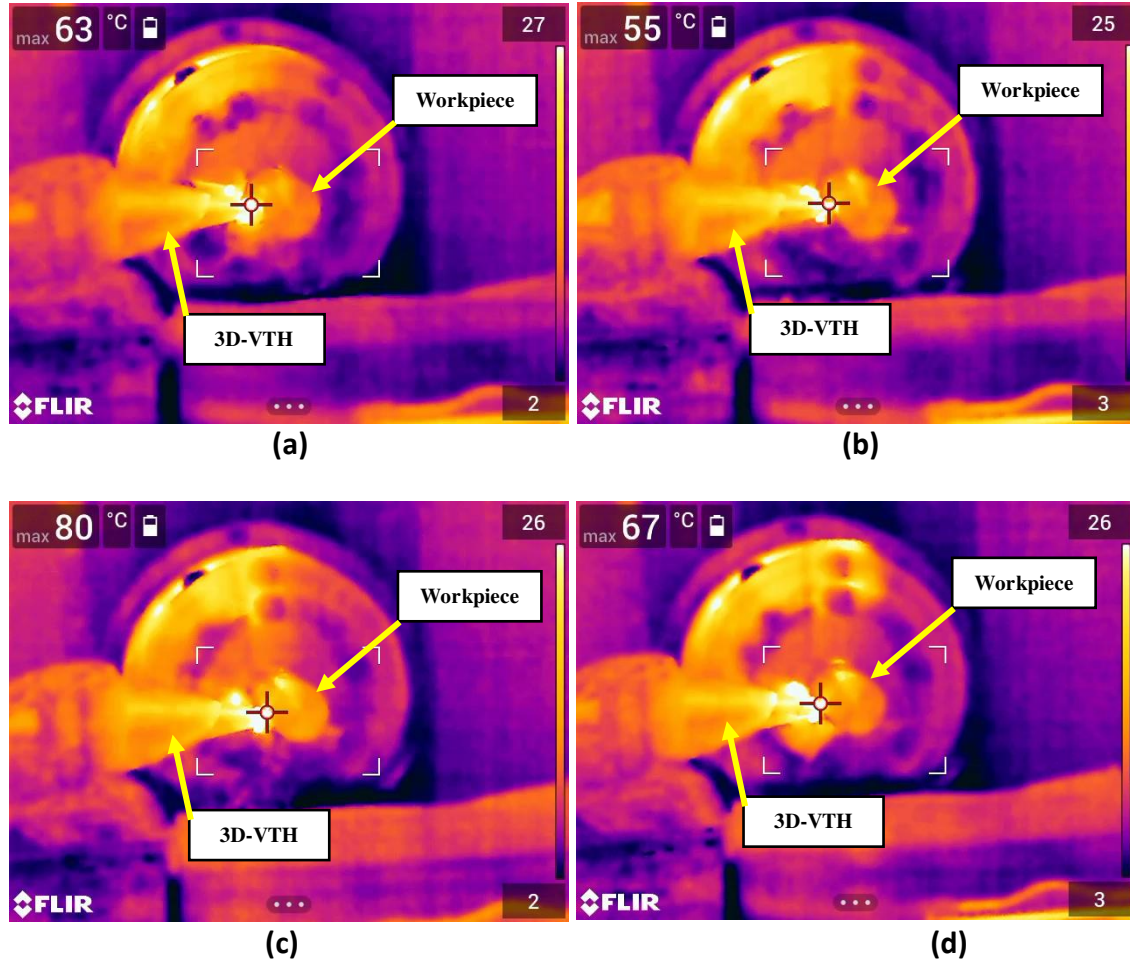


Fig. 22 Temperature measurement using IR camera on the tool tip (a) TC at $V_c = 9$ m/min, (b) 2D-VAC at $V_c = 9$ m/min (c) TC at $V_c = 12$ m/min, and (d) 2D-VAC at $V_c = 12$ m/min

5.5 Simulated Residual Stress

The residual stress reveals the condition of the machined surface after machining in either the tensile or compressive state. Fig. 23 demonstrates the residual stress comparison between TC and 2D-VAC process at $V_c = 9$ m/min and $V_c = 12$ m/min. The residual stress is captured under three different locations: the left (about 167 μm away from the edge of the beginning of cutting), center (about 250 μm away), and right position (about 333 μm away).

The residual pattern for both methods starts from the compressive stress state (negative value) and then grows to the tensile stress state (positive value) before achieving steady-state conditions (about zero value). In the case of the TC process, the compressive stress state grows high, which starts from the left to the right position because of the non-uniform cutting load under serrated chip cutting load. Meanwhile, in the case of the 2D-VAC process, the compressive stress state is relatively similar due to uniformity of the cutting load under serrated chip cutting load.

It can be clearly seen that the 2D-VAC process has a deeper pattern of the compressive stress, which is larger than that in the TC process. In the case of the right position (blue line), the compressive stress could reach 400 MPa for 2D-VAC at $V_c = 9$ m/min (Fig. 23 (b)). The compressive stress in the TC process is only 150 MPa (Fig. 23(a)). The mechanical effects such as the vibration impact of the tool edge and the vibration velocity greatly affect the compressive stress for the 2D-VAC process.

In addition, the tensile stress is also high in the 2D-VAC, which is probably due to higher cutting temperature on the machined surface or the tertiary deformation zone, as indicated in Fig. 20 in the simulation results. The thermal effect generally sensitizes to the tensile stress due to molecular size deformation under high temperature. Moreover, as the cutting velocity is increased for both methods, the compressive and tensile stress peaks also increase (Fig. 23 (c) and (d)).

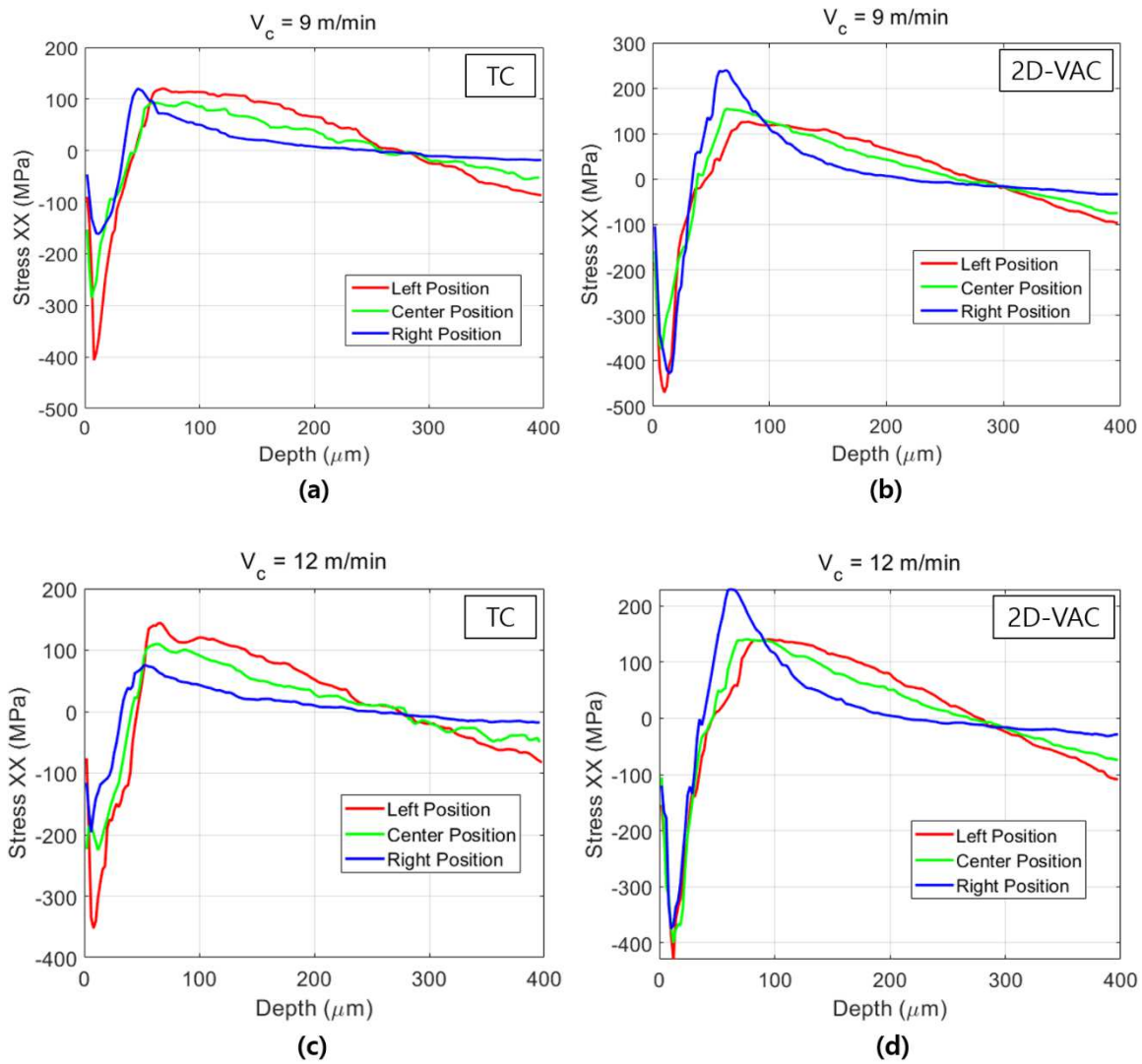


Fig. 23 Residual stress comparison between TC and 2D-VAC, **(a, b)** with $V_c = 9$ m/min, **(c, d)** with $V_c = 12$ m/min

5.5 Chip Formation

Fig. 24 shows the serrated chip generated at $V_c = 5$ m/min for both the TC and the 2D-VAC process. In this case, the cutting velocity is considered in the low range. However, the serrated pattern can still be observed clearly. Under low cutting speed, the serrated pattern for the TC method has been considerably greater than that under the 2D-VAC method, which is caused by the high cutting load. In other words, the sawtooth pattern in the 2D-VAC process is relatively small and has less uniformity, which is believed to be due to low cutting load. The β -phase is clearly seen after the chip is polished and etched by Kroll reagent. It can be seen for both processes that high shear distortion/deformation for the β -phase occurs near the adiabatic shear band. There is a significant shear distortion flow of the β -phase near the rake-chip sliding surface.

Fig. 25 shows the serrated chip generated at $V_c = 7$ m/min for both the TC and the 2D-VAC process. Similarly, it is observed that the sawtooth pattern in the 2D-VAC is small and has less uniformity. Under higher cutting speed, crack formation has been observed along the adiabatic shear band. It is believed that high strain and high strain rate occur along the adiabatic shear band in the TC process. However, there is no indication of a large crack along the adiabatic shear band in the 2D-VAC process, which indicates low cutting load.

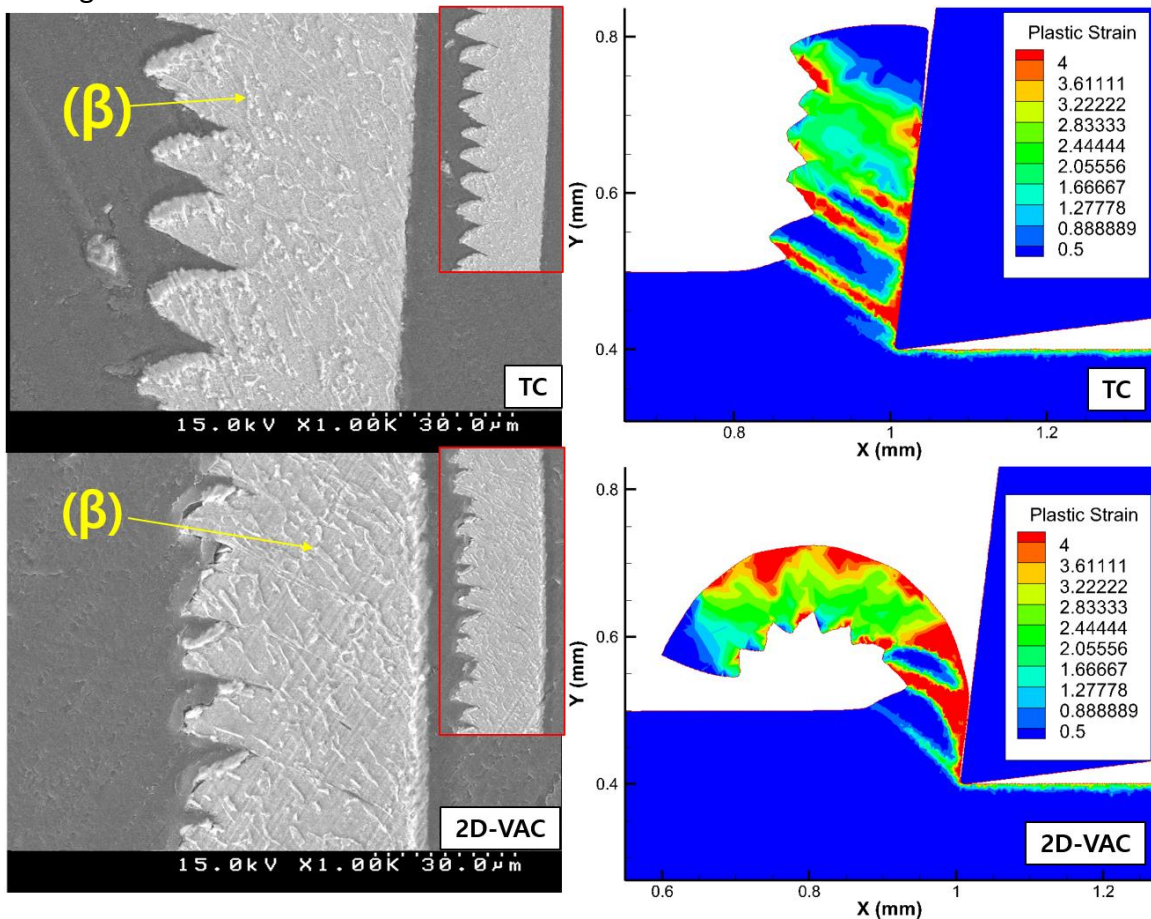


Fig. 24 Chip formation comparison between the TC and the 2D-VAC at $V_c = 5$ m/min

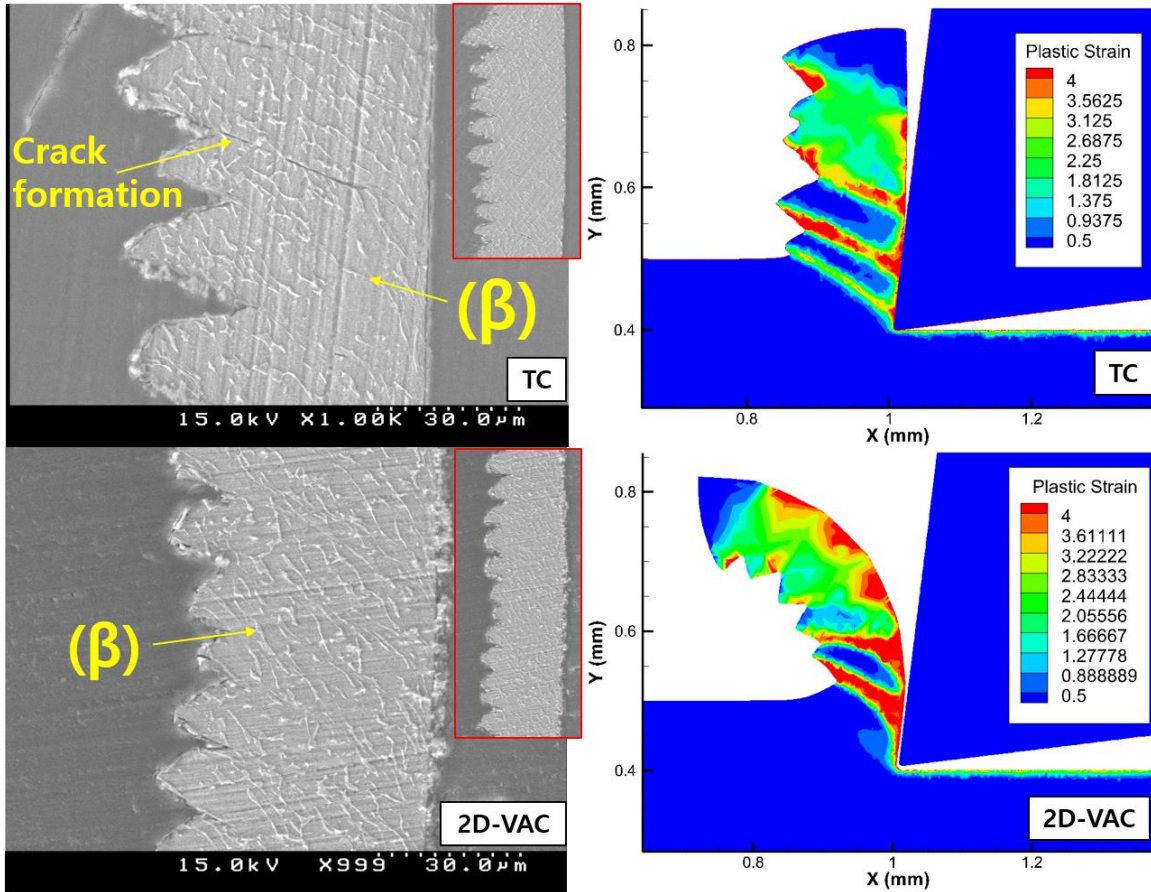


Fig. 25 Chip formation comparison between the TC and the 2D-VAC at $V_c = 7$ m/min

5.6 Micro-hardness and micro-structure

Fig. 26 reveals the results for the experimental micro-Vickers hardness comparison between the TC and the 2D-VAC method at $V_c = 12$ m/min and $V_c = 9$ m/min. The micro-Vickers hardness has been investigated under 300 gForce for $V_c = 12$ m/min and 100 gForce for $V_c = 9$ m/min. However, the pattern is typically similar. Thus, different pressure of the diamond Vickers does not affect the results. The micro-Vickers hardness has been captured with a machined surface of depth up to 500 μ m and 600 μ m.

Typically, the micro-Vickers hardness starts with a high value and then decreases after the depth of 350 μ m, and the micro-Vickers hardness becomes relatively steady. The experimental results showed that the micro-Vickers hardness near the machined surface is high for the TC process. Meanwhile, a lower hardness occurs for the 2D-VAC process, as shown in Fig. 26 with the blue lines. This micro-hardness results indicate that higher cutting energy occurs in the TC process. It can be understood that the machined surface experiences an intermittent cutting process in the 2D-VAC. Thus, less shear deformation and stress occur, and the machined surface does not change too much from the original state before cutting.

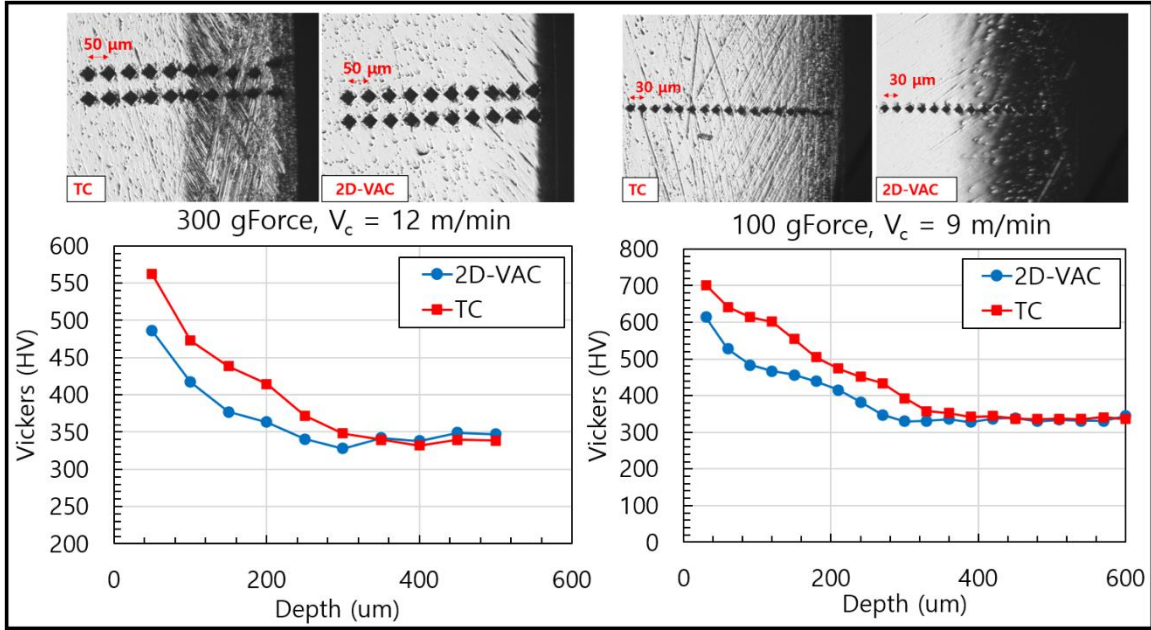
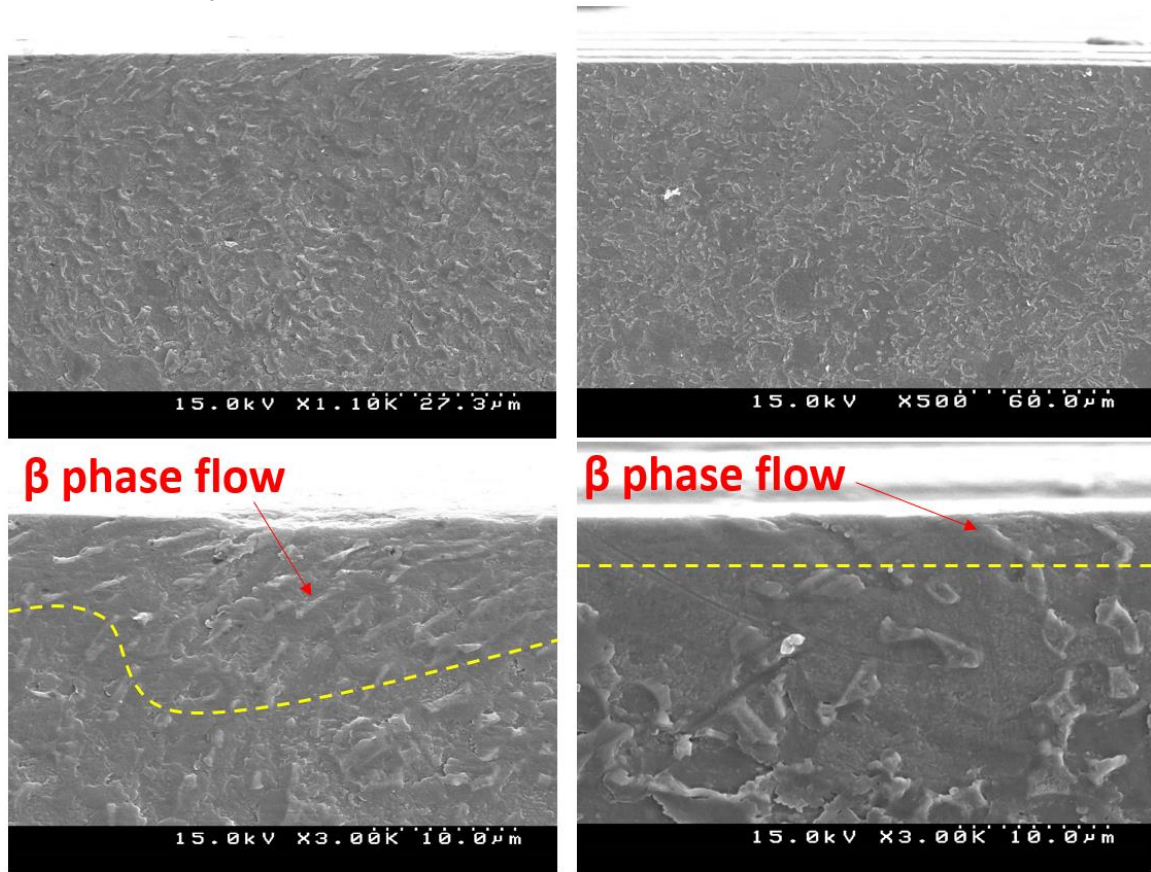


Fig. 26 Micro-hardness comparison between the TC and the 2D-VAC method under $V_c = 12$ m/min and $V_c = 9$ m/min.



(a) TC $V_c = 12$ m/min

(b) 2D-VAC $V_c = 12$ m/min

Fig. 27 Micro-structure comparison between (a) TC and (b) 2D-VAC process

Fig. 27 reveals the experimental results for the micro-structure of the machine surface layer after mirror polishing and using the Kroll reagent in SEM images. The results clearly show the β -phase flow due to shearing deformation in a large portion under the TC process. Meanwhile, the β -phase flow due to shearing deformation occurs less in the 2D-VAC process. The depth portion of the β -phase flow is approximately from 10 μm to 20 μm since the shearing deformation is not uniform in the TC process. Meanwhile, for 2D-VAC, the depth portion of the β -phase flow is less than 5 μm . This experimental information reveals that the 2D-VAC has less shearing deformation when compared to the TC process.

CONCLUSIONS

In this study, numerical and the experimental results during the TC and the 2D-VAC process during Ti6Al4V cutting have been conducted. Additionally, validation of the analytical cutting force model of the 2D-VAC process with a numerical solution has been presented as well. The concluding remarks of this study are pointed out below:

- According to the von Mises distribution contour, the stress distribution in the 2D-VAC can be lower than in the TC process because of the tool retraction effect. However, its value can be equal to the one in the TC process (about 1100 to 1200 MPa) when steady-state cutting occurs. The plastic strain in the 2D-VAC can be higher than that in the TC process. According to the numerical results, the plastic strain in the 2D-VAC is high near the chip-rake contact zone (secondary deformation zone).
- The proposed analytical cutting force model for the 2D-VAC based on transient modified Johnson-Cook shear flow, the transient shear strain rate, the transient TOC, and the transient shear angle shows good agreement with the numerical solution and can be used to predict or even analyze the 2D-VAC process during the cutting of Ti6Al4V.
- Numerical analysis of the temperature value in the deformation shows that in the case of the 2D-VAC, its value could be lower than that in the TC process because of the tool retraction effect. This was proved with the experimental results. However, the peak cutting tool temperature could be higher than that in the TC process.
- Residual stress simulation shows that in the case of the 2D-VAC, the compressive stress could be high. More mechanical effects such as the vibration impact of the tool edge and the vibration velocity are considered as the main causes. Additionally, the serrated chip in the 2D-VAC is curlier when compared to the TC process. The sawtooth pattern in the 2D-VAC process is relatively small and has less uniformity because of the low cutting load.

- A lower hardness occurs in the 2D-VAC process, which indicates less shear deformation on the machine surface, and it does not change too much from the original state. This was confirmed with micro-structure surface results, in which the β -phase flow deformation had less occurrence in the 2D-VAC process.

FUNDING

This study was supported by the Basic Science Research Program through the National Research Foundation of Korea (NRF) and funded by the Ministry of Science, ICT, and Future Planning [Grant Number NRF-2020R1A2B5B02001755].

CONFLICTS OF INTEREST

Authors declare that there are no conflicts of interest in this manuscript. The authorship and funding have been declared properly.

AVAILABILITY OF DATA AND MATERIAL

Not available

CODE AVAILABILITY

Not available

ETHICS APPROVAL

Not applicable

CONSENT TO PARTICIPATE

Not applicable

CONSENT FOR PUBLICATION

Not applicable

AUTHOR'S CONTRIBUTION

Rendi Kurniawan: Writing – original draft, Methodology, Conceptualization, Investigation, Formal Analysis.

Farooq Ahmed: Resources.

Gun Chul Park: Validation.

Tae Jo Ko: Writing – review & editing, Supervision, Project Administration.

NOMENCLATURE

$x_e(t)$	The tool movement in x-direction at the CC-point as function of time
$y_e(t)$	The tool movement in y-direction at the CC-point as function of time
a_m	The elliptical locus magnitude in x-direction
b_m	The elliptical locus magnitude in y-direction
f_v	The frequency vibration of the tool movement in Hz
φ	The phase difference between cosine wave in radian
t	The time in second
V_c	The constant cutting speed of the cutting tool in $\mu\text{m/s}$
f	The feed rate, $\mu\text{m/rev}$
r_e	The cutting edge radius in μm
$\theta_t(t)$	The slope angle of the tool movement
$V_x(t)$	The velocity vector of the tool movement in x-direction
$V_y(t)$	The velocity vector of the tool movement in y-direction
$V_t(t)$	The transient tool velocity
$TOC_t(t)$	The transient thickness of cut as function of time
TOC_{max}	The maximum of transient thickness of cut
t_A	Tool engaging time at the point A
t_A'	Tool engaging time in previous cycle at the point A
t_D	Tool disengaging time at the point D
t_P	Toll disengaging time in the previous one-cycle at point P
t_r	Tool engaging time lies between the point A and B
$\phi_s(t)$	Transient shear angle as function of time
ϕ_{kc}	The constant shear angle of the CC-like process
ϕ_{kr}	The constant shear angle of the kinetic reverse process
β	The friction angle
α_o	The constant rake angle
$\varepsilon(t)$	The transient shear strain
$\dot{\varepsilon}(t)$	The transient shear strain rate
Δd	The thickness between two sequences segmented chip
Δs	The elongation of workpiece material during shear deformation
$\tau_s(t)$	The modified Johnson-Cook flow stress
A, B, C, n, m	The constant Johnson-Cook parameters
$F_s(t)$	The transient shear force
$F_R(t)$	The transient resultant force
$F_c(t)$	The transient principal force

$F_t(t)$	The transient thrust force
----------	----------------------------

REFERENCES

- [1] M. Lu, B. Chen, D. Zhao, J. Zhou, J. Lin, A. Yi, H. Wang, Chatter Identification of Three-Dimensional Elliptical vibration Cutting Process Based on Empirical Mode Decomposition and Feature Extraction, *Appl. Sci.* 9 (2018) 21. <https://doi.org/10.3390/app9010021>.
- [2] S.J. Zhang, S. To, G.Q. Zhang, Z.W. Zhu, A review of machine-tool vibration and its influence upon surface generation in ultra-precision machining, *Int. J. Mach. Tools Manuf.* 91 (2015) 34–42. <https://doi.org/10.1016/j.ijmachtools.2015.01.005>.
- [3] Z. Yang, L. Zhu, G. Zhang, C. Ni, B. Lin, Review of ultrasonic vibration-assisted machining in advanced materials, *Int. J. Mach. Tools Manuf.* 156 (2020) 103594. <https://doi.org/10.1016/j.ijmachtools.2020.103594>.
- [4] F. Ning, W. Cong, Ultrasonic vibration-assisted (UV-A) manufacturing processes: State of the art and future perspectives, *J. Manuf. Process.* 51 (2020) 174–190. <https://doi.org/10.1016/j.jmapro.2020.01.028>.
- [5] J. Zhang, T. Cui, C. Ge, Y. Sui, H. Yang, Review of micro/nano machining by utilizing elliptical vibration cutting, *Int. J. Mach. Tools Manuf.* 106 (2016) 109–126. <https://doi.org/10.1016/j.ijmachtools.2016.04.008>.
- [6] G. Quintana, J. Ciurana, Chatter in machining processes: A review, *Int. J. Mach. Tools Manuf.* 51 (2011) 363–376. <https://doi.org/10.1016/j.ijmachtools.2011.01.001>.
- [7] A. Otto, G. Radons, Application of spindle speed variation for chatter suppression in turning, *CIRP J. Manuf. Sci. Technol.* 6 (2013) 102–109. <https://doi.org/10.1016/j.cirpj.2013.02.002>.
- [8] D. Ulutan, T. Ozel, Machining induced surface integrity in titanium and nickel alloys: A review, *Int. J. Mach. Tools Manuf.* 51 (2011) 250–280. <https://doi.org/10.1016/j.ijmachtools.2010.11.003>.
- [9] X. Liang, Z. Liu, B. Wang, State-of-the-art of surface integrity induced by tool wear effects in machining process of titanium and nickel alloys: A review, *Meas. J. Int. Meas. Confed.* 132 (2019) 150–181. <https://doi.org/10.1016/j.measurement.2018.09.045>.
- [10] D. Yang, Z. Liu, X. Ren, P. Zhuang, Hybrid modeling with finite element and statistical methods for residual stress prediction in peripheral milling of titanium alloy Ti-6Al-4V, *Int. J. Mech. Sci.* 108–109 (2016) 29–38. <https://doi.org/10.1016/j.ijmecsci.2016.01.027>.
- [11] C.M. Rao, S.S. Rao, M.A. Herbert, Development of novel cutting tool with a micro-hole pattern on PCD insert in machining of titanium alloy, *J. Manuf. Process.* 36 (2018) 93–103. <https://doi.org/10.1016/j.jmapro.2018.09.028>.
- [12] R. Muhammad, M.S. Hussain, A. Maurotto, C. Siemers, A. Roy, V. V. Silberschmidt, Analysis of a free machining $\alpha+\beta$ titanium alloy using conventional and

- ultrasonically assisted turning, *J. Mater. Process. Technol.* 214 (2014) 906–915. <https://doi.org/10.1016/j.jmatprotec.2013.12.002>.
- [13] J. Zang, J. Zhao, A. Li, J. Pang, Serrated chip formation mechanism analysis for machining of titanium alloy Ti-6Al-4V based on thermal property, *Int. J. Adv. Manuf. Technol.* 98 (2018) 119–127. <https://doi.org/10.1007/s00170-017-0451-6>.
- [14] M. Calamaz, D. Coupard, F. Girot, A new material model for 2D numerical simulation of serrated chip formation when machining titanium alloy Ti-6Al-4V, *Int. J. Mach. Tools Manuf.* 48 (2008) 275–288. <https://doi.org/10.1016/j.ijmachtools.2007.10.014>.
- [15] M. Sima, T. Özel, Modified material constitutive models for serrated chip formation simulations and experimental validation in machining of titanium alloy Ti-6Al-4V, *Int. J. Mach. Tools Manuf.* 50 (2010) 943–960. <https://doi.org/10.1016/j.ijmachtools.2010.08.004>.
- [16] R. Kurniawan, S.T. Kumaran, S. Ali, D.A. Nurcahyaningasih, G. Kiswanto, T.J. Ko, Experimental and analytical study of ultrasonic elliptical vibration cutting on AISI 1045 for sustainable machining of round-shaped microgroove pattern, *Int. J. Adv. Manuf. Technol.* 98 (2018) 2031–2055. <https://doi.org/10.1007/s00170-018-2359-1>.
- [17] E. Shamoto, T. Moriwaki, Study on Elliptical Vibration Cutting, *CIRP Ann. - Manuf. Technol.* 43 (1994) 35–38. [https://doi.org/10.1016/S0007-8506\(07\)62158-1](https://doi.org/10.1016/S0007-8506(07)62158-1).
- [18] R. Tan, X. Zhao, S. Guo, X. Zou, Y. He, Y. Geng, Z. Hu, T. Sun, Sustainable production of dry-ultra-precision machining of Ti-6Al-4V alloy using PCD tool under ultrasonic elliptical vibration-assisted cutting, *J. Clean. Prod.* 248 (2020) 119254. <https://doi.org/10.1016/j.jclepro.2019.119254>.
- [19] Q. Wang, Y. Wu, J. Gu, D. Lu, Y. Ji, M. Nomura, Fundamental Machining Characteristics of the In-base-plane Ultrasonic Elliptical Vibration Assisted Turning of Inconel 718, *Procedia CIRP.* 42 (2016) 858–862. <https://doi.org/10.1016/j.procir.2016.03.008>.
- [20] J. Zhang, L. Han, J. Zhang, H. Liu, Y. Yan, T. Sun, Brittle-to-ductile transition in elliptical vibration-assisted diamond cutting of reaction-bonded silicon carbide, *J. Manuf. Process.* 45 (2019) 670–681. <https://doi.org/10.1016/j.jmapro.2019.08.005>.
- [21] R. Kurniawan, G. Kiswanto, T.J. Ko, Micro-dimple pattern process and orthogonal cutting force analysis of elliptical vibration texturing, *Int. J. Mach. Tools Manuf.* 106 (2016) 127–140. <https://doi.org/10.1016/j.ijmachtools.2016.03.007>.
- [22] Y. Yang, Y. Pan, P. Guo, Structural coloration of metallic surfaces with micro/nano-structures induced by elliptical vibration texturing, *Appl. Surf. Sci.* 402 (2017) 400–409. <https://doi.org/10.1016/j.apsusc.2017.01.026>.
- [23] H.N. Hosseinabadi, S.A. Sajjadi, S. Amini, Creating micro textured surfaces for the improvement of surface wettability through ultrasonic vibration assisted turning, *Int. J. Adv. Manuf. Technol.* 96 (2018) 2825–2839. <https://doi.org/10.1007/s00170-018-1580-2>.

- [24] X. Zhang, a. Senthil Kumar, M. Rahman, C. Nath, K. Liu, An analytical force model for orthogonal elliptical vibration cutting technique, *J. Manuf. Process.* 14 (2012) 378–387. <https://doi.org/10.1016/j.jmapro.2012.05.006>.
- [25] R. Kurniawan, G. Kiswanto, T.J. Ko, Surface roughness of two-frequency elliptical vibration texturing (TFEVT) method for micro-dimple pattern process, *Int. J. Mach. Tools Manuf.* 116 (2017) 77–95. <https://doi.org/10.1016/j.ijmachtools.2016.12.011>.
- [26] C. Kong, D. Wang, Numerical investigation of the performance of elliptical vibration cutting in machining of AISI 1045 steel, *Int. J. Adv. Manuf. Technol.* 98 (2018) 715–727. <https://doi.org/10.1007/s00170-018-2277-2>.
- [27] H. Xie, Z. Wang, Study of cutting forces using FE, ANOVA, and BPNN in elliptical vibration cutting of titanium alloy Ti-6Al-4V, *Int. J. Adv. Manuf. Technol.* 105 (2019) 5105–5120. <https://doi.org/10.1007/s00170-019-04537-w>.
- [28] Y. Liang, D. Li, Q. Bai, S. Wang, M. Chen, Molecular dynamics simulation of elliptical vibration cutting, *Proc. 1st IEEE Int. Conf. Nano Micro Eng. Mol. Syst. 1st IEEE-NEMS.* (2006) 635–638. <https://doi.org/10.1109/NEMS.2006.334862>.
- [29] M. Lotfi, S. Amini, J. Akbari, Surface integrity and microstructure changes in 3D elliptical ultrasonic assisted turning of Ti-6Al-4V: FEM and experimental examination, *Tribol. Int.* (2020) 106492. <https://doi.org/10.1016/j.triboint.2020.106492>.
- [30] J. Zhang, D. Wang, Investigations of tangential ultrasonic vibration turning of Ti6Al4V using finite element method, *Int. J. Mater. Form.* 12 (2019) 257–267. <https://doi.org/10.1007/s12289-018-1402-y>.
- [31] X. Zhang, a. S. Kumar, M. Rahman, K. Liu, Modeling of the effect of tool edge radius on surface generation in elliptical vibration cutting, *Int. J. Adv. Manuf. Technol.* 65 (2013) 35–42. <https://doi.org/10.1007/s00170-012-4146-8>.
- [32] W. Bai, R. Sun, Y. Gao, J. Leopold, Analysis and modeling of force in orthogonal elliptical vibration cutting, *Int. J. Adv. Manuf. Technol.* 83 (2016) 1025–1036. <https://doi.org/10.1007/s00170-015-7645-6>.
- [33] L. Jieqiong, H. Jinguo, Z. Xiaoqin, H. Zhaopeng, L. Mingming, Study on predictive model of cutting force and geometry parameters for oblique elliptical vibration cutting, *Int. J. Mech. Sci.* 117 (2016) 43–52. <https://doi.org/10.1016/j.ijmecsci.2016.08.004>.
- [34] M. Shaw, *Metal cutting principles*, 1984, 1st ed, Oxford University Press, United States, 1984. https://scholar.google.pt/scholar?q=metal+cutting+principles&btnG=&hl=pt-PT&as_sdt=0,5#3.
- [35] P.J. Arrazola, A. Garay, L.M. Iriarte, M. Armendia, S. Marya, F. Le Maître, Machinability of titanium alloys (Ti6Al4V and Ti555.3), *J. Mater. Process. Technol.* 209 (2009) 2223–2230. <https://doi.org/10.1016/j.jmatprotec.2008.06.020>.
- [36] C. Li, M. Xu, Z. Yu, L. Huang, S. Li, P. Li, Q. Niu, T.J. Ko, Electrical discharge-assisted milling for machining titanium alloy, *J. Mater. Process. Technol.* 285 (2020) 116785. <https://doi.org/10.1016/j.jmatprotec.2020.116785>.

- [37] R. Vignjevic, N. Djordjevic, T. De Vuyst, S. Gemkow, Modelling of strain softening materials based on equivalent damage force, *Comput. Methods Appl. Mech. Eng.* 335 (2018) 52–68. <https://doi.org/10.1016/j.cma.2018.01.049>.
- [38] B. Müller, U. Renz, S. Hoppe, F. Klocke, Radiation thermometry at a high-speed turning process, *J. Manuf. Sci. Eng. Trans. ASME.* 126 (2004) 488–495. <https://doi.org/10.1115/1.1763188>.

Figures

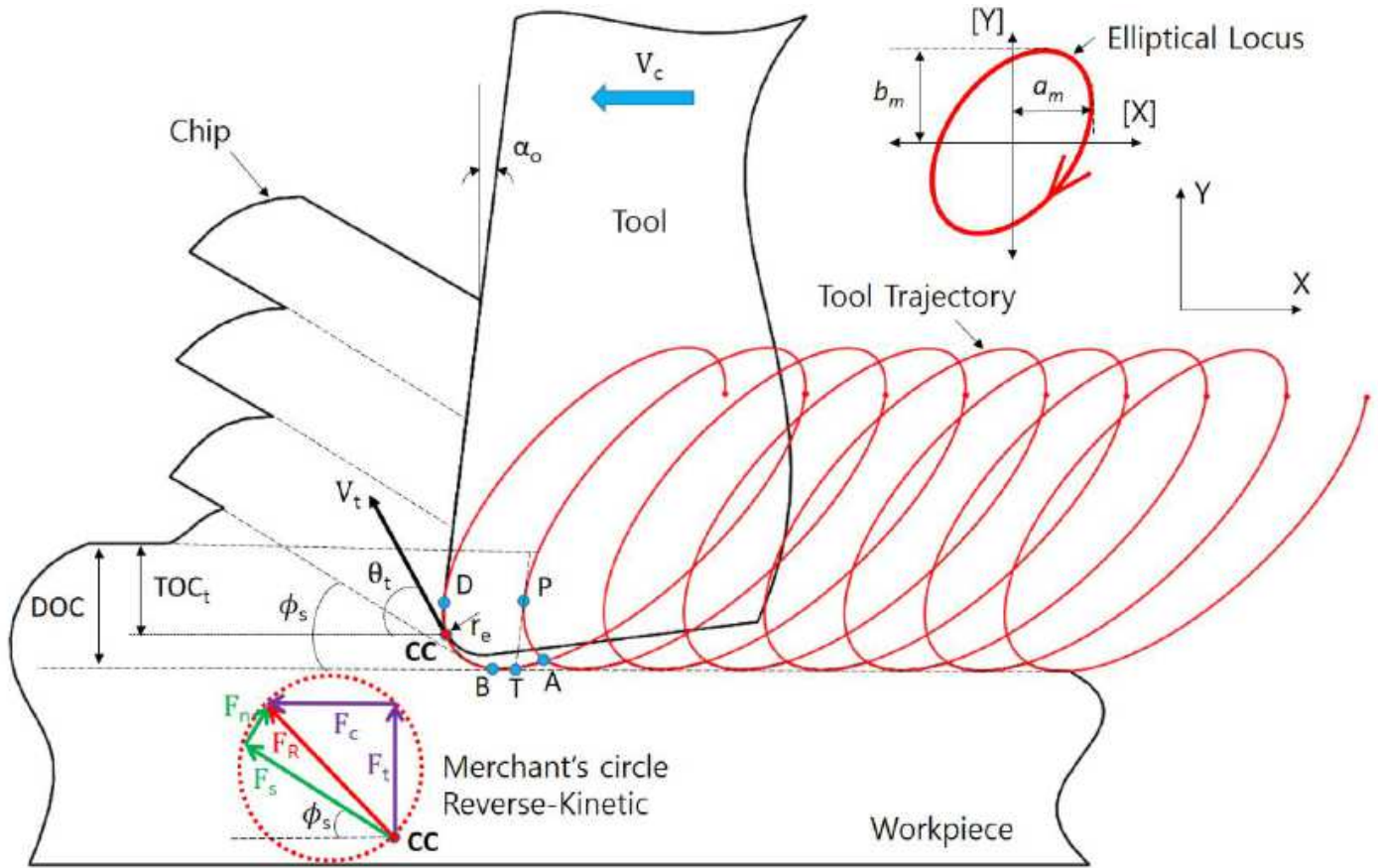


Figure 1

Illustration of 2D-VAC with Merchant's circle reverse-kinetics

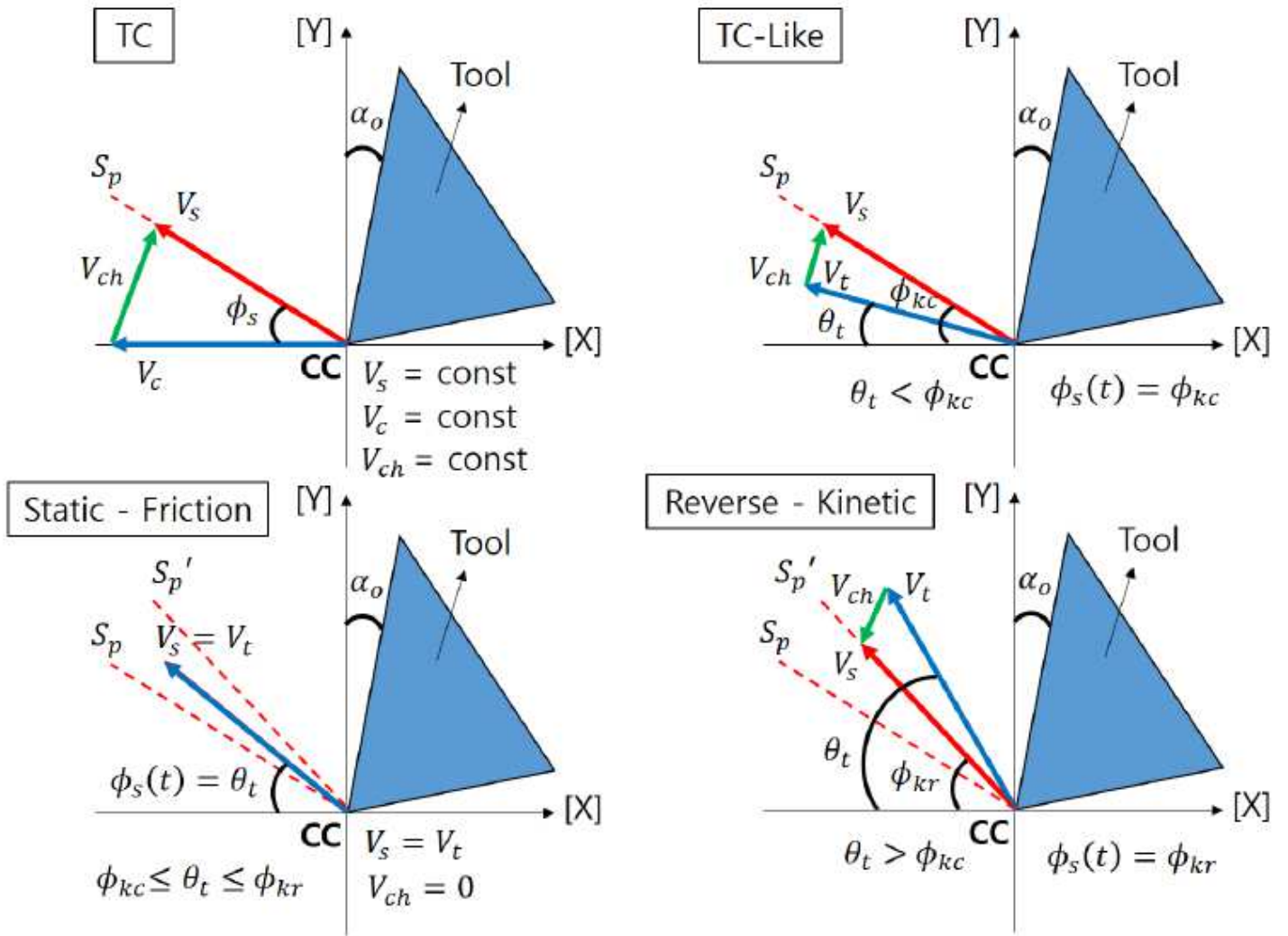


Figure 2

Model of transient shear angle (TC-like, static-friction, and reverse-kinetic) in the 2D-VAC mechanisms

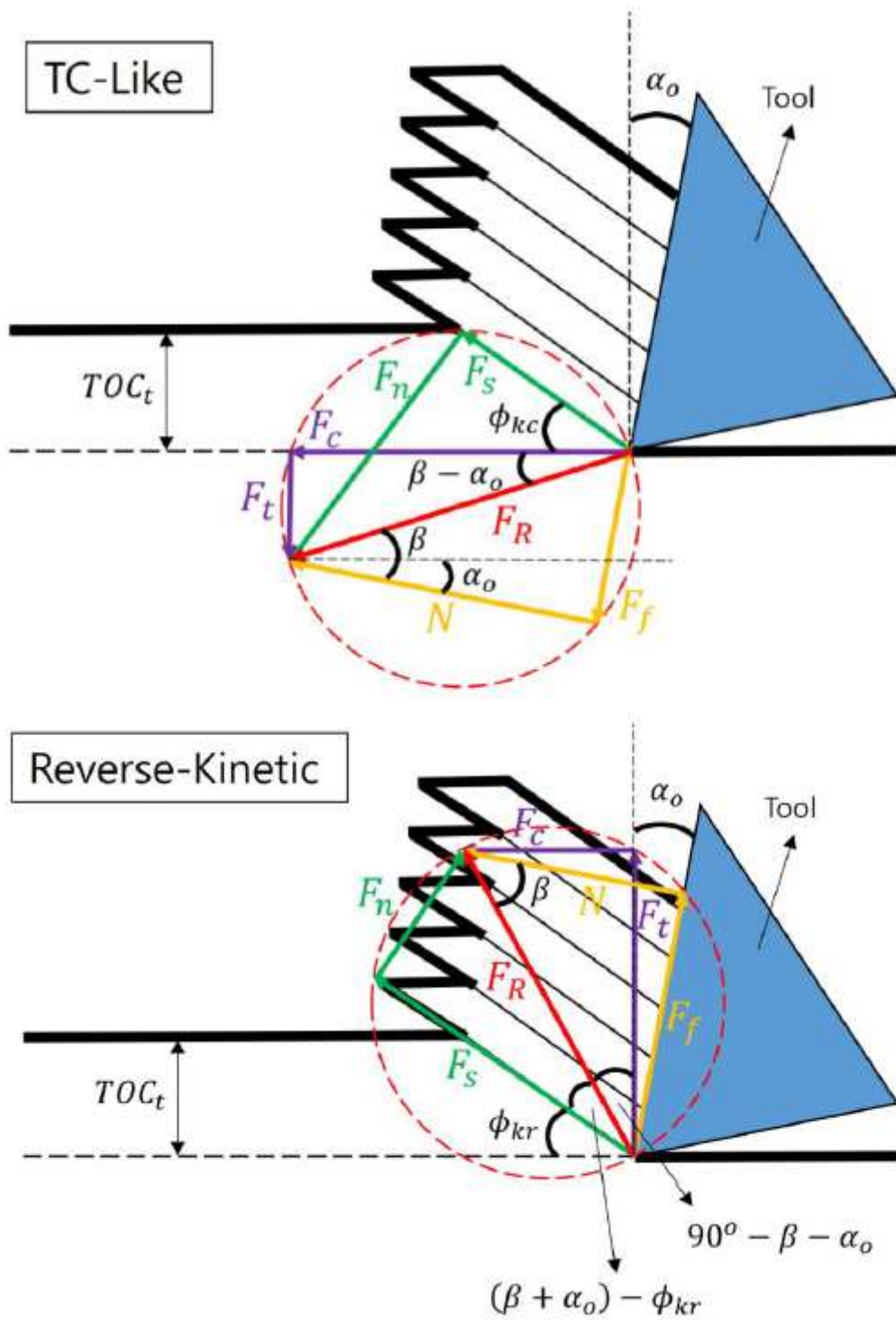


Figure 3

Merchant's circle when TC-like and Reverse-Kinetic cutting

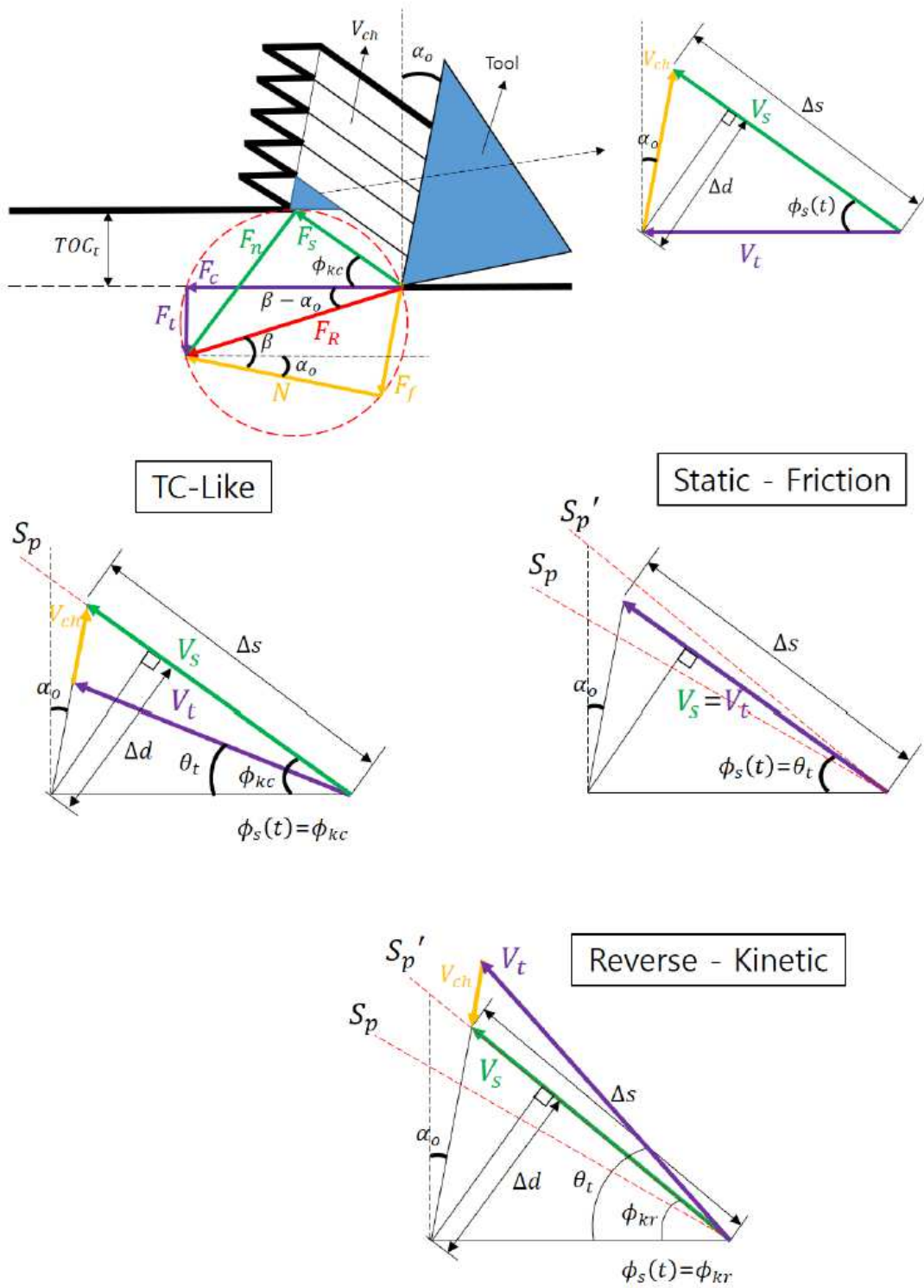


Figure 4

Illustration of transient shear strain in 2D-EVC

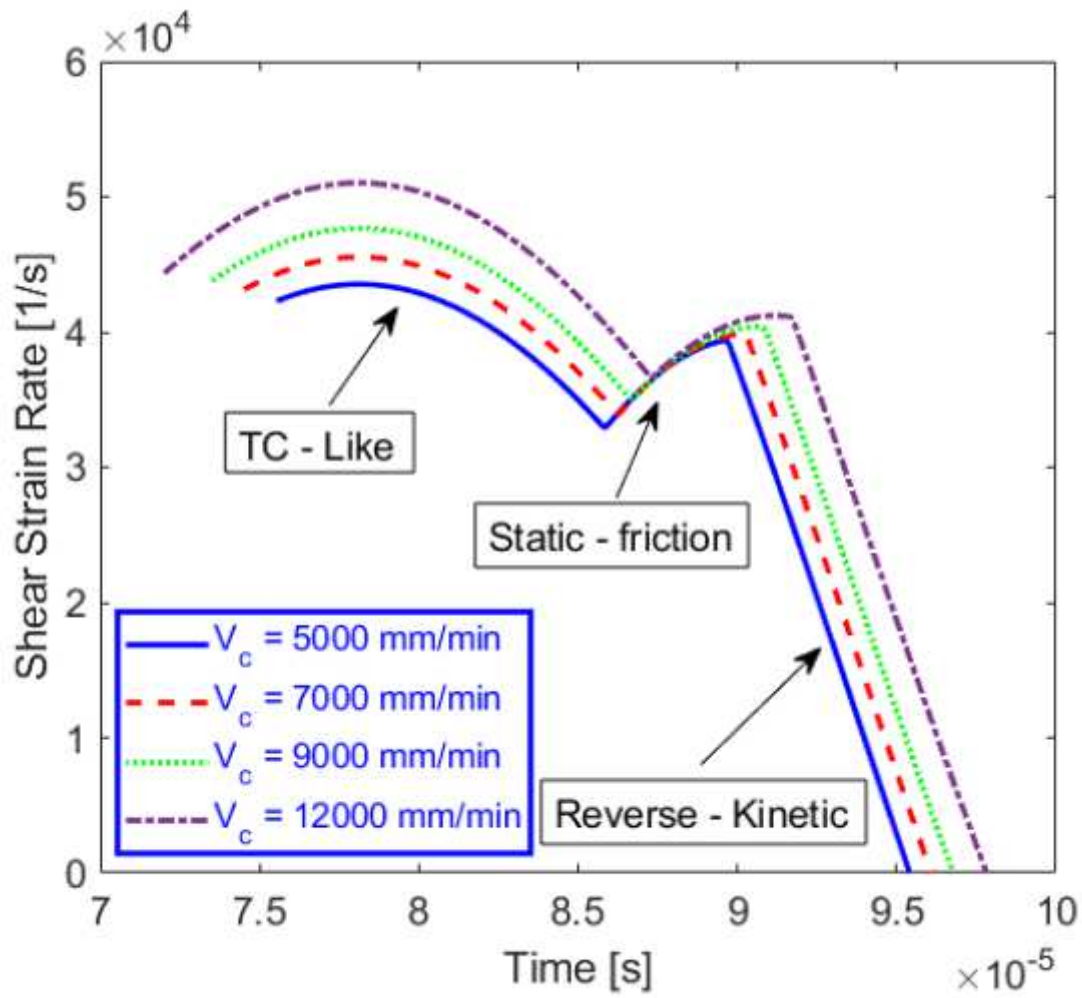


Figure 5

Shear strain rate simulation for 2D-VAC with various cutting speeds V_c

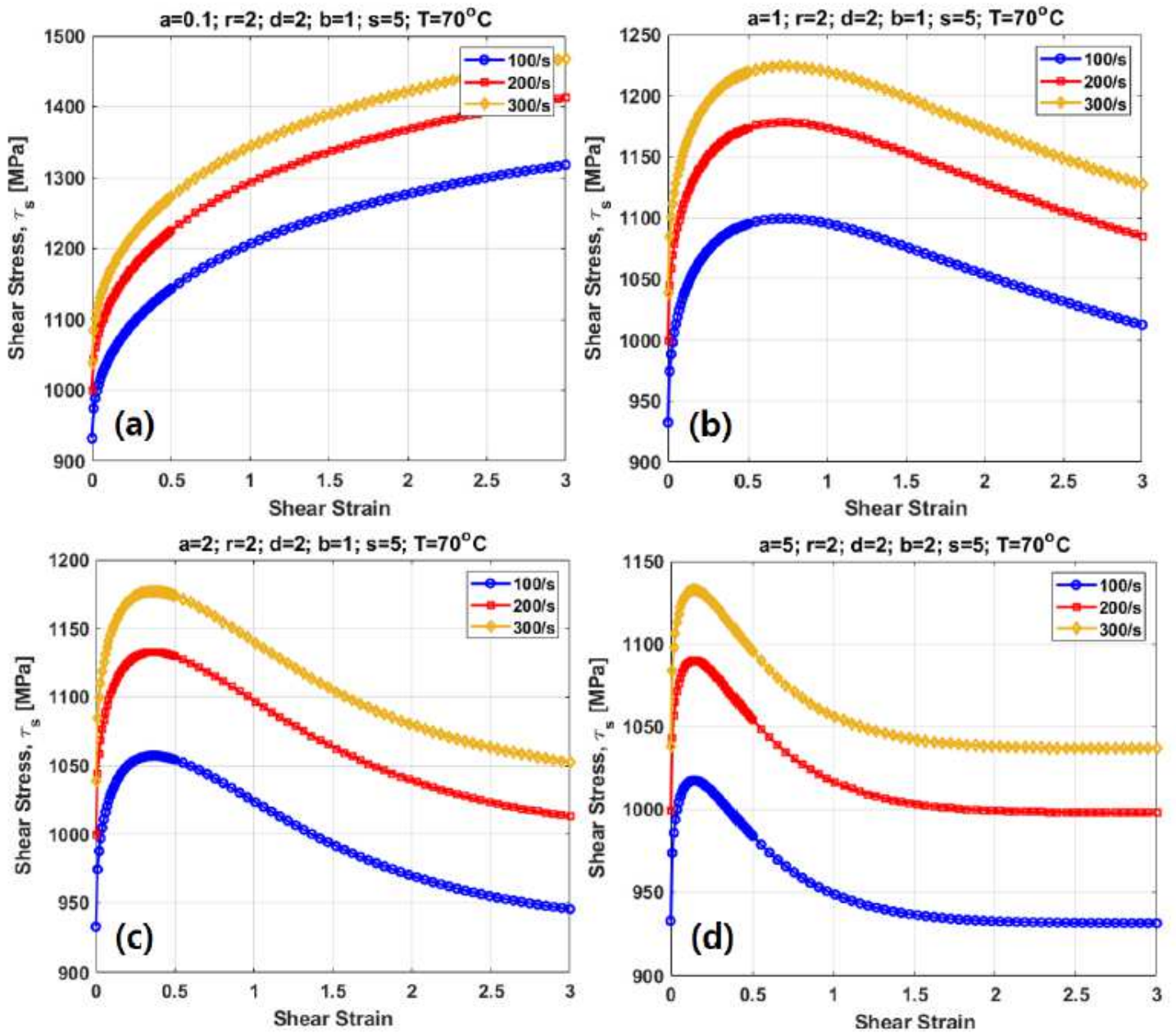


Figure 7

Transient shear stress of modified Johnson-Cook model with variation of variable a . (a) $a=0.1$, (b) $a=1$, (c) $a=2$, (d) $a=5$.

Tool Vibration:

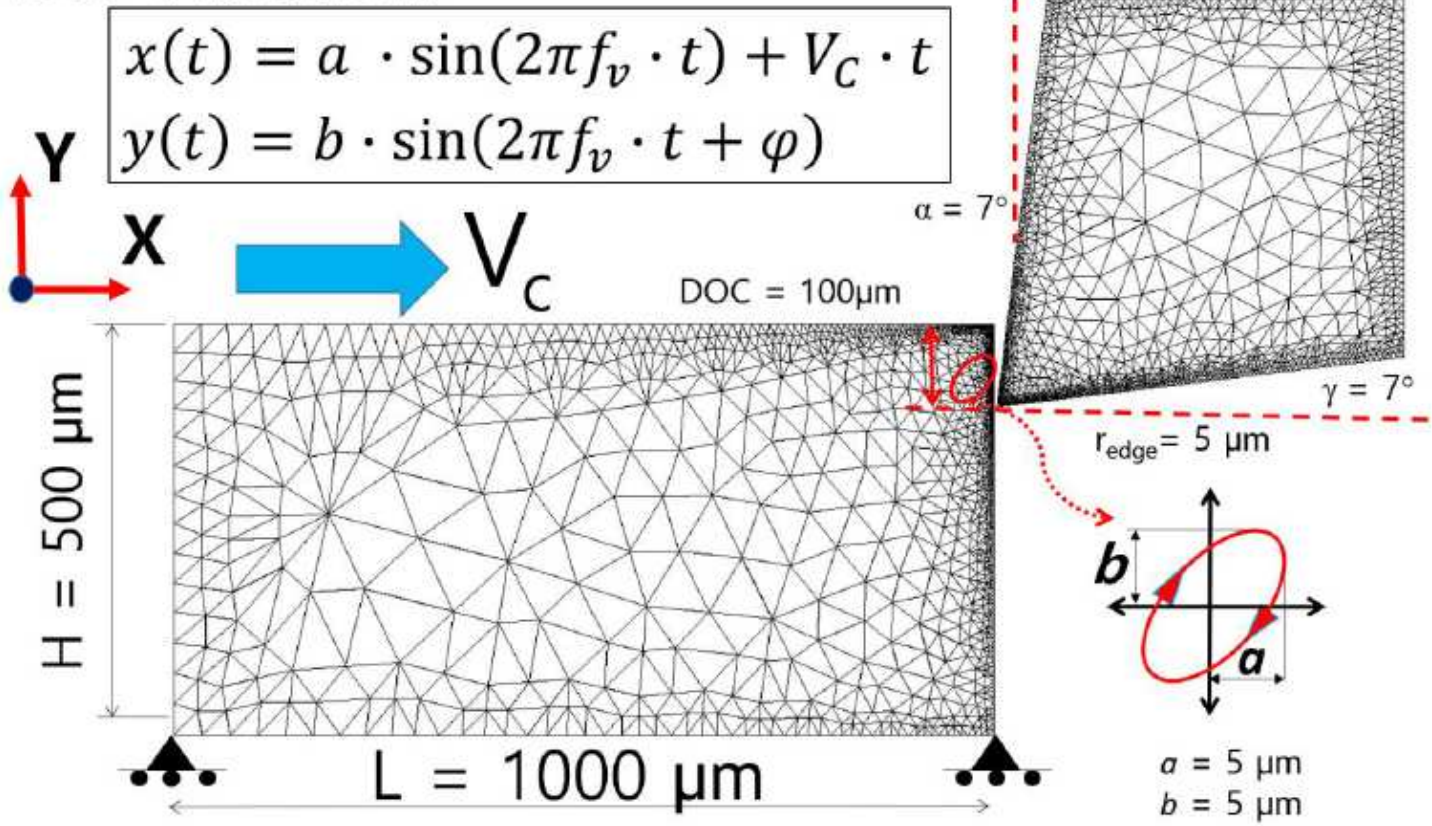


Figure 8

FEA simulation setup for 2D-VAC

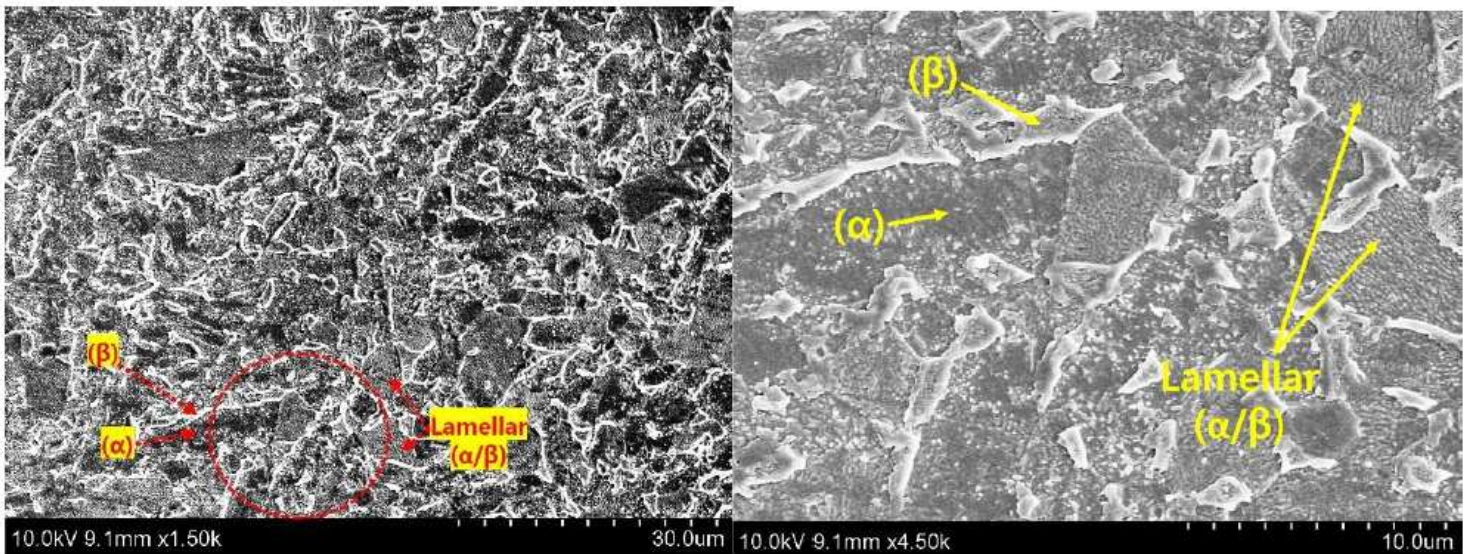


Figure 9

SEM Ti6Al4V metallography after Kroll's etching

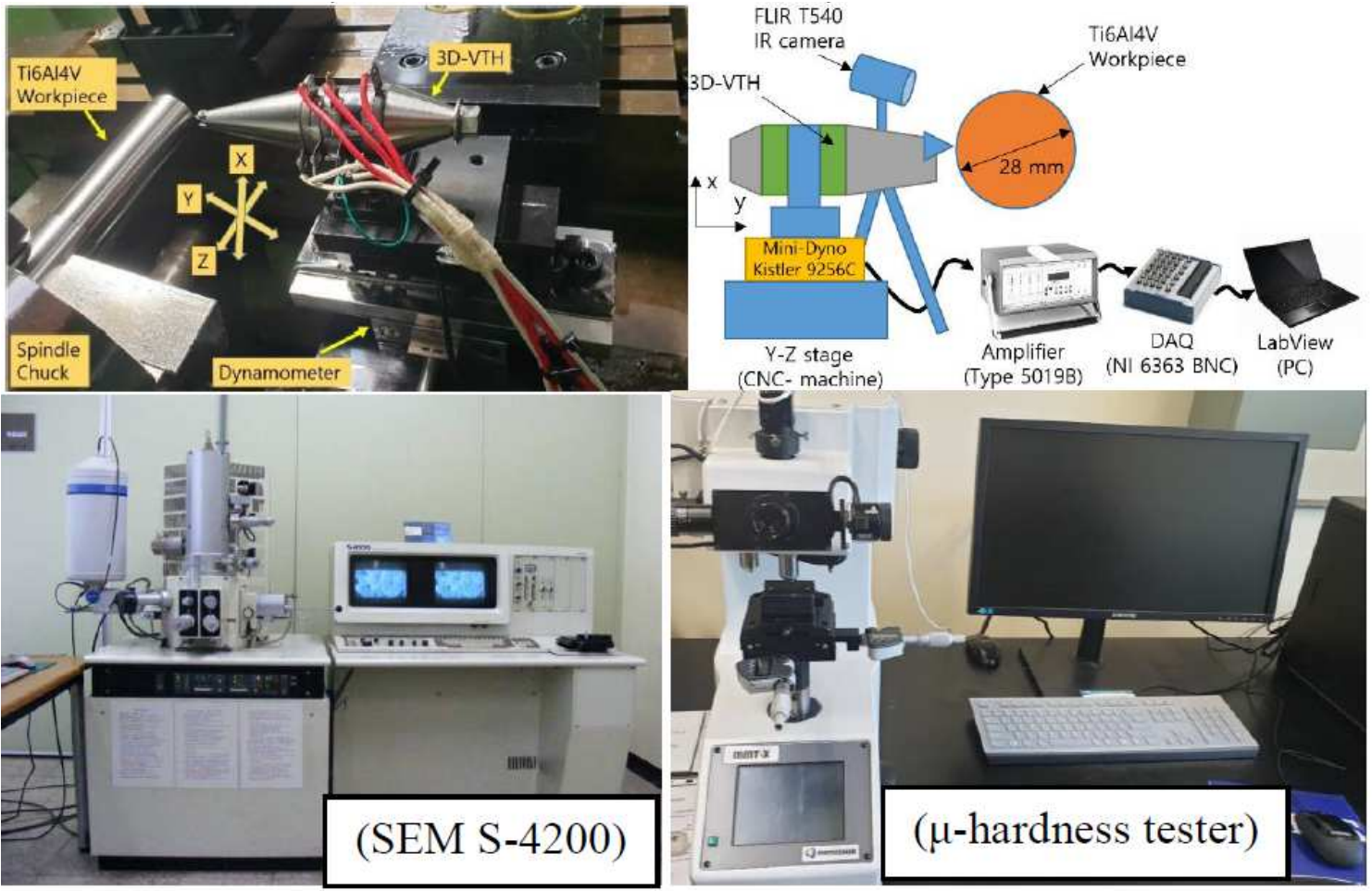


Figure 10

Experimental setup of the 2D-VAC, SEM HITACHI S-4200 and μ -hardness tester

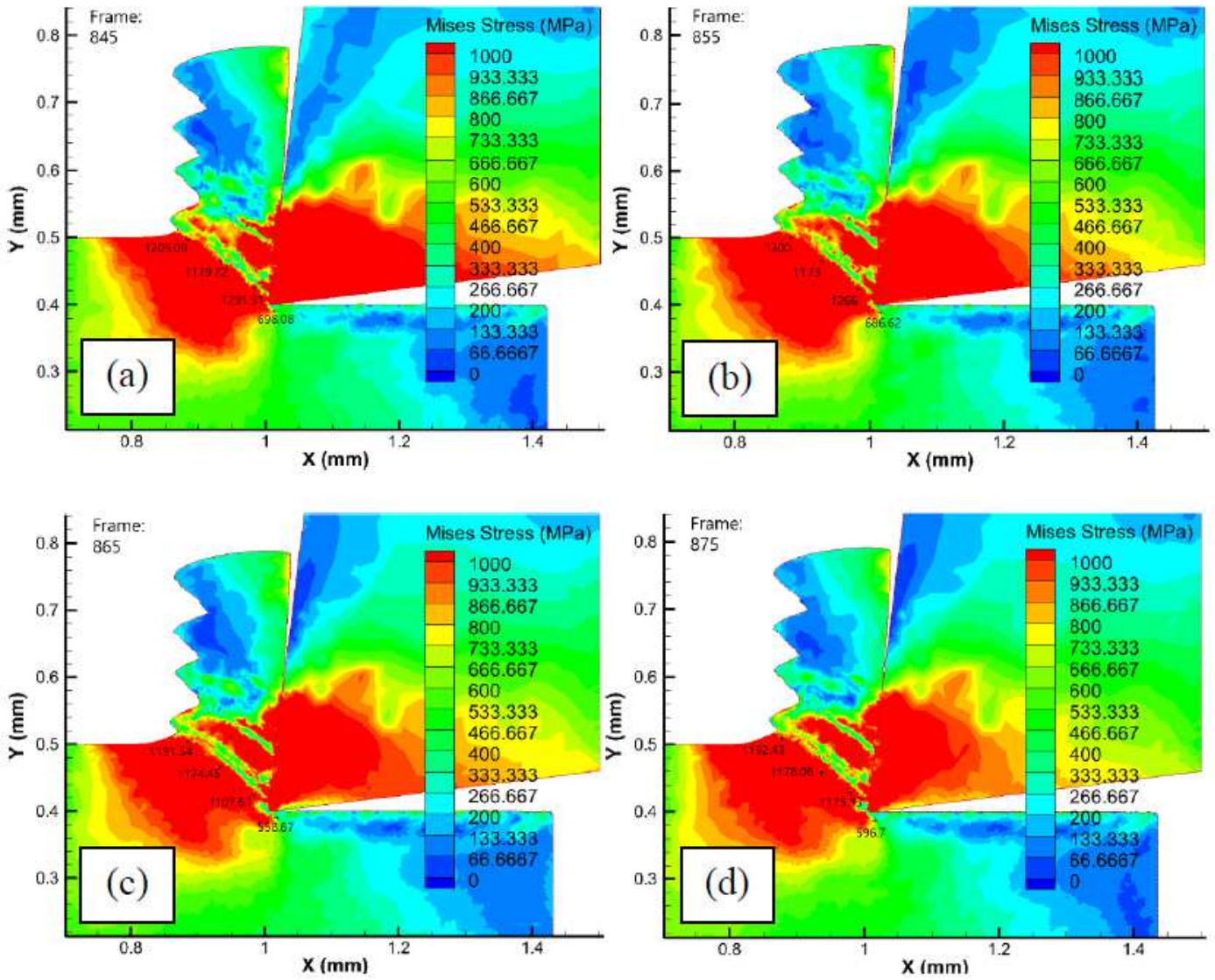


Figure 11

Von Mises stress contour in the TC process at $V_c = 9$ m/min, $f = 100$ μ m/rev, $w = 80$ μ m

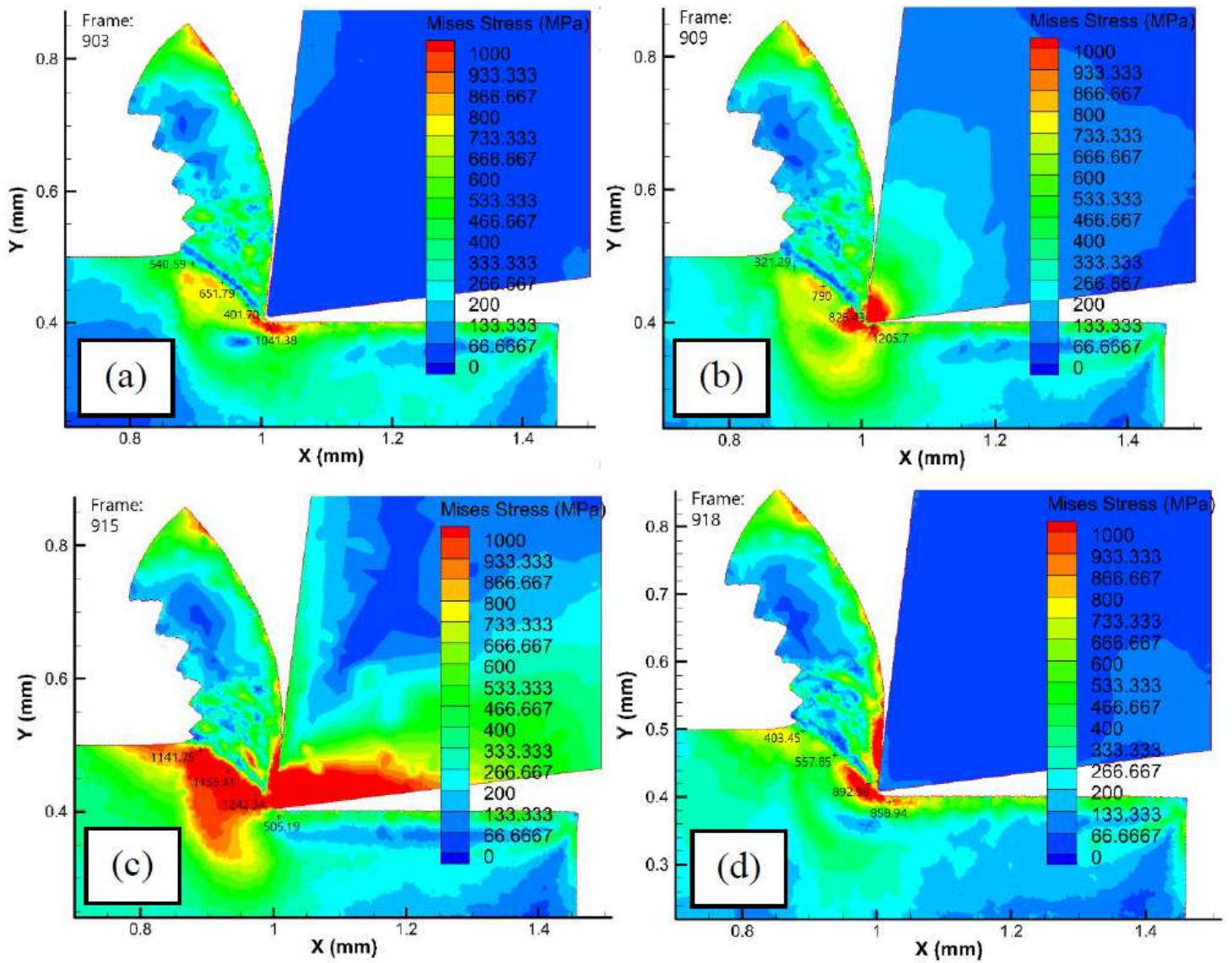


Figure 12

Von Mises stress contour in the 2D-VAC process at $V_c = 9$ m/min, $f = 100$ $\mu\text{m}/\text{rev}$, $w = 80$ μm , $f_v = 16$ kHz, $\phi = 90^\circ$, $a = 5$ μm , and $b = 5$ μm (a) after retracted tool, (b) beginning to cut, (c) cutting process, (d) disengaged tool

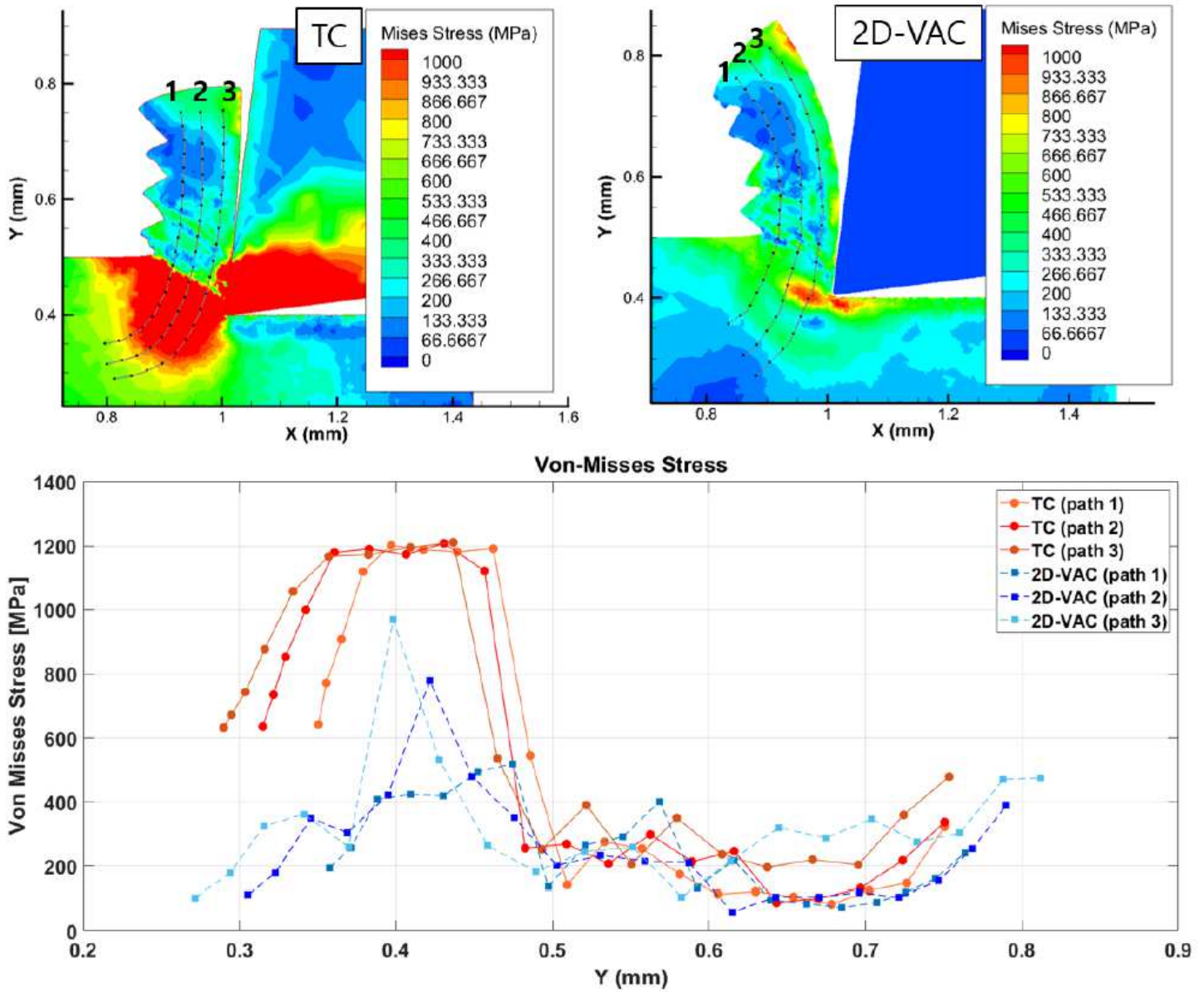


Figure 13

Von Mises stress comparison between the TC and the 2D-VAC at $V_c = 12$ m/min, $f = 100$ μ m/rev, $w = 80$ μ m, $f_v = 16$ kHz, $\varphi = 90^\circ$, $a = 5$ μ m and $b = 5$ μ m

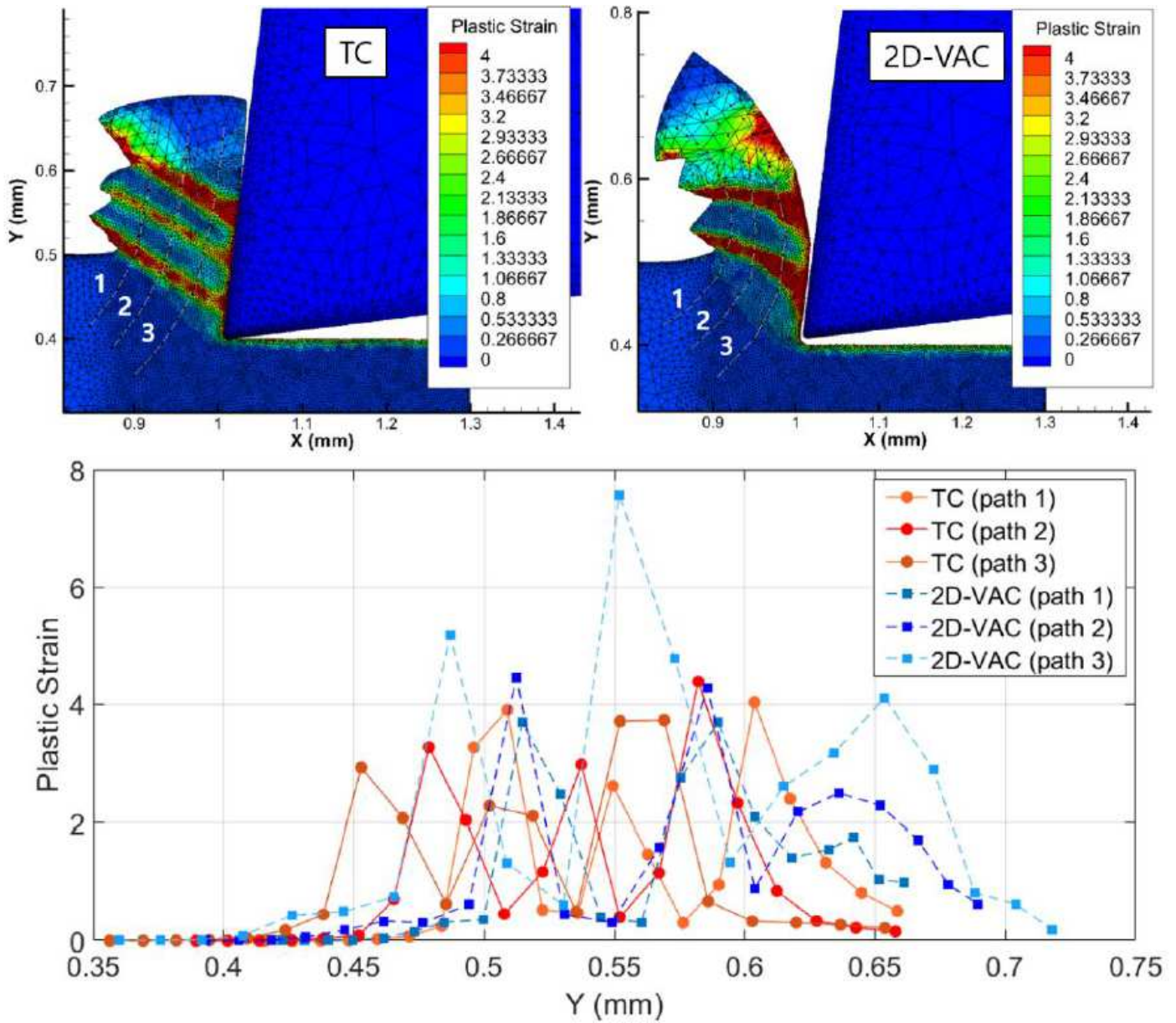


Figure 14

Plastic strain comparison between the TC and the 2D-VAC at $V_c = 7$ m/min, $f = 100$ $\mu\text{m}/\text{rev}$, $w = 80$ μm , $f_v = 16$ kHz, $\phi = 90^\circ$, $a = 5$ μm , and $b = 5$ μm

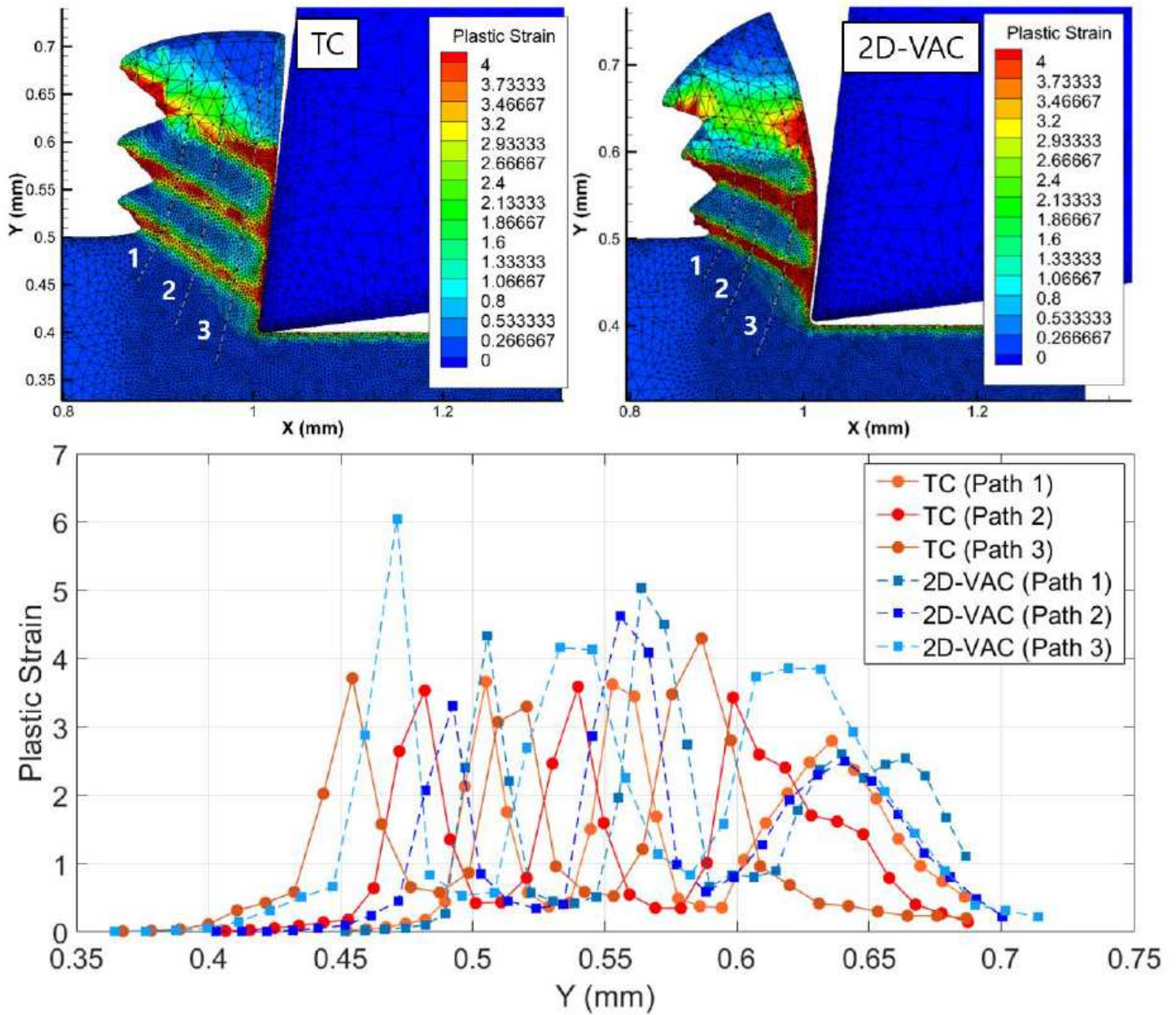


Figure 15

Plastic strain comparison between the TC and the 2D-VAC at $V_c = 9$ m/min, $f = 100$ $\mu\text{m}/\text{rev}$, $w = 80$ μm , $f_v = 16$ kHz, $\phi = 90^\circ$, $a = 5$ μm , and $b = 5$ μm

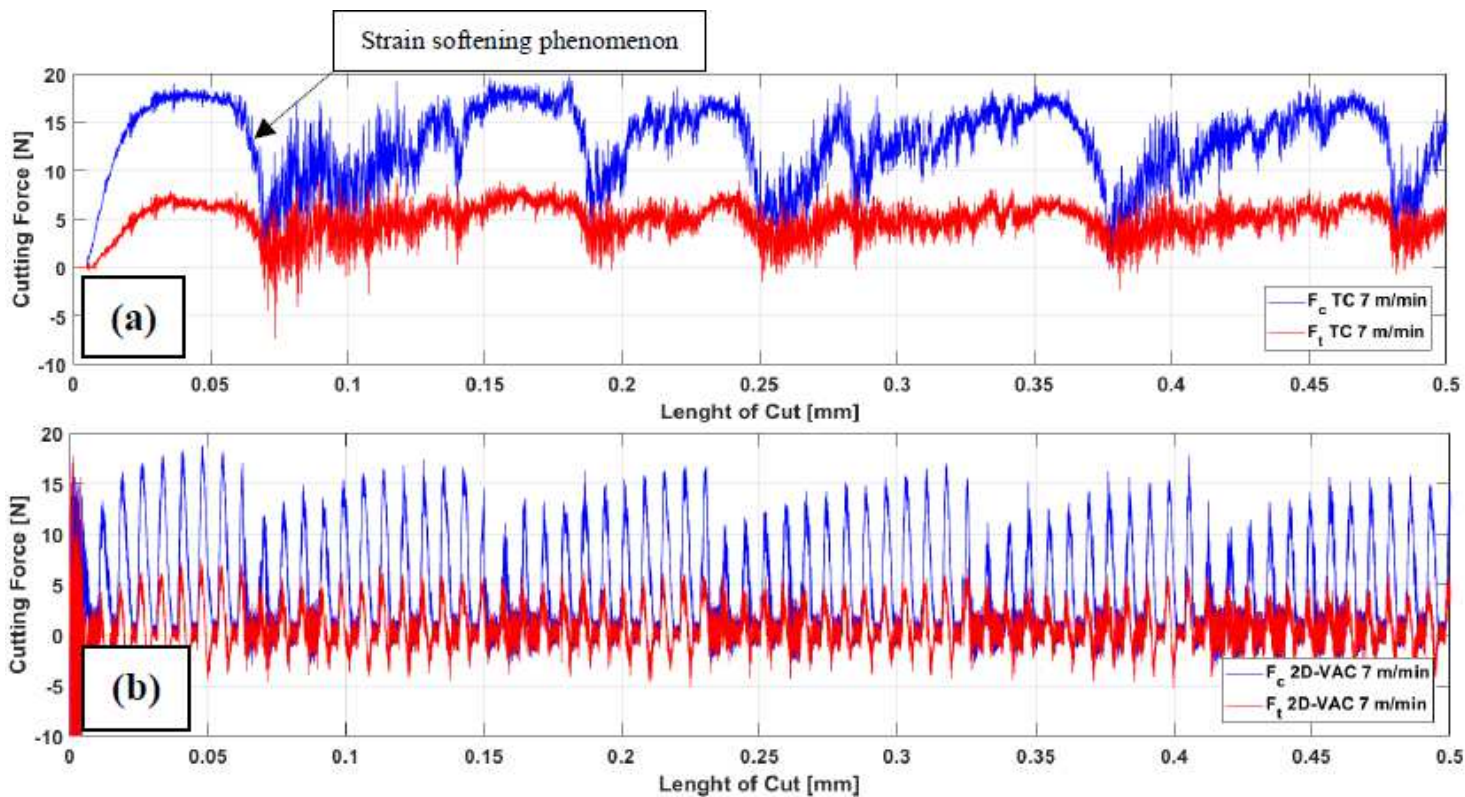


Figure 16

Simulated cutting force comparison between (a) the TC and (b) the 2D-VAC at $V_c = 7$ m/min

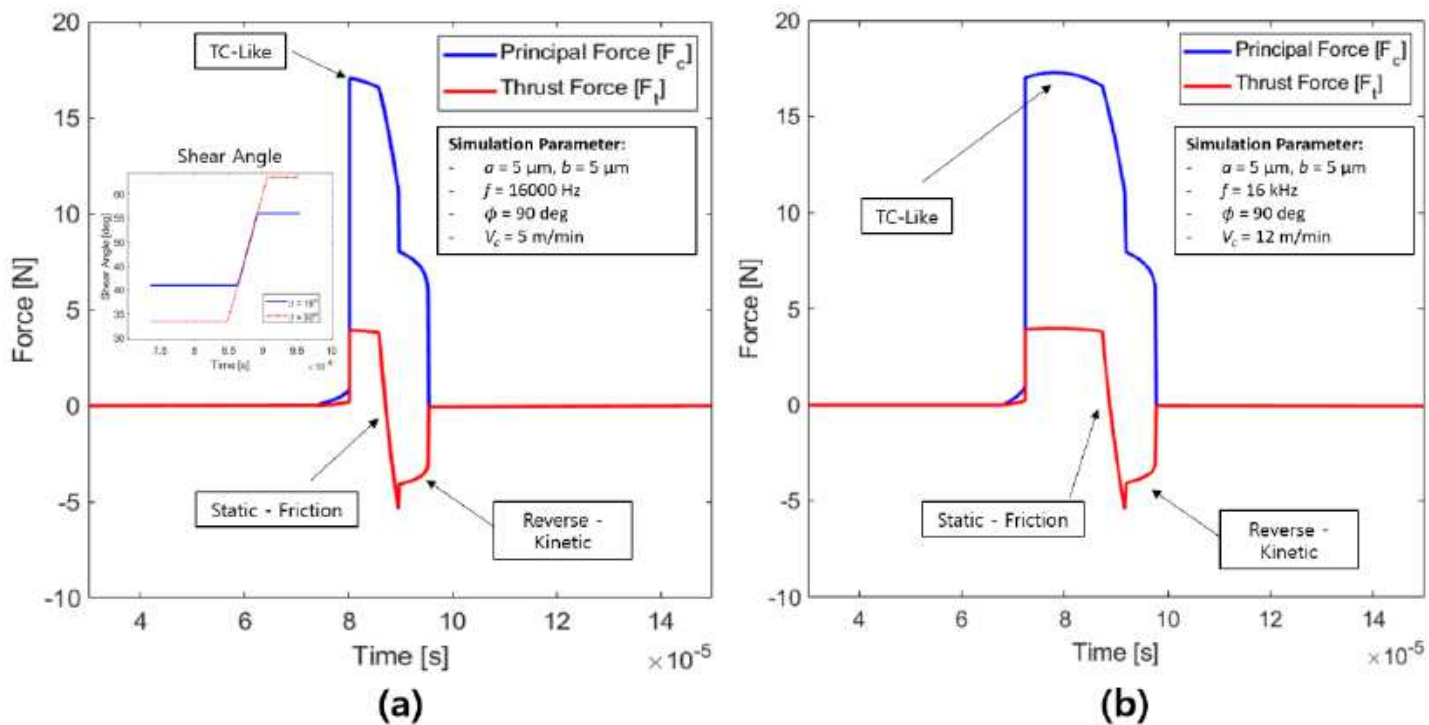


Figure 17

Simulated cutting force in the 2D-VAC. (a) $V_c = 5$ m/min, (b) $V_c = 12$ m/min

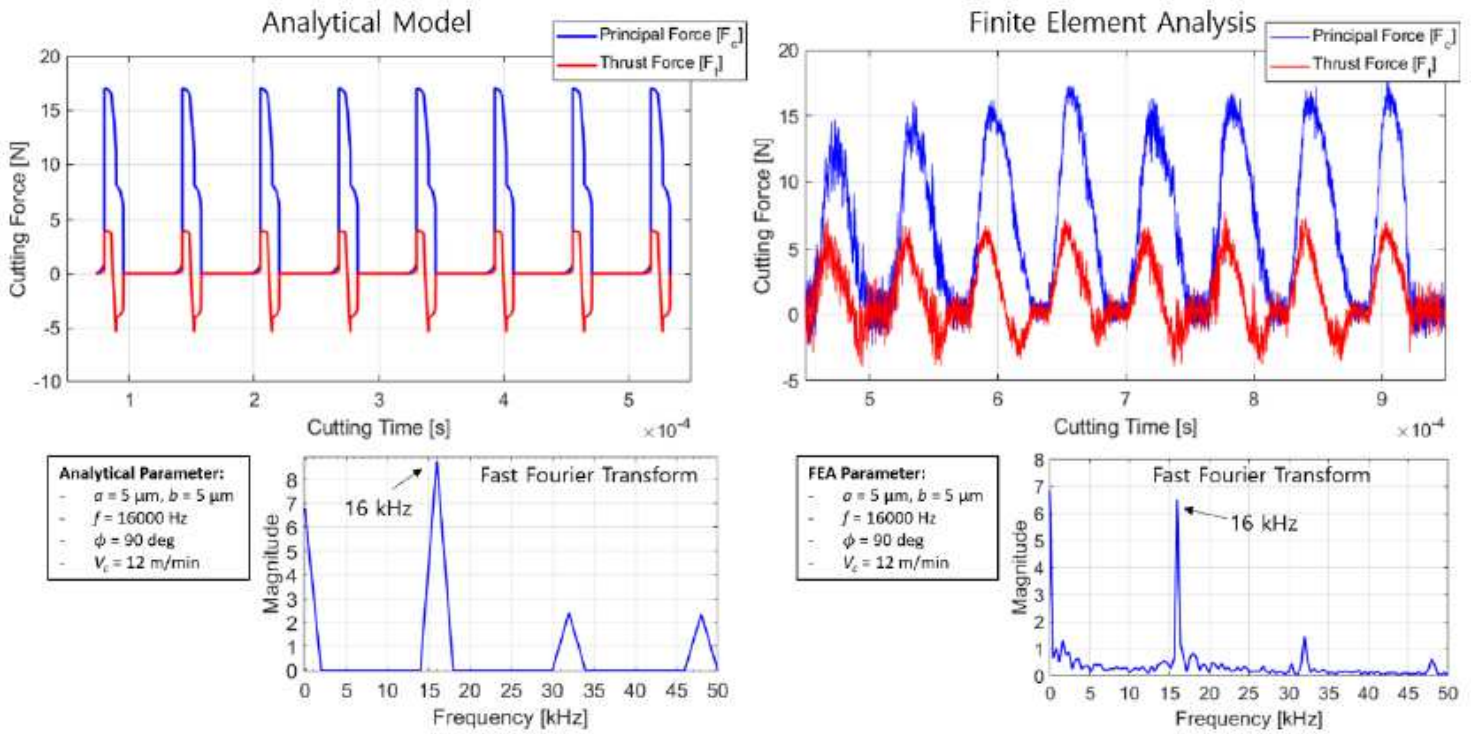


Figure 18

Comparison between analytical force and FEA simulated force for the 2D-VAC at $V_c = 12$ m/min

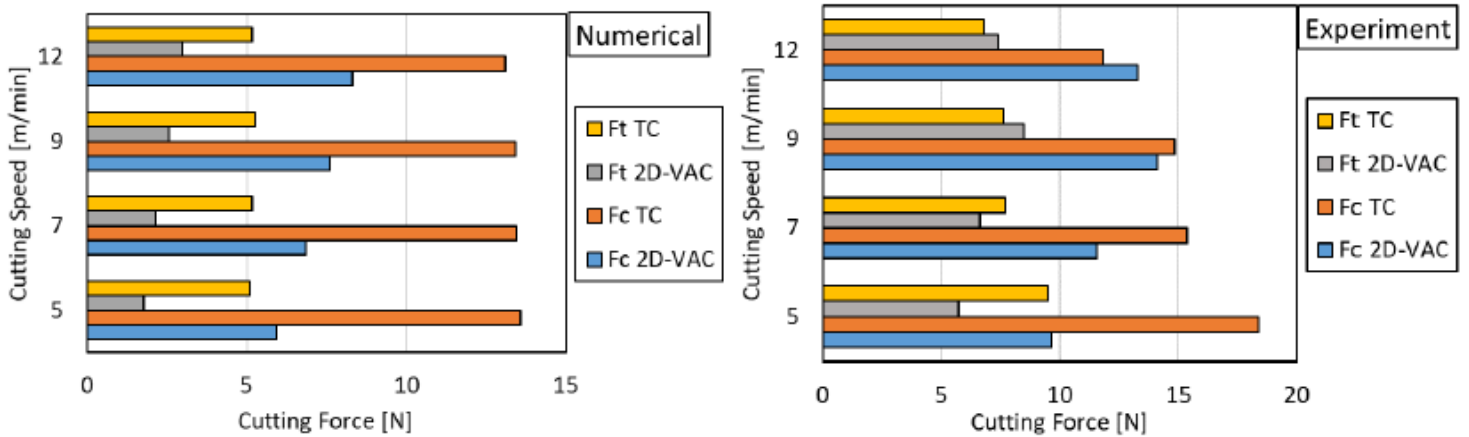


Figure 19

Average cutting force comparison among numerical and experimental results.

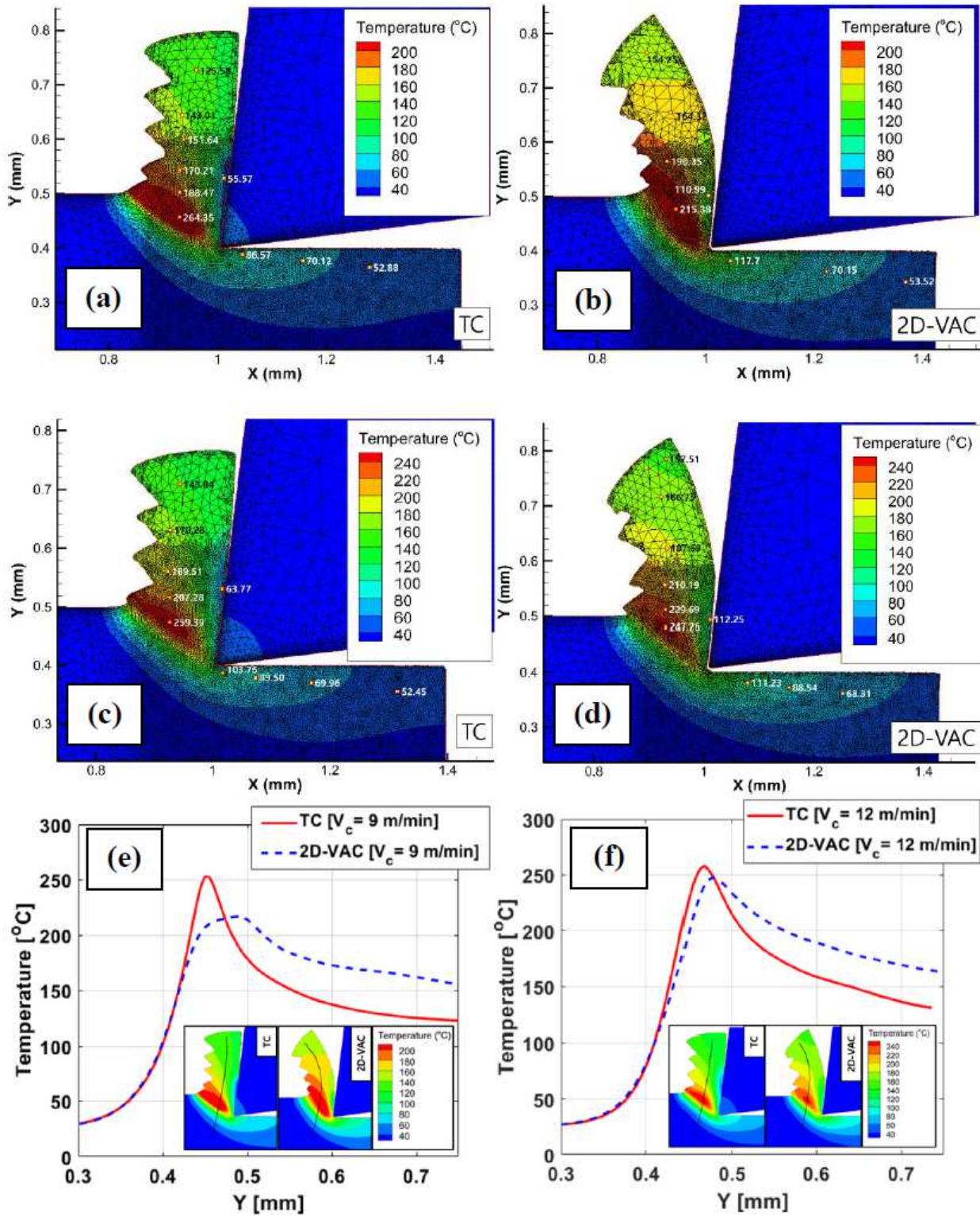


Figure 20

Temperature contour comparison between (a) TC at $V_c = 9$ m/min, (b) 2D-VAC at $V_c = 9$ m/min, (c) TC at $V_c = 12$ m/min, (d) 2D-VAC at $V_c = 12$ m/min, (e, f) temperature plot at specific polyline.

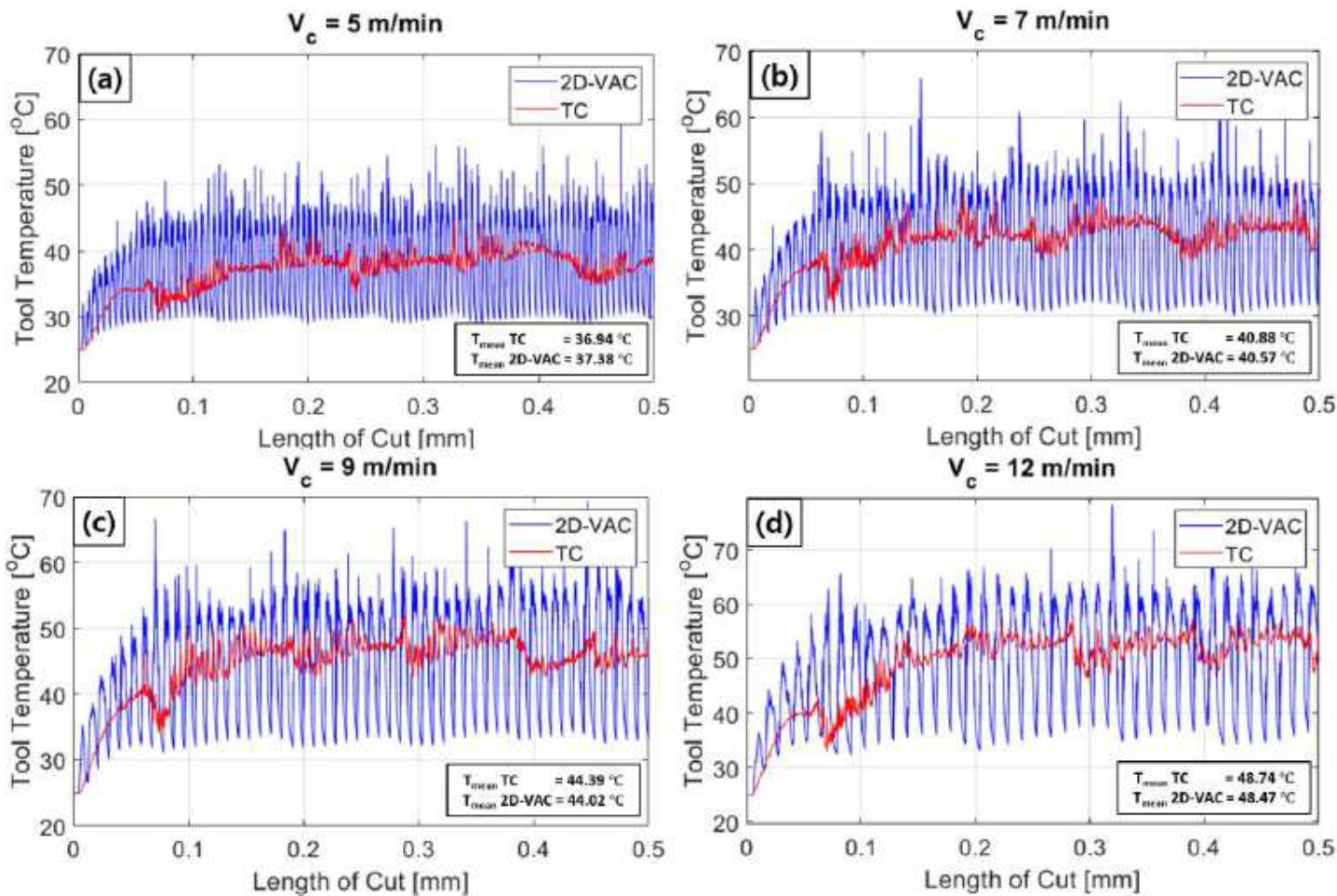


Figure 21

Comparison of the average simulated temperature in the cutting tool between the 2D-VAC and TC method through change of the cutting speed. (a) $V_c = 9$ m/min, (b) $V_c = 7$ m/min, (c) $V_c = 9$ m/min and (d) $V_c = 12$ m/min

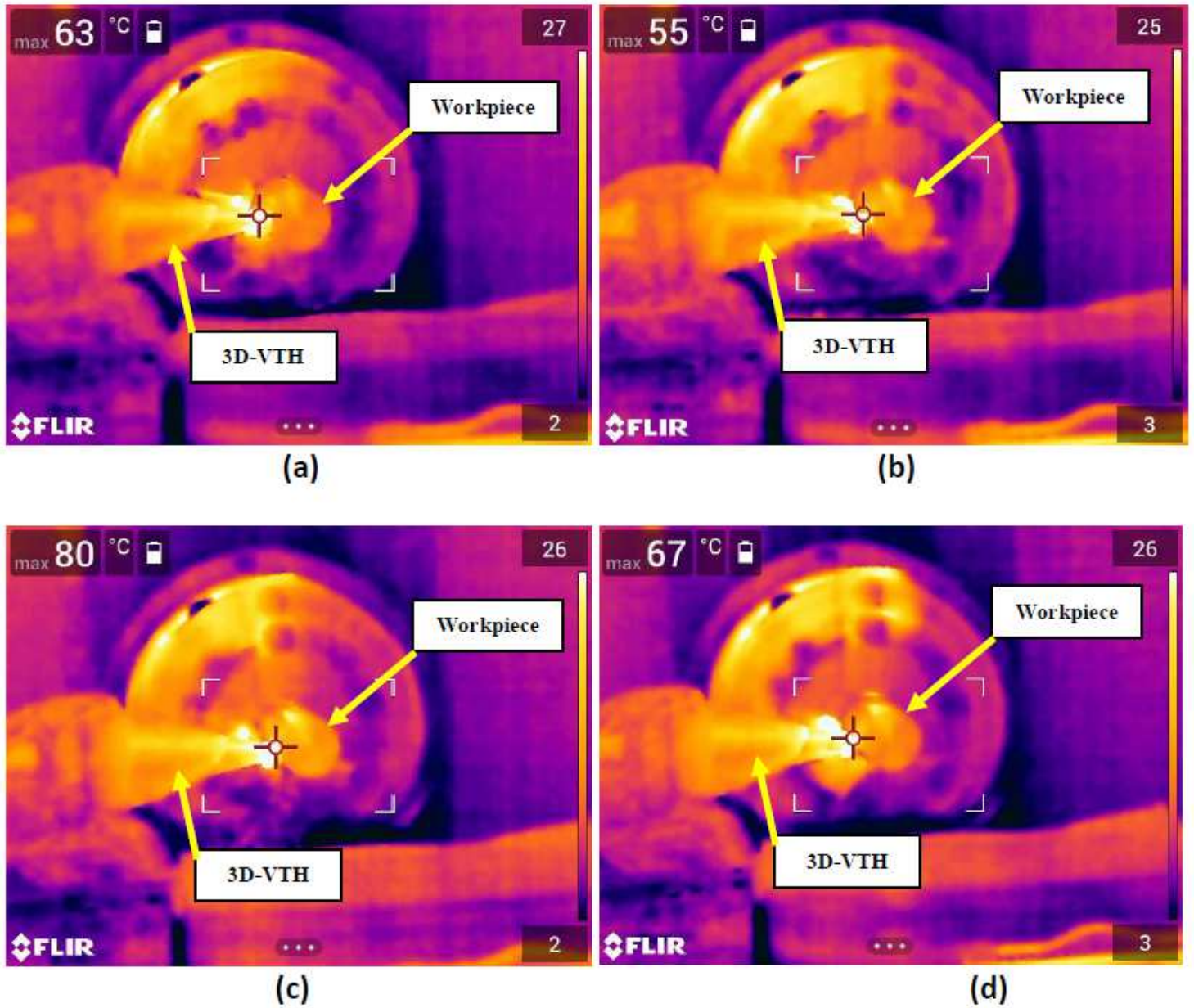


Figure 22

Temperature measurement using IR camera on the tool tip (a) TC at $V_c = 9$ m/min, (b) 2D-VAC at $V_c = 9$ m/min (c) TC at $V_c = 12$ m/min, and (d) 2D-VAC at $V_c = 12$ m/min

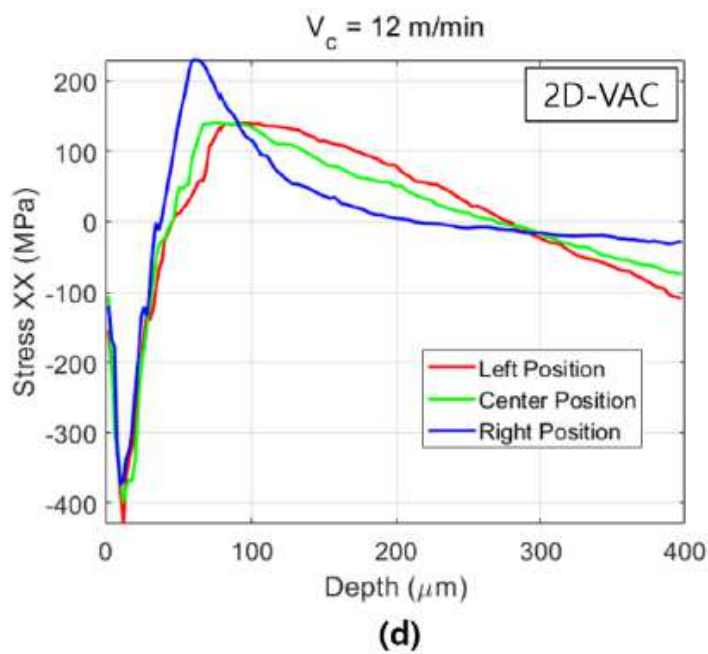
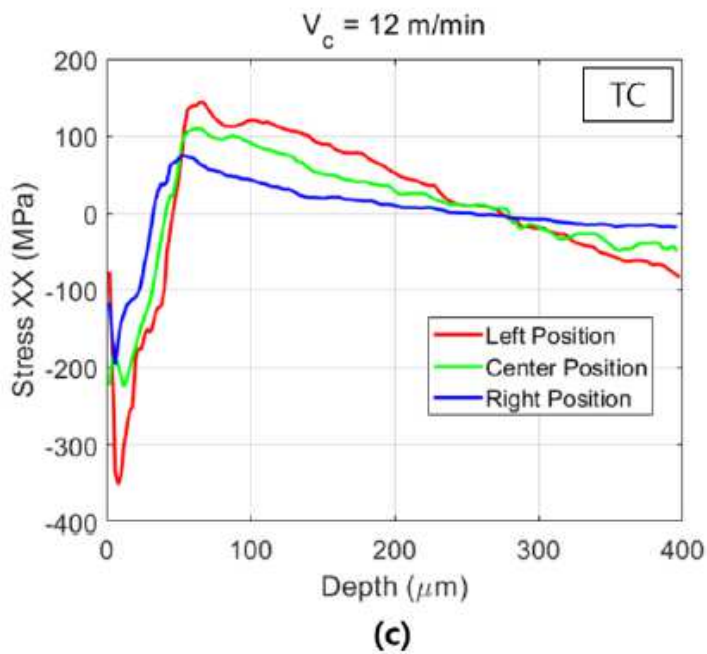
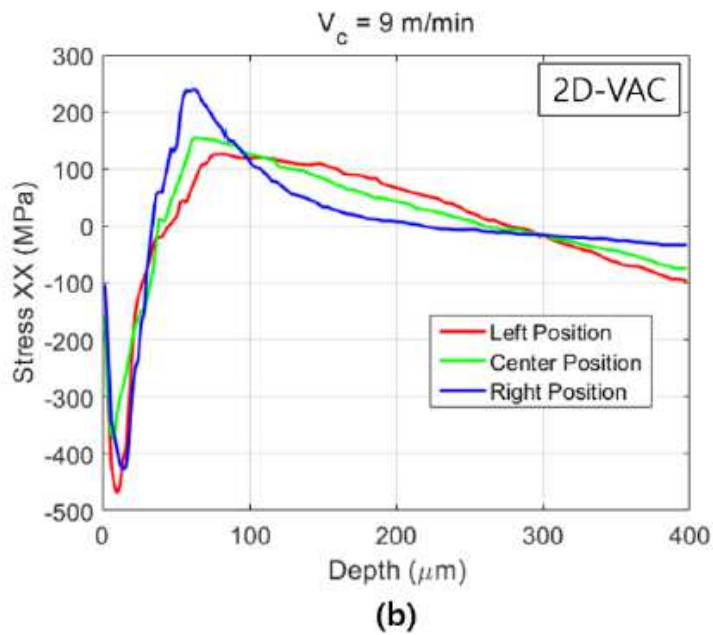
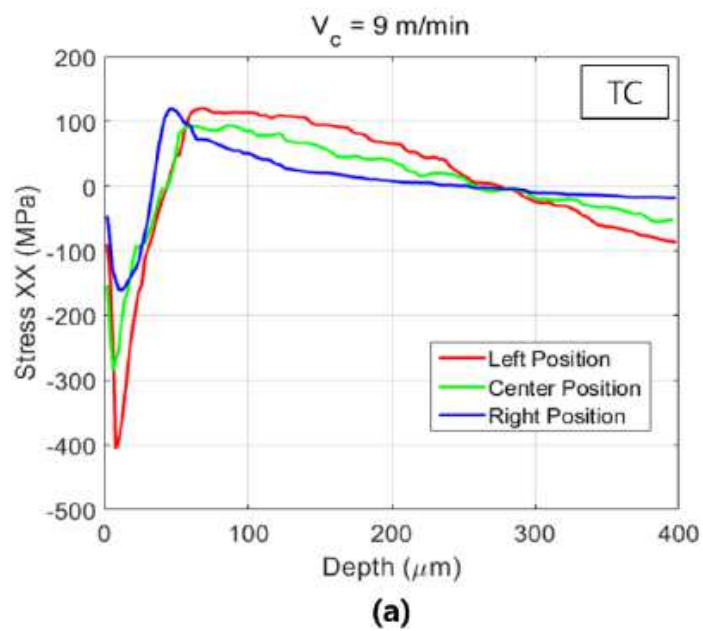


Figure 23

Residual stress comparison between TC and 2D-VAC, (a, b) with $V_c = 9 \text{ m/min}$, (c, d) with $V_c = 12 \text{ m/min}$

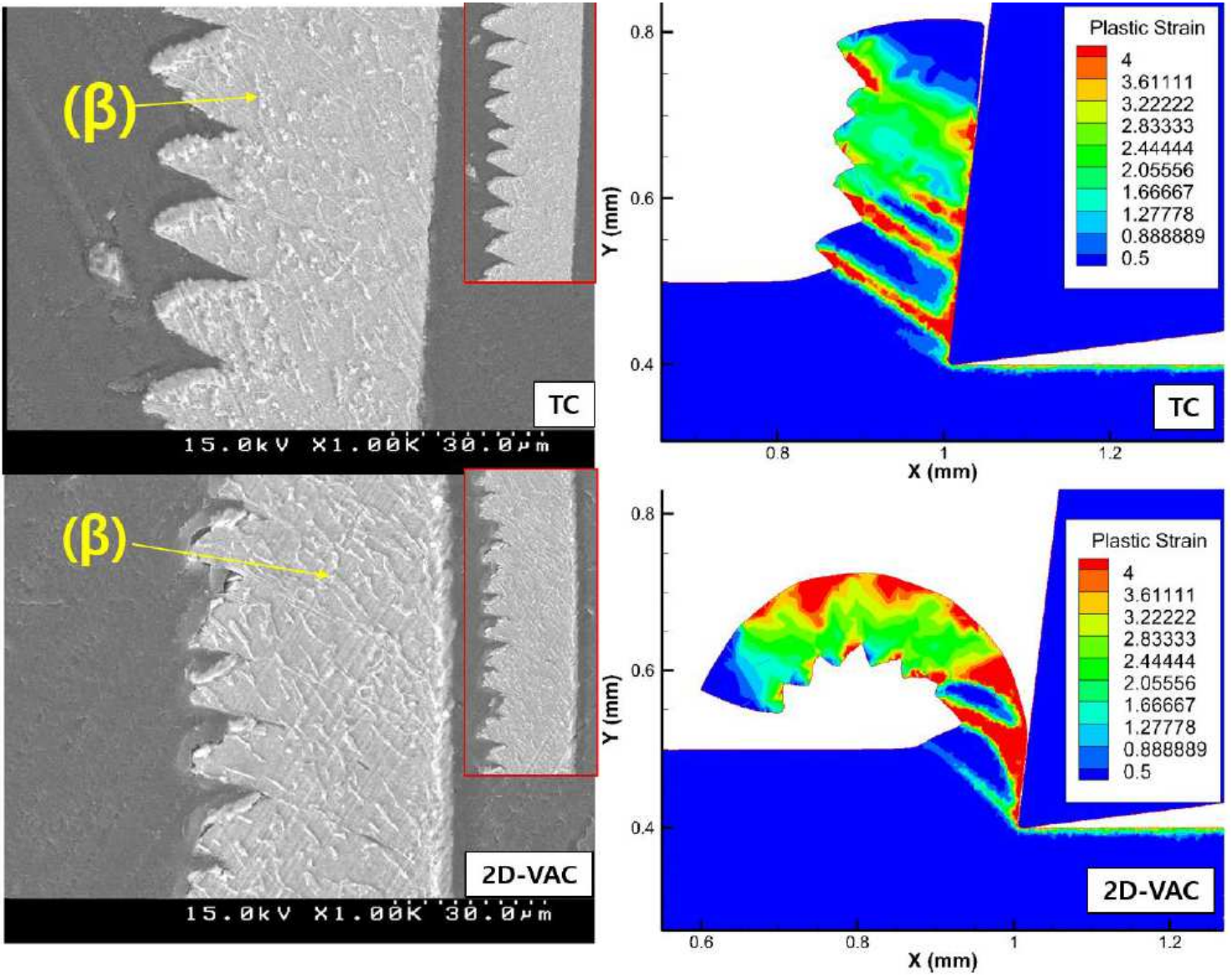


Figure 24

Chip formation comparison between the TC and the 2D-VAC at $V_c = 5$ m/min

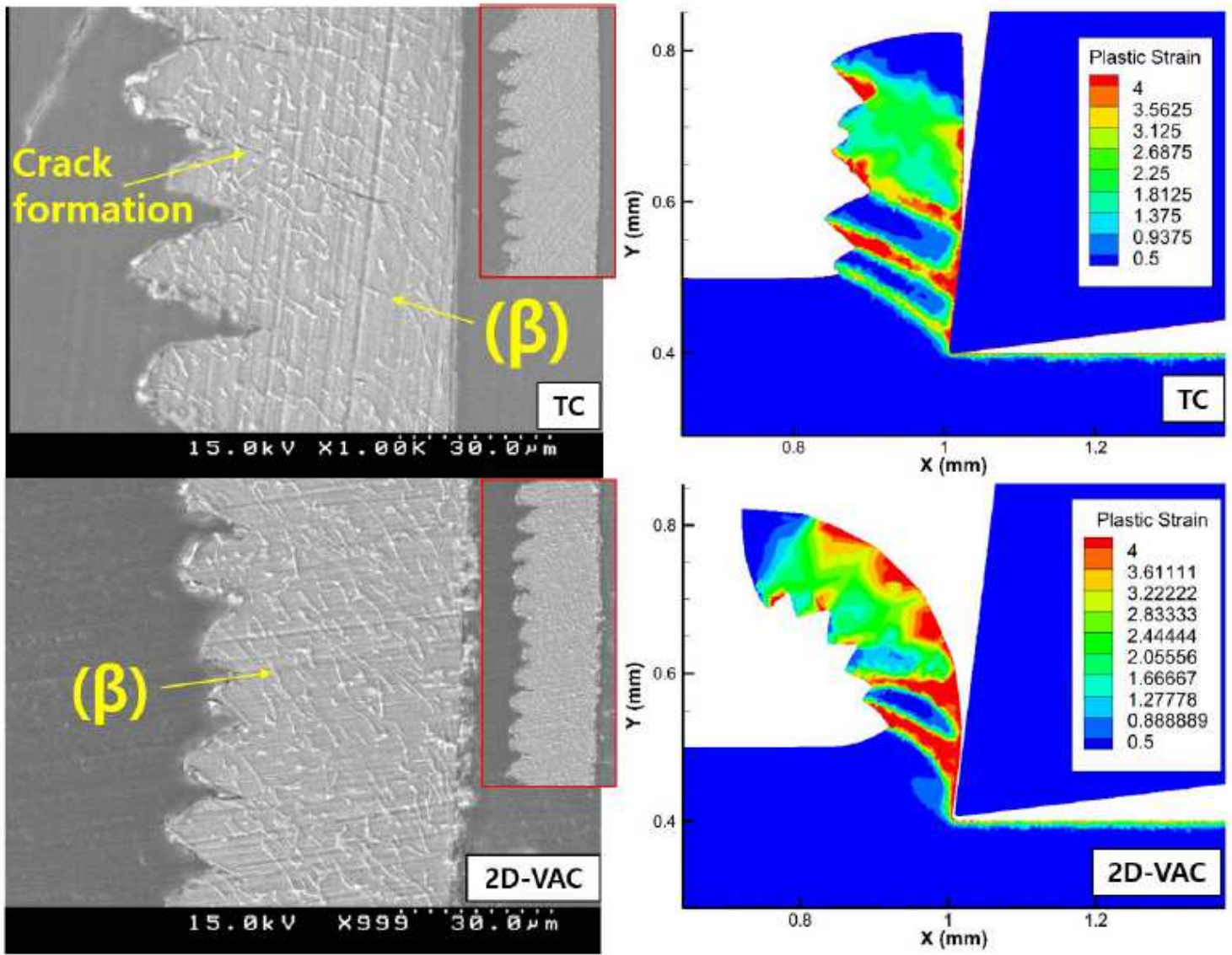


Figure 25

Chip formation comparison between the TC and the 2D-VAC at $V_c = 7$ m/min

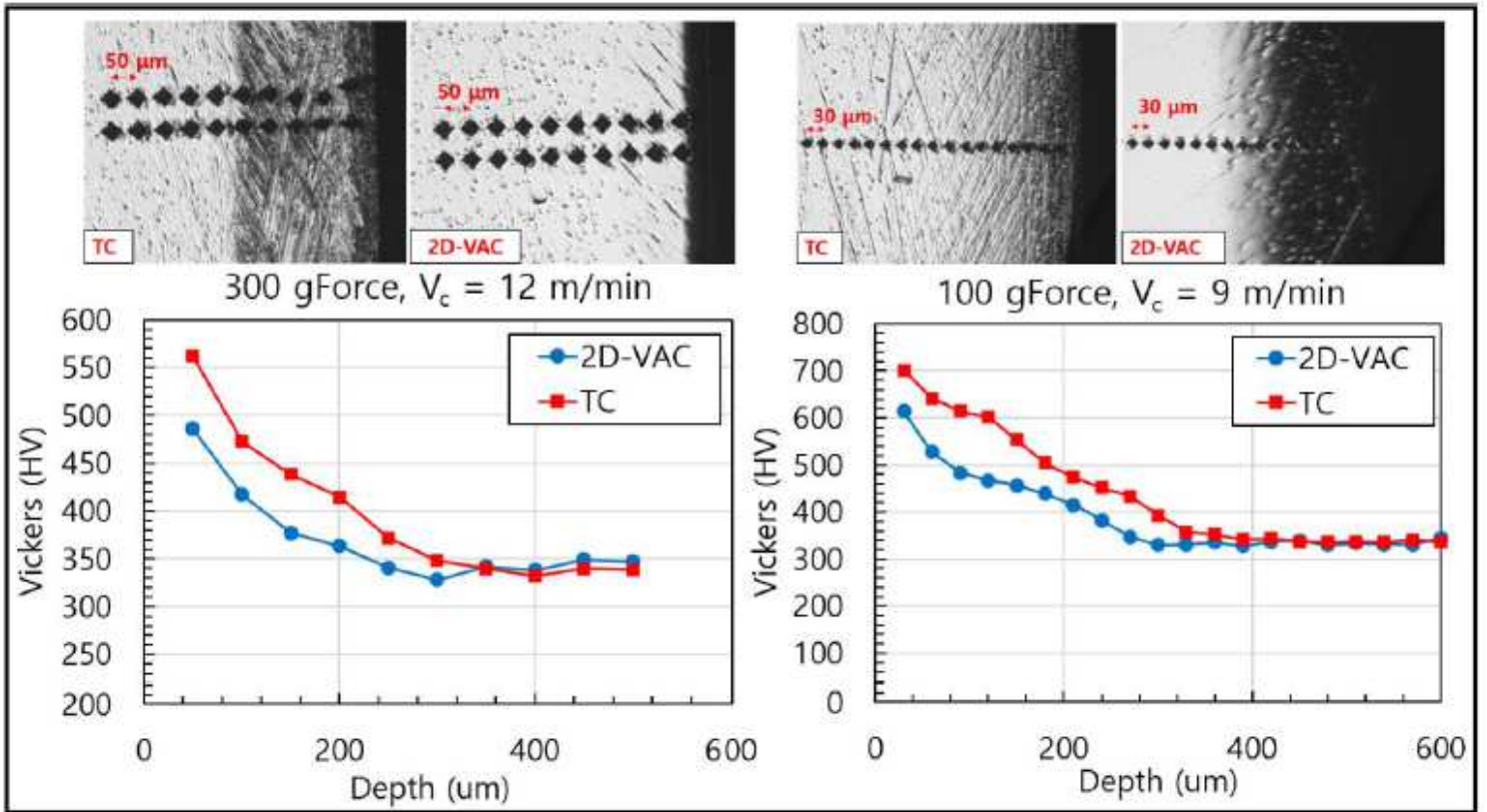
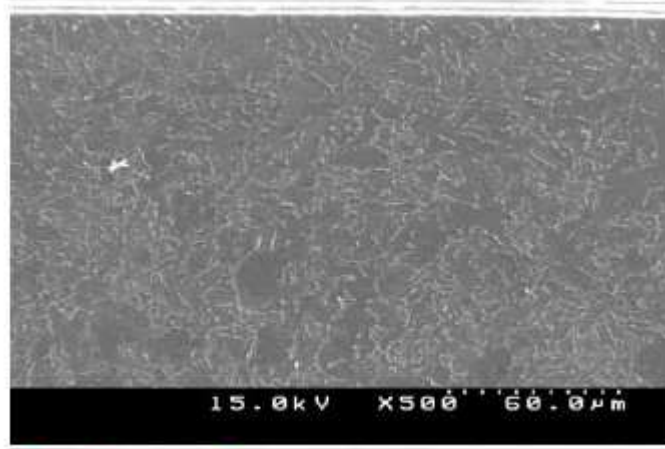
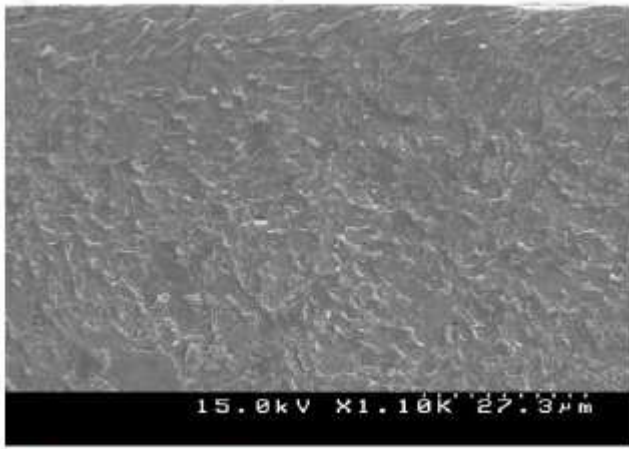


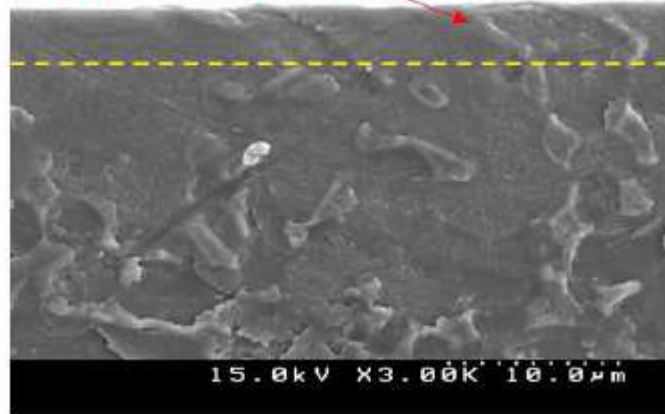
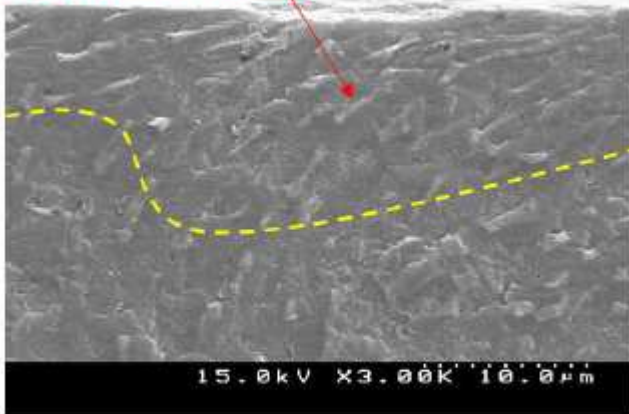
Figure 26

Micro-hardness comparison between the TC and the 2D-VAC method under $V_c = 12$ m/min and $V_c = 9$ m/min.



β phase flow

β phase flow



(a) TC $V_c = 12$ m/min

(b) 2D-VAC $V_c = 12$ m/min

Figure 27

Micro-structure comparison between (a) TC and (b) 2D-VAC process